SINGLE VIRION FUSION STUDIES OF MEMBRANE-ENVELOPED VIRUSES TO BIOMIMETIC MEMBRANES

A Dissertation

Presented to the Faculty of the Graduate School

of Cornell University

In Partial Fulfillment of the Requirements for the Degree of

Doctor of Philosophy

by

Deirdre Ann Costello

[January 2014]

SINGLE VIRION FUSION STUDIES OF MEMBRANE-ENVELOPED VIRUSES TO CELL-DERIVED MEMBRANES

Deirdre Ann Costello, Ph. D.

Cornell University [2014]

Understanding the mechanisms involved in the viral entry process is key for developing effective anti-viral therapies and vaccines. Entry of membrane-enveloped viruses typically involves two key processes mediated by a dual-function viral glycoprotein. During influenza infection hemagglutinin (HA) binds to sialic acid moieties on epithelial cell membranes, triggering engulfment into the cell via endocytosis. As the endosome matures and becomes more acidic, HA undergoes a conformational change, which induces fusion of the viral and endosomal membranes, releasing viral RNA into the cell. Quantitative kinetic studies of binding and fusion are often conducted *in-vitro* to obtain high-resolution measurements. Total internal reflection microscopy combined with microfluidics and supported bilayers is a powerful, single particle tracking (SPT) platform for host-pathogen membrane fusion studies.

One inadequacy of the aforementioned SPT platform has been capturing the complexity of the cell membrane, including membrane proteins. Sialic acid receptors are easily integrated into the platform using glycolipids. However, viruses that bind proteinaceous receptors for cell entry have been precluded from study. We have developed a general method to integrate proteinaceous receptors and cellular

membrane components into supported lipid bilayers for SPT fusion studies of feline coronavirus (FCoV). Supported lipid bilayers are formed from mammalian cell membrane vesicles that express the FCoV receptor, aminopeptidase N (APN), using a cell blebbing technique. SPT is then used to identify fusion intermediates and measure membrane fusion kinetics of FCoV, which to our knowledge have not been obtained before. Overall, the fusion results recapitulate what is observed *in-vivo*, that coronavirus required binding to specific receptors, a low-pH trigger, and that membrane fusion is receptor and protease-dependent. We also observe that small populations of FCoV viruses are capable of fusing at neutral pH. This phenomenon was previously un-reported in-vivo for this strain of FCoV and may have implications for explaining the infection efficiency and cellular tropism of some coronaviruses. This platform also provides a new route to study how viruses rapidly adapt to other hosts, and to identify the factors that led to the emergence of other zoonotic coronaviruses, such as SARS-CoV and the new emerging MERS-CoVe. In this thesis I will also present our advances on using the cell blebbing technique to create simple virus-like particles (VLPs). VLPs can be used to study the highly pathogenic coronaviruses such as SARS-CoV and avian influenzas such as H5N1 in a biosafety level 2 laboratory

BIOGRAPHICAL SKETCH

Deirdre Ann Costello was born in Jamestown, Co.Kilkenny, Ireland to Margaret and John Costello on October 2nd 1986. She attended secondary school in Mercy Convent, Greenhill, Carrick-on-Suir, Co. Tipperary. Deirdre went on to attend University College Dublin graduate first in her class, receiving a first class honors degree in Chemical Engineering in June 2008. In August 2008 she entered the PhD program in Chemical and Biomolecular Engineering at Cornell University and studied under Professor Susan Daniel.

I dedicate this dissertation to my family, friends and all members of the Cornell community that supported me over the last five years.

ACKNOWLEDGEMENTS

The research presented in this thesis would not have been possible without the generous help and support of members of the Cornell community. First and foremost I thank my advisor Professor Susan Daniel, and the members of my special committee, Professor Gary Whittaker, Professor Lois Pollack and Professor David Putnam. I also thank all the members of the Daniel Research Group past and present, for their help with experiments and thoughtful discussion, especially Dr. Ling Chao and Dr. Kassandra Kissler. I also thank the Whittaker Research Group, especially Dr. Jean Millet and Nadia Chapman for training me and teaching me about virology. Much of this work would not have been possible without the valuable training I received from Dr. Dave Holowka. I thank all of the tool managers at the CNF, John Grazul at CCMR and Teresa Porri at NBTC. Finally I would like to thank all of the administrative and support staff in Olin Hall, especially Shelby Clark-Shevalier for always having the answers to my questions. Grants and funding bodies that supplied research funding are acknowledged at the end of each chapter.

TABLE OF CONTENTS

LIST OF FIGURES

LIST OF TABLES

LIST OF ABBREVIATIONS

APN – alanine aminopeptidase

BHK – Baby hamster kidney

Dioleoyl

FCoV – Feline coronavirus

FECV – Feline enteric coronavirus

HA – Hemagglutinin

MDCK – Madine darby canine kidney

NBA – nitrobenzaldehyde

PDMS – Polydimethylsiloxane

S – Spike protein

TLE – Total liver extract

TGE – Total ganglioside extract

LIST OF SYMBOLS

Γ – gamma function

N – number of trimers

k_H – hemifusion rate constant

k_{pore} – pore formation rate constant

CHAPTER 1

LITERATURE REVIEW

1.1 Membrane Enveloped Viral Infection

A membrane-enveloped virus is in essence a collection of viral genes, encapsulated in a lipid membrane and decorated with viral proteins that mediate host cell entry and egress. Membrane enveloped viruses infect host species by fusing the lipid membrane surrounding the viral genome with the membrane of host cells. Fusion of two biological membranes is thermodynamically favorable but the kinetic barrier is high(1). This kinetic barrier is overcome by engaging membrane proteins on the surface of the virus to mediate membrane fusion(2). Before this kinetic barrier can be overcome, viral proteins undergo activation steps. Most viral fusion proteins require a priming event, such as proteolytic cleavage, which prepares the virus for cellular uptake(3). At some point during the entry process, the viral fusion protein undergoes a conformational change, frequently triggered by proton binding in a low pH environment or binding to a specific membrane protein. The conformational change in the fusion protein mediates the merging of the viral and cellular membrane(4), resulting in the release of the genome and continuation of the replication cycle. Membrane fusion and the cellular cues accompanying this process are thus vital steps in the life cycle of many viruses. Membrane-enveloped viruses include influenza A, severe acute respiratory syndrome (SARS), human immunodeficiency virus (HIV) and

ebola virus. These viruses represent some of the biggest threats to global health and thus warrant the development of quantitative methods to discern the steps involved cell entry.

The most well characterized viral fusion protein is influenza hemagglutinin (HA), which mediates both cellular binding and membrane fusion. Understanding the mechanism of influenza entry has been the subject of much research over the last twenty years because of the constant threat of another highly lethal strain emerging similar to the 1918 pandemic strain.

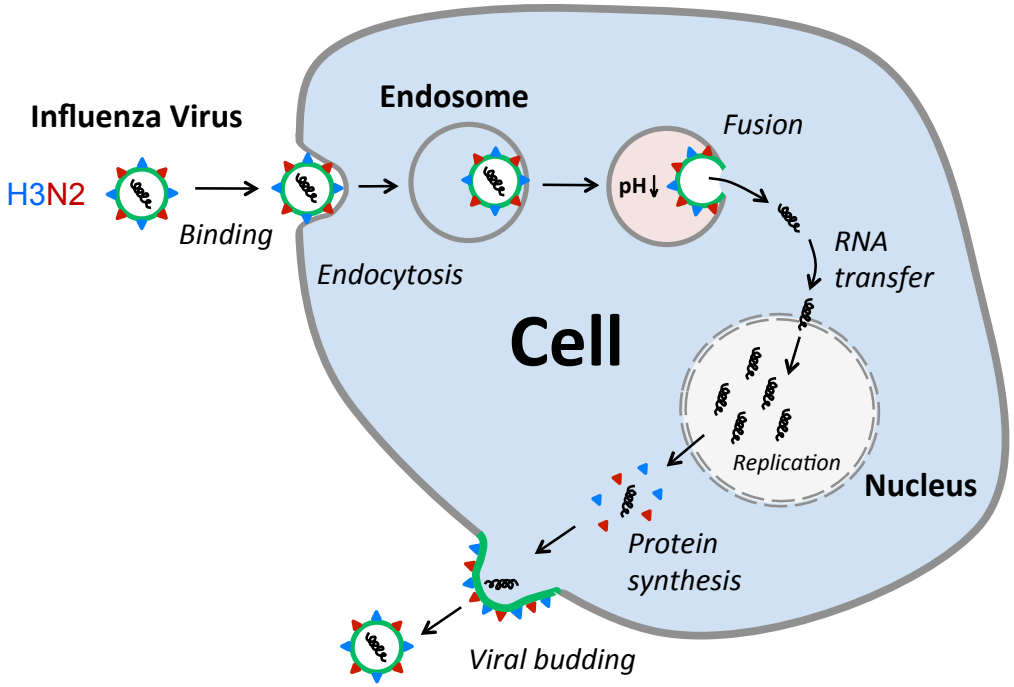

Figure 1 schematic of influenza replication cycle. Virus enters the cell by receptor mediated endocytosis. As the endosome matures and becomes midly acidic, the viral and target membranes fuse and the segmented viral genome is released. RNA is replicated in the nucleus and after transcription and translation of viral proteins the viru assembles at the plasma membrane. Influenza acquires it's membrane by budding through the plasma membrane and progenies go on to infect neighbouring cells.

HA binds to sialic acid residues on the cell plasma membrane. This binding event triggers uptake via receptor mediated endocytosis(5). As the endosome matures, the pH drops from neutral to a mildly acidic pH(6) (between 6 and 5) and it is this change in pH which initiates the HA conformational change and provides the energy that initiates membrane fusion. HA is a protein comprised of two glycopolypeptides, HA_1 and HA_2, linked by a single disulphide bond. HA_2 is anchored in the viral membrane by its C-terminus. Structural analysis(7, 8) has revealed that HA_2 chains are a large component of an alpha-helical stem, which forms the center of the molecule. HA_1 chains form three membrane distal globular domains containing the sialic acid binding sites. A key feature of the HA_2 domain is the presence of a hydrophobic sequence located close to the N-terminus called the fusion peptide(9, 10), shown in *figure 2*. The fusion peptide is located approximately 35 Å from the viral membrane and 100 Å from distal tip of the HA. During the low pH-induced conformational change of HA, the fusion peptide is exposed and inserts into the endosomal membrane.

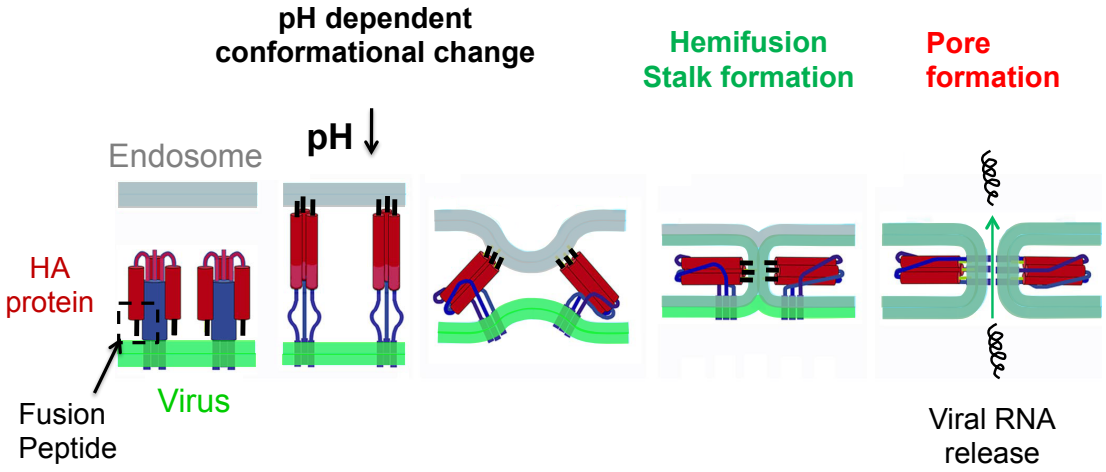

Figure 2. Schematic of the hypothesized steps in the membrane fusion process. Adapted from Harrison et al(11). The fusion peptide of HA (small green ends of the red region) is concealed and facing the viral

membrane until the pH drops to 5.5. Proton binding results in the projection of the fusion peptide to the target membrane and conformation rearrangement of the protein that leads to the bending of the two membranes. The outer leaflets of the membranes are the first to mix (hemifusion) and upon collapse of the hemifusion stalk a fusion pore is opened. The viral capsid is then released into the cell where it is transported to the nucleus for replication.

Viral membrane fusion entails multiple kinetic steps and the activation of multiple HA trimers. In recent years it has been shown that number of HAs needed for fusion is could be anywhere from one to six (12-14) .

Harrison(11) proposed the following mechanism, which is summarized in *figure 2*.

1. The fusion peptide of HA bridges the target membrane forming an extended intermediate state of HA and enabling the first steps of membrane fusion.
2. The extended intermediate then undergoes collapse and the C-terminal segment of the protein folds back along the outside of the HA. Segments from the three subunits of the C-terminal do not fold back at the same rate so that they can extend to different lengths along the HA core, enabling the entire protein to bend away from the deformed membrane.
3. Hemifusion happens next, as the outer monolayers of the membranes are brought into contact after the extended intermediate collapses. The outer monolayers fuse into a hemifusion stalk.
4. The hemifusion stalk collapses and a fusion pore opens. Hemifusion is the final intermediate state before a fusion pore is fully formed and RNA is released.

Understanding the entry mechanisms is key not only for influenza viruses, but also for other viruses that can utilize the endosomal pathway to enter cells. In the last 10 years, coronaviruses have emerged as a serious pandemic threat. Coronaviruses are zoonotic viruses that typically cause respiratory and enteric disease in mammals and birds. Like influenza, transmission of coronavirus can occur between animal reservoirs and a human host. The outbreak of severe acute respiratory syndrome (SARS) in 2003 and Middle Eastern respiratory syndrome (MERS) in 2012 are two widely known examples of such species jumping events. The factors that contribute to coronaviruses adapting to new hosts are not well understood and due to the high mortality rates associated with SARS and MERS, understanding the critical steps involved in viral entry has become increasingly important for developing antiviral therapies.

Coronavirus membranes typically contain 3 viral proteins, spike protein (S), the membrane protein (M) and the envelope protein (E)(15). The spike protein regulates both binding and membrane fusion and thus plays an important role in determining the host tropism. Like influenza (HA), spike binds to cellular receptors and triggers uptake of the coronavirus via endocytosis and membrane fusion is mediated by conformational changes in the spike protein(16). Spike protein must undergo proteolytic cleavage to expose the hydrophobic fusion peptide that mediates membrane fusion(15, 17). The timing of cleavage can be a key determinant in pathogenicity. For example, influenza HA may be cleaved by several proteases, but some serotypes can be cleaved with host cell furin during the secretion pathway, resulting in a systemic infection(3). Timing is equally important for coronavirus S cleavage. The most dramatic example occurs during infection with SARS. In the

presence of certain exogenous proteases SARS can bind and fuse at the cell surface, which is believed to 100- to 1000-fold more efficient than endosomal entry(18). This example demonstrates how the timing of proteolytic activation changed the pathway and efficiency. By studying coronavirus entry single particle fusion assays, the sequence of trigger e.g. cleavage-binding-fusion or binding-cleavage-fusion can be easily controlled and more insight into the entry pathways can be elucidated.

1.2 Methods for Monitoring Viral Fusion

In vitro systems are typically used to monitor fusion as conditions inside mammalian cells are difficult to control and assay. The majority of work to date uses bulk fusion techniques(19) to quantify viral fusion kinetics. In these experiments virus was labeled with self-quenching fluorescent dye conjugated to a single acyl chain, typically octadecylrhodamine B (R18), which inserts into the viral membrane. At high concentrations of R18 in the viral membrane the fluorescence is quenched. Upon fusion with nearby liposomes, triggered by low pH, the mixing of the viral and liposome membrane results in dilution of the R18. As the dye molecules diffuse into the target membrane, they become diluted and the overall fluorescence increases. From the change in fluorescence intensity in time, kinetic parameters can be obtained. Bulk experiments data does not provide enough detail or resolution to be able to observe the individual steps involved in viral fusion mechanism, for example, one cannot distinguish between binding of the virus to sialic acid receptors and fusion.

Single particle tracking techniques can mitigate many of the drawbacks associated with bulk fusion assays. The study of single events requires a surface-specific technique where individual viruses can be located and observed. One such optical technique is total internal reflection microscopy (TIRF). Recently, TIRF has increased in popularity for studying viral fusion(20-23). The use of TIRF with supported lipid bilayers to study viral fusion enables tracking of individual binding and fusion events. Using supported lipid bilayers facilitates the use of TIRF and its planarity is closer to the geometry the virus sees in the late endosome in nature. Events can be followed using the same dequenching strategy as used in the bulk assays, however, individual particles can be monitored using TIRF if the concentration of bound virus is low enough to distinguish particles from one another. In TIRF(24), a collimated laser beam is passed through a prism at a high incidence angle. Total internal reflection occurs when the laser beam passes from a medium with a high refractive index (glass coverslip) to a medium with a lower refractive index (water), at an angle that is larger than the critical angle α_c. The critical angle is calculated according to Snell's Law (equation 1)

$$n_1 \sin(\alpha_1) = n_2 \sin(\alpha_2) \quad \text{Equation 1}$$

$$\alpha_2 = 90^o$$

$$\alpha_c = \sin^{-1}\left(\frac{n_2}{n_1}\right)$$

In our system, n_1 and n_2 are the refractive indices of water (1.33) and the glass coverslip (1.518), respectively. Using these values, the critical angle (α_c) is 61°. When

the angle incident laser beam is greater than 61°, total internal reflection occurs at the interface of the coverslip and water. This results in a standing wave at the interface, with an intensity that decreases exponentially with distance away from the interface. This is known as an evanescent wave. This surface-specific technique typically illuminates a region up to 200 nm away from the interface, thus exciting only fluorophores that are located in this region and eliminating any noise from particles in the bulk fluid *(figure 4)*. By locating the supported bilayer within the evanescent field, viral particles can be bound within the evanescent field to facilitate observation of fusion events.

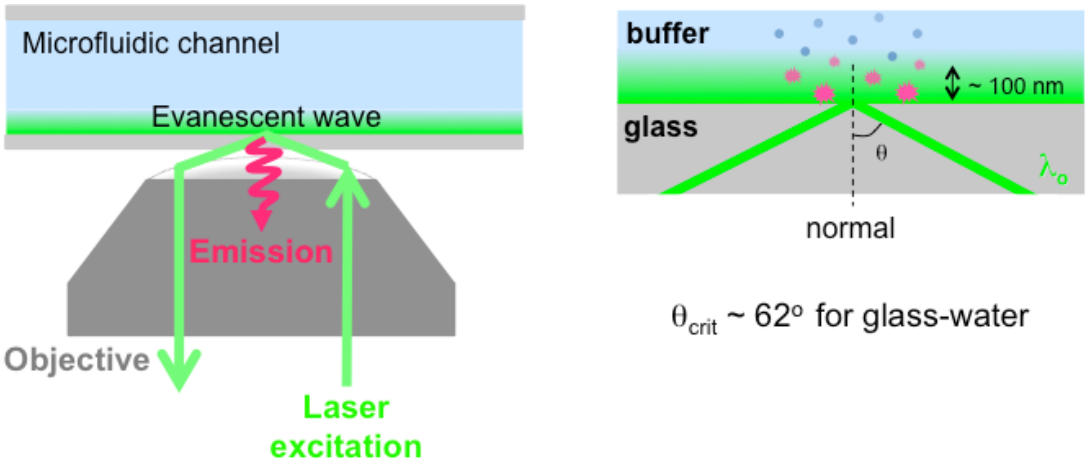

Figure 3. Schematic representation of TIRF microscopy. The incident laser beam is totally internally reflected at the interface between glass and buffer. The resultant evanescent wave excites fluorophores that are no more than 100 nm from the interface, thus eliminating noise from virus in the bulk solution.

Wessels et al(20) demonstrated that TIRF could be used to study the fusion of single influenza and Sindbis particles to solid supported lipid bilayers. Wessels(20)

used R18 dequenching to detect fusion. This work showed that dequenching of a single influenza virus occurred on the order of 100 ms. However, it is impossible to known how much R18 partitions into the inner leaflet of the viral membrane, because R18 can "flip-flop"(25, 26) across the bilayer. Thus, the typical dequenching spike is not a definitive indicator of complete pore formation, but reports only on "hemifusion", which the fusion of the two outer-most leaflets of the viral and host membranes. In order to accurately distinguish hemifusion from pore formation, an additional dye must be used to label the internal contents of the viral particle to indicate its release from the virus.

Floyd et al(21) developed a two-color fluorescence assay to differentiate influenza membrane hemifusion and full pore-formation. Viruses were bound to a supported lipid bilayer containing sialic acid receptor, GD1a. Viral particles were labeled with a green membrane dye (R110C18) to track hemifusion and sulforhodamine B (SRB), a red dye that intercalates into the viral interior. The time at which pore formation occurs is reported by a decrease in SRB intensity as the pore opens and the dye is released for the virus. Using this technique to study membrane fusion provides detailed kinetic information of both the hemifusion and pore formation processes. Kinetic analysis revealed a multistep process where the number of steps (N) occurring in the hemifusion process was approximately equal to three, confirming earlier estimates(21). Their analysis showed that three steps occurred in parallel and N represented the number of HAs that must undergo a conformational change at low pH to initiate a hemifusion event. In addition, they confirmed that the collapse of the

hemifusion stalk to form a pore is the single rate-limiting step in the membrane fusion process(27).

One of the most compelling reasons to study influenza fusion using single particle tracking techniques stems from the process of producing high titers of influenza virus for vaccine production and anti-fusogenic drug testing. For development of anti-fusogenic drugs, antibody therapies and vaccines, a high titer of virus is required for testing. This is achieved by infecting large batches of embryonated chicken eggs with the clinical virus strains in a method first developed 50 years ago(28, 29). Various studies have shown that passaging virus in eggs alters the composition of the HA making it significantly different from the wild-type virus(30, 31). In chapter 2, we use single virion fusion assays to determine significant differences in fusion kinetics between lab adapted and clinical strains of influenza.

1.4 **Difficulties associated with the single virion approach**

1.3.1 Method of initiation for pH triggered proteins

While the use of single virion tracking techniques has improved the resolution at which we can probe virus-host interactions, there are still limitations associated with this technique. One of the biggest concerns associated with typical TIRF assays is the method of buffer exchange used to simulate a low pH environment in microfluidic channels. A key aspect of determining the fusion lag times in any assay is a precise knowledge of when the pH drop occurs in the system. The timescale for the re-arrangement of HA and exposure of the fusion peptide is on the order of milliseconds(27). Thus in order to study fusion most accurately in an in vitro system,

the timescale of acidification is a key parameter to control. Typically, to mark when acidification occurs a pH sensitive fluorescent marker such as fluorescein is typically incorporated into the lipid bilayer. Thus when the fluorescein intensity decreases, low pH has been reached in the system. However, there are inherent difficulties in using hydrodynamic flow to initiate fusion. The binding affinity of HA to sialic acid is weak and flowing buffer through the system shears viruses. This shear force can not only remove particles from the bilayer and carry them along with the flow, but could also induce a deformation in the viral envelope or fusion protein. Simulations have shown spherical vesicles tethered to a surface undergo a slight morphological change when under the influence of a shear force(32).

Photo-dissociation of nitrobenzaldehyde has been studied by transient absorption and photo acoustic methods(33). Upon UV excitation, the nitronate ion of the cage compound is rapidly produced through intramolecular proton transfer reaction and protons are released into solution, resulting in a change in pH in the local environment *(33)*. Caged compounds have been used in the investigation of the mechanisms of organized biological systems such as the active transport of proteins in muscle fibers (34) protein folding kinetics(35, 36) and proton transfer in green fluorescent protein(37). Proton cages are advantageous because they induce a rapid, localized pH change on the order of microseconds that is orders of magnitude faster than the buffer exchange, which can take up to five seconds. Also, the reaction occurs in a completely quiescent environment, removing any artifacts induced by shearing buffer flow. In chapter 2, we describe the integration of proton cages into the individual virion tracking assay and the impact on membrane fusion kinetics.

1.3.2 Studying viruses that utilize membrane proteins as receptors for entry

One of the biggest drawbacks when using single virion assays to study virus entry is the limited range of enveloped viruses that can be studied. Viruses like influenza or vesicular stomatitis virus (VSV) are studied because their cellular receptors are easily integrated into supported lipid bilayers. However, the receptors for many enveloped viruses are membrane proteins. The receptors for the coronaviruses, SARS and MERS were determined to be angiotensin-converting enzyme 2(38) and dipeptidyl-peptidase 4(39) respectively. Coronaviruses have been precluded from study in single virion fusion assays because of the difficulty associated with embedding functional, membrane proteins in supported lipids bilayers. Usually, proteins are incorporated into vesicles by using detergent to solubilize the membrane protein of interest, which is then reconstituted into a vesicle called a proteoliposome(40). When membrane proteins are solubilized, they are extracted from their native environment exposing the hydrophobic transmembrane domains to an aqueous environment. To minimize these energetically unfavorable interactions, the proteins refold and this can result in incorporation of misfolded proteins into proteoliposomes and hence supported bilayers. The conformation of membrane proteins involved in viral entry is crucial and it is of utmost importance when analyzing the steps in pathogenesis. To overcome this limitation, we have developed a method of embedding, functional, enzymatically active membrane proteins in supported bilayers by utilizing chemically induced cell blebbing(23). Cell blebs are spherical membrane protrusions that are produced by contractions of the actin

cytoskeleton. When the plasma membrane locally detaches from the cytoskeleton, the hydrostatic pressure in the cytoplasm drives membrane expansion by forcing cytoplasmic fluid through the cortex hole (41). This causes the membrane to detach further from the actin cortex eventually resulting in vesicles pinching off the cell membrane. Blebs are a common marker of apoptosis but blebs are also observed in healthy cells during cytokinesis and cell spreading(42).

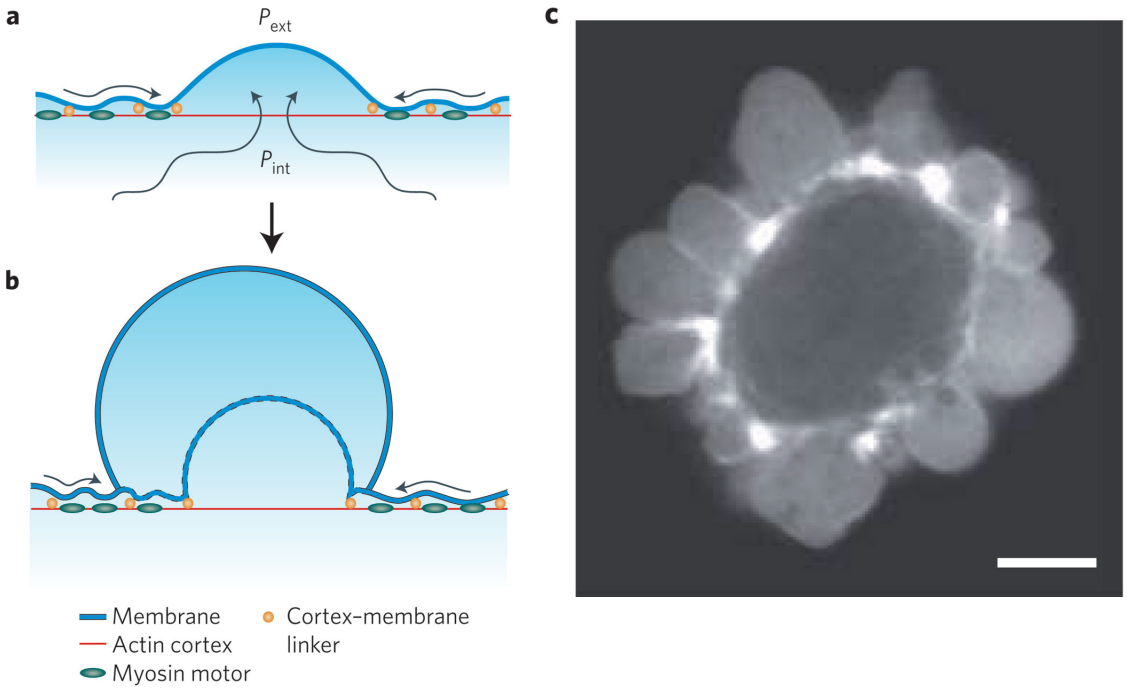

Figure 4 adapted from Dogterom et al (41) shows bleb initiation after detachment of plasma membrane from the actomyosin cortex (a) and expansion due to difference in cytoplasmic pressure (b). A confocal-microscopy image (c) of of multiple membrane blebs forming on a single cell . The scale bar in (c) is 5um

Chemical induction of blebs in cell culture was first observed in the 1970s . Blebs are induced by incubating cells with buffer containing millimolar concentrations of formaldehyde and dithiotreitol (DTT)(43-45). Chemical induction of cell blebs

produces vesicles containing transmembrane proteins that have never been subjected to solubilization and are ideal for use in biomimetic systems to study virus-host interactions. We adsorb membrane blebs, from cells transfected with receptor proteins specific for coronaviruses to a glass substrate, and then incubate with liposomes devoid of proteins. Rupturing of the liposomes in spaces between adsorbed blebs induces the rupture of the cell blebs on the substrate(23). In chapter 3, we describe using cell blebs to create, cell membrane-like supports containing coronavirus receptors, to demonstrate the first single virion coronavirus fusion studies. This new technique could potentially be extended to any membrane-enveloped virus that binds proteinaceous cellular receptors.

1.3.3 Investigating fusion kinetics of highly pathogenic viruses

In chapters 4 and 5, we will show that the single virion fusion assay can be extended to studying systems of highly pathogenic viruses. In biosafety level 2 laboratories, pathogens such as pandemic influenza viruses cannot be handled. Studying native viruses like, H2N2, H5N1 and SARS is confined to biosafety level 3 containment. However, for studying virus-host entry mechanism, it may be sufficient to use a system wherein only the fusion proteins from high path viruses are expressed in pseudotyped viruses. A pseudotyped virus has the envelope protein of a heterologous virus on the backbone of another virus, usually vesicular stomatitis virus (VSV) or murine leukemia virus (MLV). Viral pseudotypes provide a safe method for studying highly pathogenic viruses and an effective way of delivering genes for therapeutic uses. However, production of the pseudoviruses can still be quite complex.

One significant drawback of pseudotyping is the presence of viral RNA in the pseudoparticles. Even though pseudotypes have an inherent life span of one infection cycle, in the case of retroviral systems, there are still some safety concerns regarding human exposure since retroviral DNA is integrated in cellular DNA to complete it's life cycle. A safer and simpler approach would involve the use of RNA free systems. In chapter 4, we describe a simple approach to making virus-like proteoliposomes (VLP) by using the cell blebbing technique to create liposomes from plasma membranes containing viral envelope proteins(46). VLPs are RNA free and we show that they are capable of undergoing membrane hemifusion and pore formation mediated by fully functional transmembrane HA proteins. Due to the flexibility of the system, VLPs could also have a significant impact on delivery techniques for proteins and therapeutic agents.

CHAPTER 2

INFLUENZA VIRUS-MEMBRANE FUSION TRIGGERED BY RAPID PROTON UNCAGING FOR SINGLE PARTICLE STUDIES OF FUSION KINETICS

2.1.Introduction

Fusion of cell membranes is a ubiquitous biological process involved in vesicle fusion to membrane synapses, fertilization between sperm and egg cells, the merging of intracellular lysosomes, and membrane-enveloped virus fusion to endosomes(47). The fusion step is critical to the delivery of material across membranes. For example, in virus infection, membrane-enveloped viruses, such as influenza, infect cells via the endocytotic pathway, which necessitates the merging of the viral membrane with the endosomal membrane to pass viral genetic material into the cytosol. For many enveloped viruses, a drop in endosomal pH triggers conformational changes in the viral coat proteins required to initiate fusion between the viral and endosomal membranes(48). Characterization of virus fusion kinetics is important for a number of

reasons beyond understanding fundamental fusion processes, such as classification of viral strain virulence and in the development of anti-fusogenic drugs(49). Yet, directly studying fusion *in vivo* is difficult because it occurs inside intracellular compartments that are cumbersome to control and assay. Therefore, much of what is known about virus fusion has been determined using bulk or ensemble *in vitro* fusion assays that report on the collective fusion behavior of many viruses to model membranes(5, 50-58).

In bulk fusion assays, virus fusion is typically reported by a collective change in intensity resulting from fluorescence dequenching upon fusion of an ensemble of fluorescently-labeled viruses to model membranes(5, 50, 52-59). Fusion is initiated by acidification of the bulk solution. From the resulting temporal change in the fluorescence signal, some information about the kinetics of virus fusion can be obtained. Many studies of virus fusion to date have been conducted using this type of assay(5, 50, 52-59), but there are significant limitations with this approach. First, because individual events cannot be observed in this assay, viral binding and fusion cannot be distinguished from each other; this constraint impedes the separation of transport limitations from the fusion kinetics. Second, as the output signal is an aggregate of fluorescence changes resulting from many stochastic fusion events, only averaged information can be obtained from these assays; this drawback can obscure processes that occur at shorter timescales. Third, temporal limitations in uniformly acidifying the solution can spread initiation times of individual events, impacting signal response and its analysis. This limitation can reduce the temporal resolution of the measurements and obscure the sensitivity of initiating pH on kinetics(60).

Direct observation of individual virus fusion events circumvents many of the drawbacks of ensemble methods. Single particle virus fusion methods were first developed around the early 1990's(61-63), and have improved significantly since then with modern electronics and optics capable of single molecule fluorescence detection, microfluidic approaches for fluid handling, and new strategies for creating robust membranes. More recent work has provided information on the kinetics of intermediate steps of the fusion mechanism by employing total internal reflection fluorescence microscopy (TIRF)(64) to detect individual virus fusion events to solid-supported lipid bilayers (SLBs) adsorbed to the walls of microfluidic devices(20, 21). Although today's single particle virus fusion studies are easier to implement and can provide more insight into virus fusion than previously possible, two significant limitations of this approach remain: the rate at which acidification can be achieved in the confined space of the microfluidic device via acidic buffer exchange and the subsequent shearing that is imposed in the channel due to the flow.

Here we describe a method to achieve rapid acidification under quiescent conditions by integrating a photoisomerizable compound, *o*-nitrobenzaldehyde (*o*-NBA) into our single particle fusion assay. *o*-NBA donates a proton to the surrounding solution when illuminated with a 355 nm long-wave ultraviolet laser(65) with release times on the order of microseconds(66). This acidification method will hereafter be referred to as "proton uncaging". The photolysis of *o*-NBA to create a pH jump has been used in the investigation of the mechanisms of biological systems because it offers very high time resolution for kinetic measurements. In a review by McCray *et al*.(65), applications for uncaging are highlighted that include the study of active

transport of proteins in muscle fibers, mechanistic studies of ion channels, and time-resolved responses of bacterial flagella motors to rapid changes in extracellular pH. Abbruzzetti *et al*.(35) used it to examine the dissociation kinetics of histidines in Gu HCl-unfolded Fe(III) cytochrome C to increase the temporal resolution of data acquisition and allow for investigation over a wider temperature range. Saxena *et al*.(37) studied the kinetics of proton transfer in green fluorescent protein (GFP) using *o*-NBA, as a model system for characterizing the correlation between dynamics and function of proteins in general. Each of these examples illustrates the advantages of using a rapid pH jump to study pH-dependent kinetic processes. To the best of our knowledge, however, uncaging has not yet been employed for the study of pH-dependent fusion kinetics of enveloped viruses to host membranes.

There are several advantages of an uncaging strategy that are particularly beneficial for kinetic studies of viral fusion. First, the rate of release of the effector molecule (a proton) is much faster than rapid exchange of solution. Second, the effector molecule can be released close to the target, i.e., the fusion protein. Increasing the certainty of when the acidification occurs and ensuring the coordinated initiation of fusion events improves the resolution of fusion kinetics. Uncaging times are much faster than the protein conformational change for influenza hemagglutinin (HA) X:31 at the optimum triggering pH of ~ 5.0(27). A third advantage is that the environment in which the dynamics are studied is unperturbed by external forces resulting from hydrodynamic flow. The quiescent surroundings more closely mimic the endosomal environment and eliminate the possibility of hydrodynamic deformation of protein structures, which could (slightly) change the conformation of

the protein-receptor complex and impact fusion kinetics. Fourth, the absence of flow makes it possible to follow multiple processes (e.g., binding, hemifusion, pore formation) within an individual virion without it leaving the field of view.

By adjusting the concentration of *o*-NBA, the triggering pH immediately following uncaging can be tuned to achieve pH values within the range of physiological fusion pH for influenza. The characterization of the pH change in nanoliter volumes is a challenge, however, as the UV irradiation triggering proton uncaging also typically bleaches pH sensing reporter dyes. In order to be able to quantify pH a more UV resistant sensor probe thus had to be developed.

In addition to presenting a new method of initiating viral fusion in a quiescent environment we also show the utility of using single particle fusion techniques to investigate the effect of laboratory adaptations of influenza on fusion kinetics. Laboratory adaptations are antigenic and morphological changes, which occur when influenza virus is passaged repeatedly in eggs to increase the viral yield. Virus is injected into the allantoic cavity of embryonated eggs, harvested, inactivated and purified. Some clinical human strains do not grow to a high titer in eggs and have to be passaged through eggs over and over until a high yield is achieved, resulting in egg-adapted viruses(67-69). Egg adapted viruses exhibit markedly different receptor specificities morphology from clinical isolates. Human strains that are forced to passage through eggs can change receptor specificity from human type linkages α,2-6 sialic acid to avian α,2-3 linkages. It has also been shown clinical isolates of influenza virus typically contain a filamentous population, but after multiple passages in eggs virions become more pleiomorphic(70-72). We use the individual virion fusion assay

to compare the fusion kinetics of the lab adapted strain X:31 (A/H3N2/Aichi/1968) to another lab adapted strain , A/H3N2/Udorn/1972, and less adapted strain from recent clinical isolates, A/H3N2/Brisbane/2007.

2.2. Materials and Methods

The sources of all materials and detailed methods, image processing, and data analysis are described in the Appendix A. Described here are the major features of the assay and its execution.

2.2.1. Supported Lipid Bilayers

The following lipids were used in these experiments: 1, 2 dioleoyl-*sn*-glycero-3-phosphocholine (DOPC), 1-oleoyl-2-palmitoyl-*sn*-glycero-3-phosphocholine (POPC), cholesterol, and total ganglioside extract (bovine, brain). Lipid vesicles were prepared using a molar ratio of 4:4:2:0.5 of DOPC, POPC, cholesterol and total ganglioside extract. For acidic flow experiments, 0.01 mol% Oregon green DHPE lipid was added to the bilayer formulation to signal the pH drop. A detailed procedure for making liposomes used to form the supported bilayers and characterization can be found in the Appendix A.

2.2.2. Virus Labeling

Influenza X:31 (H3N2) with a hemagglutinin (HA) concentration of 2 mg/ml (as determined by Charles River Labs) was used in all experiments. Virus membranes

were labeled with lipophilic fluorophores, octadecylrhodamine B chloride (R18), a red-emitting fluorophore, or Rhodamine 110 octadecyl ester (R110C18), a green-emitting fluorophore, at sufficient concentrations to (semi-) quench fluorescence, following slight modifications to standard procedures(50, 73) as described in the Appendix A. Virus internal contents were labeled with Sulforhodamine B (SRB), a red-emitting fluorophore, as described in the Appendix A.

2.2.3. C dot pH Sensor Synthesis and Characterization

Fluorescent core-shell silica nanoparticles (Cornell or C dots) sensors were synthesized via a modified Stöber synthesis(74, 75). In contrast to earlier ratiometric two-color sensor particles(76, 77), here only single-color C dot sensors were required as pH sensing was performed in environments homogeneous on the length scale of the optical microscope resolution. To that end, first, Oregon green maleimide was conjugated with MPTMS at a molar ratio of 1:50 (dye: MPTMS) in dimethyl sulfoxide under nitrogen for 12 hours. The dye conjugate solution was then added to an ethanolic solution of 0.02 M ammonia and 4.275 M deionized water at a final concentration of 1.7×10^{-5} M dye conjugate. To this, a pure silica precursor, tetraethylorthosilicate, TEOS, was added at a concentration of 0.05 M. After reacting for 12 hours the cores were coated with a shell of additional TEOS (0.140 M) added in 31 equal aliquots at 10 min intervals. The C dots were allowed to react for 12 hours after the shell addition, and were then dialyzed to deionized water. The particles in water were then densified by heating at 120 °C in a tightly sealed reaction vial for 48

hours. This post-synthesis densification step provided improved UV stability of the encapsulated dye (data not shown). The final size of the single-color C dots sensor was determined by dynamic light scattering using a Malvern Zetasizer Nano, indicating an average diameter of 28 nm.

2.2.4. TIRF Microscope Configuration

Fusion assays were carried out using total internal reflection fluorescence microscopy using an inverted Zeiss Axio Observer.Z1 with a α Plan-Apochromat 100x oil objective with a numerical aperture (NA) of 1.46. Index-matching liquid (Carl Zeiss, Inc.) was used to couple the glass coverslip of the flow cell device to the objective. In this setup, two lasers can be used simultaneously to excite different color fluorophores; we used 561 nm and 488 nm excitation wavelengths from solid-state lasers. These were coupled into the optical pathway of the microscope using a Laser TIRF 3 slider (Carl Zeiss, Inc.), which controlled the angles of incidence. Exceeding the critical angle (~ 62°) ensured total internal reflection of the lasers and created evanescent waves about 100 nm thick. The evanescent waves excited fluorescently-labeled virus bound to sialic acid groups of the ganglioside lipids comprising the lipid bilayers, which was positioned within several nanometers of the glass-water interface. The excitation laser light was band-pass filtered through a Semrock 74 HE GFP/mRFP filter cube, and then combined with a dichroic mirror before being focused on the outer edge of the back aperture of the objective. The fluorescence emission signal was filtered through a 525/31 and 616/57nm dual band-pass emission filter and then sent to an electron multiplying CCD camera (Hamamatsu ImageEM C9100-13, Bridgewater, NJ). For acid flow and dual labeling experiments, the emission was passed through a

splitter (Photometrics DV2) to divide and focus green and red channels onto separate regions of the EMCCD camera.

Supported lipid bilayers were formed in the flow cell via vesicle fusion(78-80) by drawing a 10% dilution of liposomes into each channel at a flow rate of 100 μl/min for one minute using a syringe pump (PHD 2000 Infuse/Withdraw, Harvard apparatus, Holliston, MA). After one minute, the flow rate was reduced to 10 μl/min for 10 more minutes and then stopped to allow the channel to incubate for an additional 10 minutes. After this incubation, a fresh solution of liposomes was drawn into the channels and incubated for an additional five minutes to ensure a defect-free bilayer and complete coverage of the channel walls. The channels were then rinsed with buffer A (150 mM NaCl, 1.5 mM MES, 5 mM citric acid) for two minutes at 100 μl/min to remove unfused liposomes. Labeled virus was then pumped into the channels at 30 μl/min and allowed to incubate for 20 minutes. After the first incubation, additional virus was pumped into the channels, incubated for 10 minutes, and repeated until the desired surface density was reached. After the final incubation, *o*-NBA solution (buffer B - see *Appendix A* for preparations) was drawn into the channels at 100 μl/min for three minutes. We note that no fusion was observed during the flow steps in any assay at any condition we used. The *o*-NBA solution was then incubated in the channel for 20 minutes to reduce any residual convection in the channel after pumping ceased.

The pH drop was initiated by irradiating a 100 μm diameter section of the channel with a 4 mW UV laser for 200 ms. The beam diameter was measured to be

approximately 100 μm, thus when the beam was centered in the field of view of the microscope, it actually covered an area greater than the field of view. We ensured that the uncaging was uniform by mapping out the fusion events across the field of view in time, as shown in Figure A1 in Appendix A. The alignment of the laser is critical to ensuring that the uncaging is not biased; this can be achieved using a fluorescently-labeled bilayer in an extra channel to map out the precise alignment prior to uncaging in virus-filled channels. Using this method, the time of the pH drop is known precisely, as the cleavage of protons from the *o*-NBA molecules occurs on the order of microseconds(66). The lag between the closing of the UV shutter and the opening of the camera shutter was 200 ms. The UV flash time was 200 ms. Because of the accurate time control of this technique, it removed the requirement for a pH sensitive fluorescent probe to be present in the lipid bilayers to mark when the change in pH occurred. These probes can potentially interfere with the fusion and increase background noise in the images. Hemifusion lag times are defined as the time elapsed between acidification of the field-of-view and fluorescence dequenching for individual virus particles. Pore formation lag times are defined as the time between the start of the hemifusion step and the start of the release of the internal viral fluorophore.

The de-protonation of *o*-NBA resulted in a pH decrease from 7.0 to 5.4, 4.9, 4.6, depending on the amount of *o*-NBA added to the buffer (see *Appendix A* for exact formulations of the buffers). Fluorescence images of the viral fusion events were collected at 50 ms intervals for two minutes. In a few cases, images were taken for longer times to ensure all fusion events were captured within the typical two minute acquisition time.

2.2.6. Execution of the Acidic Buffer Flow Exchange Assay

In this experiment, the formation of bilayers, virus binding, and rinsing steps were conducted as described above. Here, instead of initiating hemifusion using the proton uncaging method, hemifusion was initiated by flowing buffer A (150 mM NaCl, 1.5 mM MES, 5 mM citric acid) pre-calibrated over a range of low pH values into the flow-cell at a flow rate of 100 μl/min for two minutes. The time at which acidification of the flow cell occurred was marked by a marked decrease in fluorescence of Oregon green DHPE present in the supported bilayer for this purpose. Images were collected at an interval of 100 ms for three or four minutes.

2.3. Results and Discussion

2.3.1 The Individual Virion Fusion Assay

We monitored individual influenza X:31 (H3N2) virus fusion events occurring inside a microfluidic device that had its walls coated with supported lipid bilayers to mimic the endosomal membrane. Supported lipid bilayers have served as excellent cell membrane mimics in numerous applications since their introduction in the 1980s(78) because they are chemically tunable and preserve the two-dimensional fluidity of constituents. This fluidity is key, as influenza is capable of multivalent binding to sialic acid receptors present in the bilayer. In this application, we employed a bilayer containing a mix of sialic receptors for virus binding. Once the bilayer formed in the device, fluorescently-labeled virus was introduced into the channel and bound to the supported bilayer as described in *Materials and Methods*.

The microfluidic device was coupled to a total internal reflection fluorescence microscope, as illustrated in Figure 1, A, and used to image the individual virus fusion events. After fusion initiation by acidification, fluorescence dequenching of a green fluorophore in the viral membrane signals the onset of the merging of the opposing leaflets of the virus and the supported bilayer, called "hemifusion." The fluorescent "spike" and "cloud" features are easily monitored with TIRF(20, 21) because TIRF is a surface-specific technique that effectively eliminates any fluorescent signal from the bulk that might obscure single fusion events. Pore formation is marked by radial diffusion of a red fluorophore originating from inside the virus, co-localized with the green fluorophore. A sequence of images showing these features is given in Figure 2, A and is described in more detail in the *Appendix A*..

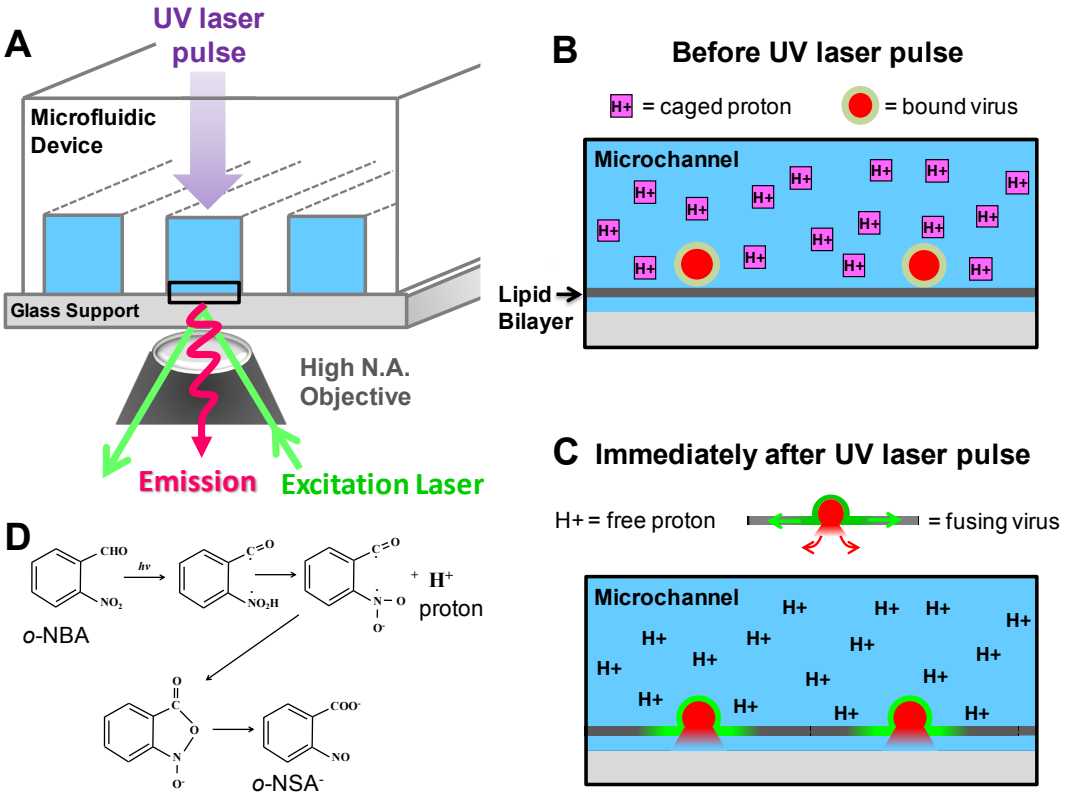

Figure 1.(A) An illustration of the microfluidic device coupled to a TIRF microscope for imaging individual

virion fusion events. The purple arrow entering the top of the device represents a UV laser that is aligned directly with the microscope objective beneath the device. Note that the dimensions of this drawing are not to scale. The actual channel is about 1 mm wide by 70 μm high and the diameter of the UV laser beam is about 100 μm. (B) An inset of the region within the field of view of the camera, drawn as the black rectangle in (A), prior to UV irradiation at a neutral pH. This illustration shows that the glass surface comprising the fourth wall of the microchannel is coated with a solid supported lipid bilayer (gray). Virus labeled with a quenching concentration of fluorophore is colored light green with a red interior. The dark pink boxes represent proton cages (*o*-NBA) that release protons when illuminated with 355 nm light. Note that this drawing is also not to scale; influenza virus is typically 100 nm in diameter and the bilayer is ~ 4 nm thick. (C) Immediately following UV irradiation the caged protons are released (denoted as free H+ in the diagram), acidifying the surrounding solution. Fusing viruses are now colored bright green to denote the dequenching of green fluorophores and the escape of the internal red dye upon pore formation. (D) The photochemistry of uncaging: the conversion of *o*-nitrobenzaldehyde to *o*-nitrosobenzoic acid and a proton upon irradiation with UV light.

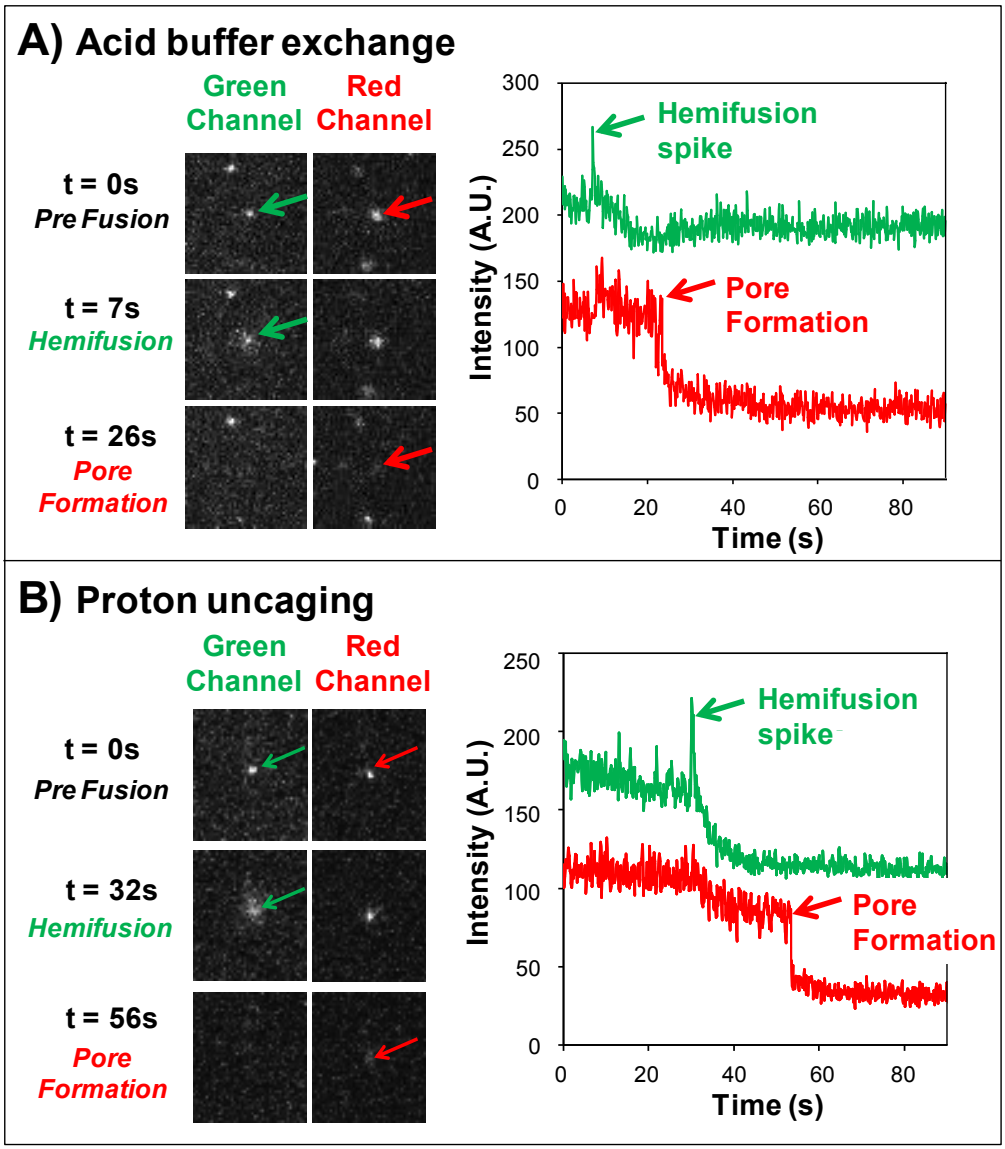

Figure 2. (A) Virus fusion initiated by acidic buffer flow exchange. Green and red fluorescence images of a single fusing virus, marked by the arrows. After acidification, the green channel shows the hemifusion of the membranes; the spike in fluorescence is observed in the plot to the right. The red channel shows the radial diffusion of the internal red fluorophore after pore formation. The drop in red signal can be observed in the plot to the right; here it takes ~ 20 seconds between hemifusion and pore formation. (B) Virus fusion initiated by proton uncaging. Here it takes ~ 15 seconds between hemifusion and pore formation.

The fusion process is hypothesized to occur in several steps(54, 57, 58, 81, 82). First, the viral fusion protein, HA, undergoes a conformational change from a prefusion folded state to an extended state, exposing hydrophobic fusion peptides, which insert into the host membrane. This intermediate undergoes an additional conformational change, which brings the two distal leaflets of each membrane close to each other, causing them to merge. Merging of the outer leaflets results in the creation of a hemifusion stalk, aided by the concerted action of several HA trimer units. We will hereafter refer to this coordinated unit as a "fusogenic complex." Eventually this structure transforms into a fusion pore through which the viral RNA escapes the endosome and enters the cytosol of the cell. Each step and conformational intermediate has a characteristic lifetime; here, we focus on measuring the kinetic rate constant leading up to the hemifusion step and the lag time for pore formation following hemifusion. In this work, we compare the fusion of fluorescently-labeled influenza virus to solid-supported lipid bilayers inside microfluidic channels initiated by the traditional acidification method (acidic buffer exchange by flow) and the proton uncaging method (Figure 1).

As both a validation of our assay setup and a control case, we initiated virus fusion by acidic buffer exchange, i.e., by flowing an acidic buffer through the microfluidic channel, not by uncaging. Initially, virus was introduced into the microfluidic device at pH 7.0 and allowed to bind. Unbound virus was gently rinsed from the channel with buffer at pH 7.0. Subsequently, citric acid buffer at various pHs was sent through the channels at a rate of 100 μl/min. We chose this specific flow rate for several reasons. First, we wanted to match conditions as closely as possible with previously published

reports(21). Second, we selected this moderate flow rate as a compromise between fast flow (for rapid delivery of protons) and slow flow (to minimize shear rates). The rate of buffer exchange must be low enough to minimize tearing viruses off the receptors and/or stretching of the protein conformations, which could cause non-native fusion protein-proton interactions and impact kinetics. Balancing these constraints, the 100 μl/min flow rate leads to acidification times for the field of view at 100x magnification of several seconds, as measured by the drop in fluorescence of a pH-sensitive fluorophore (Oregon green DHPE) doped into the supported bilayer. Images of the field of view were acquired just before and during acidification at 100 ms intervals. All fusion events within the field of view were recorded and cataloged by the time point at which the dequenching spike occurred immediately following acidification. A representative set of data for the frequency of events as a function of time after acidification using acid buffer exchange is shown in Figure 3, A (open black circles). These data were fit with a cumulative gamma distribution as described in the *Appendix A*. Hemifusion kinetic parameters were determined from the best fits of the data for various initiating pHs, as shown in Figure 4 (black circles). The good agreement with previously reported values(21) using the same experimental conditions, validates our assay and provides a point of comparison for the uncaging acidification strategy examined later.

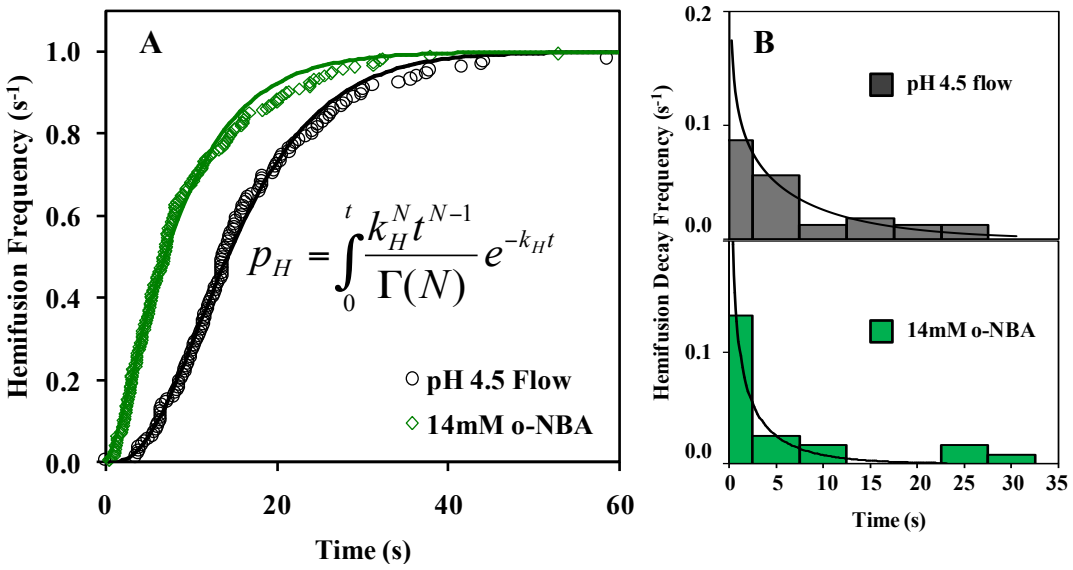

Figure 3. (A) Frequency of hemifusion events plotted as a function of time for initiation pH 4.5 obtained either by acidic buffer exchange (open black circles) or proton uncaging using 14 mM *o*-NBA (open green diamonds). The lines are the best fits to gamma function equation shown in the inset, and described in detail in the *Appendix A*. The rate of hemifusion, k_H, was 0.20 ± 0.01 s^{-1} and 0.17 ± 0.01 s^{-1} for acidic buffer exchange and proton uncaging, respectively. *N* values for acid exchange and uncaging are 3.2 ± 0.1 s^{-1} and 1.51 ± 0.05 s^{-1}, respectively. B) Histograms of lag times between the onset of hemifusion and the onset of pore formation. (Top) acidic buffer exchange; (Bottom) proton uncaging. The rate of transition from hemifusion to pore formation ($k_{H\square P}$) using the acid flow and uncaging methods was found to be 0.08 ± 0.02s^{-1} and 0.09 ± 0.05s^{-1} respectively. N was less than 1 in both cases (0.7 ± 0.1 for acid flow and 0.5 ± 0.1 for uncaging), which agrees with previous findings that there is a single step transition between hemifusion and pore formation.

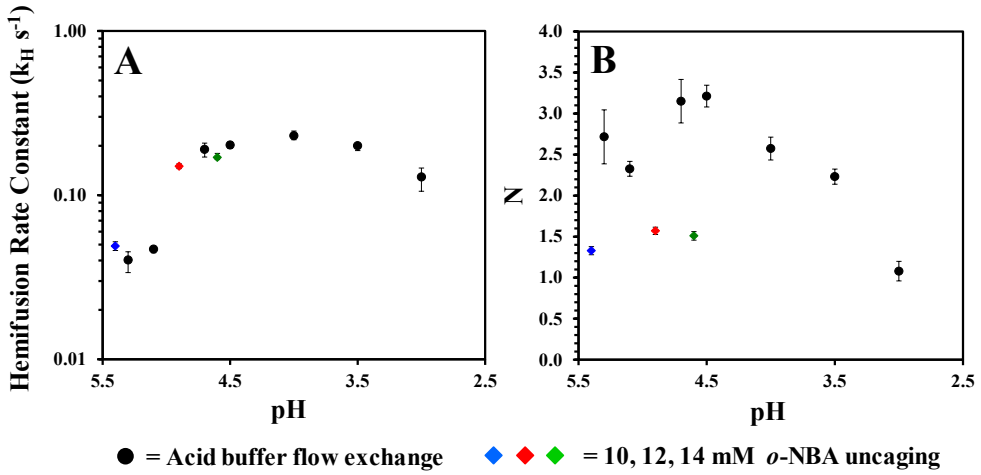

Figure 4. (A) Hemifusion rate constants, k_H, and (B) N parameters for a range of fusion initiation pH values.

The lag time between the hemifusion step and pore formation was also monitored. Previous work under similar experimental conditions has shown that pore formation lags hemifusion on the order of tens of seconds(21) and that this step is independent of pH(21, 58). A histogram for the pore formation lag time for one set of data taken at pH 4.5 is shown in Figure 4 B (top) and agrees with previous work. We note that in our case; however, a polymer cushion was not used to support the bilayer as employed in previous work(21). Despite this, our results are quite similar indicating that the polymer cushion may not be necessary for this assay. Eliminating this cushion preparation step can reduce the assay preparation time greatly.

To compare these results to the proton uncaging acidification strategy, it is imperative to know the pH following the uncaging event. But to our knowledge, there is no published characterization of the post-irradiated pH following uncaging, most likely because no reporter probe existed that could withstand the high energy

irradiation of UV without significant photobleaching. Therefore, we first report results obtained from a simple pH-sensing probe we developed to calibrate the pH in nanoliter volumes that can withstand the UV irradiation conditions in our experiment. pH-sensing single-color C dots are composed of Oregon green fluorophore encapsulated in a silica core and surrounded by a pure silica shell. As described in the *Materials and Methods* section these C dots sensors were densified in a post-synthesis heating step. Our rational for this dye-encapsulation approach was based on the fact that (i) silica is known to absorb (and therefore shield from) UV radiation, and (ii) the C dot architecture is known to improve photobleaching behavior of organic chromophores through its rigid silica matrix(83). Such particles may also find uses as pH sensors in small volumes in other microfluidic or *in vivo* applications (e.g., endosomal pH monitoring) or as novel UV sensors beyond the application presented in this work.

2.3.3. Comparison of pH-Sensing Sensitivity Between Free Oregon Green and Silica-Encapsulated Oregon Green after UV irradiation

Release of protons from *o*-NBA occurs within microseconds(66) when illuminated with 355 nm wavelength light. A pulsed diode pumped solid state laser by Teem Photonics (Model # SNV-04P-000, Lafayette, CO) was used to initiate proton uncaging in the microfluidic device. Uniformity of laser illumination was confirmed by mapping virus fusion event location in the field of view and noting that the events were random (*Appendix A*). The pH in the microfluidic channel after the 200 ms UV pulse was measured using the pH sensitive C dot sensors encapsulating Oregon green. We note here that free Oregon green (devoid of a silica shell) suffered significant

photobleaching from the UV pulse and thus could not be used as a pH sensor in this application. Other pH-sensitive fluorophores we tried also failed due to significant photobleaching. Figure 5A compares the level of photobleaching of free Oregon green and the silica-encapsulated Oregon green. This figure clearly shows that the silica capsule protects the Oregon green from photobleaching and that the level of photobleaching is not dependent on the pH of the solution.

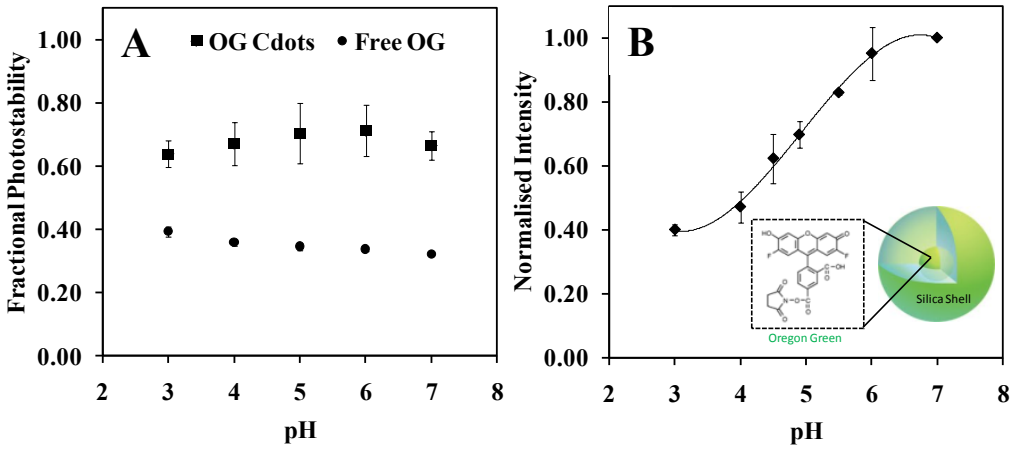

Figure 5.(A) Comparison of photobleaching between Oregon green C dots sensor and free Oregon green after exposure to UV light for 200 ms. Note that the error bars in the free OG case are within the data point. All values are normalized to the intensity value before the 200 ms UV bleach to obtain a fractional photostability at each pH. (B) Calibration curve for Oregon green C dot sensor fluorescence intensity at various pH values. All data were normalized to the pH 7.0 value so that intensities post UV irradiation could be compared directly. Note that these data were taken after irradiating the samples with UV light to account for photobleaching in the uncaging runs. (Inset) Structure of the Oregon green C dot.

2.3.4. Calibration of the Final pH after Irradiation of *o*-Nitrobenzaldehyde Buffer with UV Light Using C dots

Solutions of single-color C-dot sensors were prepared in buffer C (1.25 mM MES, ranging from pH 3 to 7). These solutions were loaded into microfluidic channels and imaged under quiescent conditions. Each channel containing a different pH solution was exposed to a 200 ms UV pulse and images were acquired at an exposure time of 100 ms for one minute. A calibration curve matching fluorescence intensity to pH (Figure 5, B) was generated by normalizing the post UV bleach intensity value of each solution to the post UV bleach intensity at pH 7 according to the following equation: $I_{calibration} = \frac{I_{bleach}^{pHX} - I_{background}}{I_{bleach}^{pH7} - I_{background}}$, where pHX is the pH of the calibration solution or the 10, 12 , or 14 mM solution of *o*-NBA in buffer C. The pH post UV pulse was then determined by matching the normalized intensity for each *o*-NBA concentration to the corresponding pH on the calibration curve. Note that this calibration curve matches well to the published Oregon green pH response curve(84) and indicates that as expected the presence of the silica shell does not impede the pH sensing ability of the Oregon green molecule.

Table 1. Post-UV pH Calibration Table for Various Cage Solutions

Concentration of *o*-NBA in buffer	10 mM	12 mM	14 mM
Intensity value	0.83 ± 0.12	0.69 ± 0.06	0.63 ± 0.01
pH from calibration curve	5.4 ± 0.5	4.9 ± 0.2	4.6 ± 0.1

It should be noted that the pH reported in Table 1 is the pH approximately 200-300 ms after the UV pulse, as there is a lag time between the laser shutter closing and the detector turning on. This delay may contribute to the variation in the measurements, as it is possible that the exact pH in the irradiated zone just after the laser hits is slightly lower than what we report here due to the diffusion of any unbound protons along the length of the channel. Because the entire channel is not irradiated with the UV light, the pH in the irradiated zone will recover (see Appendix A for details on recovery characteristics in this device). Previous work has shown, however, that the steps following the initial conformational change of the protein induced by low pH do not require a low pH environment themselves(54, 58), therefore, recovery post fusion initiation should not impact the kinetics obtained. Our work corroborates this previous work, as will be discussed later. All experiments were conducted at ambient temperature (~ 23ºC).

2.3.5. Single Particle Fusion Assay Using Proton Uncaging to Initiate Virus Fusion

In this set of experiments, acidification was achieved by proton uncaging. The chemical reaction upon UV excitation of *o*-NBA is shown in Figure 1,D: *o*-NBA undergoes an intramolecular proton transfer reaction and is converted to a nitronate ion and a proton. The nitronate ion is then converted to an *o*-nitrosobenzoic anion(33). In these experiments, virus was introduced into the microfluidic device at pH 7.0 and allowed to bind, as previously described. Buffer at pH 7.0 containing a pre-calibrated amount of *o*-NBA was used to rinse out the unbound virus. Next, a small region of the channel, pre-aligned with and encompassing the field of view of the microscope

objective, was irradiated for 200 ms with 355 nm light from a solid state UV laser to "uncage" the proton of the *o*-NBA, as shown in Figure 1 A, B. Immediately preceding and following irradiation, images were recorded at 50 ms intervals. Fusion events were detected and cataloged using the same procedure described previously for the acidic buffer exchange. A typical set of images of virus fusion initiated by proton uncaging acidification is shown in Figure 2, B. Values for k_H and N obtained from best fits of the data at various initiating pH's for buffer exchange (flow) acidification and uncaging are reported in Figure 4.

Comparing the results from the two experiments, there are important similarities and differences depending on the acidification method used (Figure 4). Interestingly, k_H stays about the same, regardless of the acidification method; however, N is reduced. N is often interpreted to be the number of protein trimers that must act concertedly to initiate fusion(21, 85). Several previous studies report a value of around three for hemifusion to occur(12, 53, 81), although prior literature includes the possibility that it could be as low as one(13) or as high as six(14, 86).

There are several possibilities that could impact fusion kinetics and explain the lowering of N in the uncaging experiment relative to the acidic buffer exchange method. These include: 1) changes in the virus fusion machinery caused by UV irradiation, 2) interactions of the *o*-NBA or the reaction product, *o*-NSA^-, with the fusion protein, 3) a significant change (drop) in the overall number of particles fusing per experiment (extent of fusion) that affects kinetic analysis, and 4) changes in the delivery rate of protons to the fusion proteins (leading to better coordination of initiation of events, more certainty of when the pH dropped, and elimination of shear

effects). To identify the cause of the change, we ran a series of control experiments. A brief summary of the results are presented here only; the details and results of these control experiments are provided in the *Appendix A*.

1) Impact of UV irradiation on kinetics. To ensure that UV irradiation itself does not trigger hemifusion or enhance fusion kinetics, a flow cell was prepared under the same experimental conditions as described previously for the proton uncaging experiment, except that it did not contain *o*-NBA. The flow cell was irradiated with the UV laser for 200 ms and then images were acquired at a rate of 200 ms post UV irradiation. No fusion events were detected. Following this data acquisition, fusion was induced by flowing acidic buffer at pH 5.1 into the channel. In this part of the experiment, hemifusion occurred as previously reported in the acidic buffer exchange experiments, indicating that prior exposure to long wave UV radiation did not affect the ability of the pre-bound viruses to fuse, in accordance with prior literature(87). k_H obtained for these conditions was 0.07 ± 0.003 s^{-1} with N value of 2.2 ± 0.10.

2) Impact of o-NBA or o-NSA$^-$ on fusion kinetics. To ensure that the presence of *o*-NBA or *o*-NSA$^-$ did not alter the fusion kinetics, we conducted fusion experiments in exactly the same way as described previously for acidic flow experiments, except the virus was incubated with either *o*-NBA or *o*-NSA$^-$ (both at pH 7.0) for 30 minutes prior to acidic buffer flow exchange. Upon acidification by acidic buffer exchange, the kinetic parameters obtained were nearly the same as in the absence of these compounds. The respective values of k_H and N obtained for each case were: 0.17 ± 0.006 and 2.1 ± 0.07; and 0.21 ± 0.01 and 2.9 ± 0.14. Thus, we confirmed that the presence of *o*-NBA, or *o*-NSA$^-$ did not lead to significant changes in kinetic

parameters compared to the acidic flow case devoid of these compounds and that only during uncaging were differences in *N* observed.

3) Assessment of changes in the extent of fusion. To ensure that there was no artifact in the kinetic analysis resulting from a reduction in extent of fusion by the proton uncaging method, we compared the extents of fusion between the acidic buffer exchange experiments and the uncaging method. We found that the overall number of virions fusing in a given experiment at a given pH were similar (Table 2). This result shows that the uncaging process has enough power to initiate the fusion of any virus present in the UV beam during the short pulse duration. We corroborated this result by irradiating the same area with a second UV pulse and found that no more fusion was initiated within a given region. Even though the UV pulse is short-lived, we obtain the same extent of fusion and hemifusion rate constants with uncaging as we obtain with the buffer exchange method; only *N* differs. Previous studies of influenza X:31 fusion after neutralization immediately following acidification show that once the fusion protein is "activated," the rest of the process does not necessarily require a low pH environment(54, 58). Therefore, the similarity of the fusion extents and hemifusion rate constants we obtain by these different acidification methods also corroborates these reports in the literature that the intermediate fusion steps are not strongly pH dependent.

Table 2. Extent of Virus Fusion Obtained with Various Fusion Initiation Methods

Fusion Initiation Method	**Extent of Fusion (%)**
14 mM *o*-NBA uncaging	27 ± 5

pH 4.5 acid flow exchange	17 ± 6
pH 4.7 acid flow exchange	25 ±7

4) Impact of the method and rate of proton delivery to the fusion proteins on kinetics. The final possibility that could explain the lower value of *N* is the immediate availability of protons to fusion proteins upon uncaging compared to the acidic flow experiments. As *N* is in the exponent of the gamma fitting equation, it will be quite sensitive to initiation time. In the case of uncaging, the acidification to the target pH is rapid: the drop is complete after the 200 ms UV pulse. In contrast, the time to drop the pH by the acidic buffer flow exchange is significantly longer (order of seconds) due to the no slip boundary condition at the bilayer surface. The impact of faster proton delivery on kinetics could be manifested in several ways. First, immediate availability of protons at the fusion protein ensures the coordination of initiation of fusion events at a specific pH value; second, faster acidification means better precision in knowing the time when acidification actually occurred (time = 0) for more certainty in determining lag times used in kinetic analysis.

To speed up the delivery of protons by acidic buffer exchange to better coordinate events, we carried out experiments at higher flow rates (500 μl/min) to ascertain the difference in the data and fits, as shown in Figure 6. With faster flow rate, we do observe a shift in the data toward the uncaging trend and a decrease in *N*; however, the effect is small with only a 5-fold change in flow rate. We are precluded from increasing the flow rate much more in an attempt to match the uncaging value because the increased hydrodynamic shear on the bound virions starts to disrupt their

attachment to the bilayer and significant shear may also lead to changes in kinetics as the HA may stretch and alter the binding pocket for the proton.

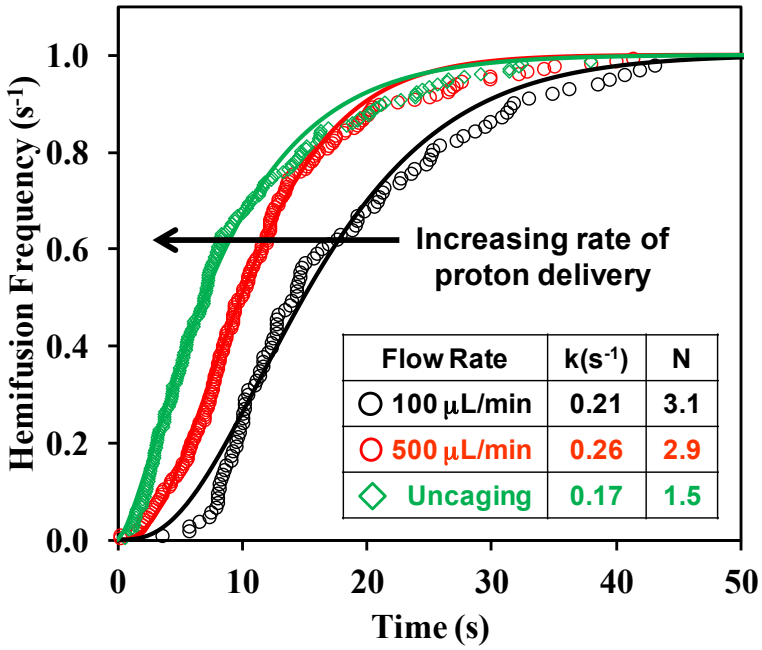

Figure 6. Fusion data at an initiation pH of 4.7. As the flow rate increases, the data trends shift closer to the uncaging data.

2.3.6. Investigating the effect of influenza laboratory adaptations on fusion kinetics

While the uncaging method of fusion initiation described above has many advantages, in order to complete a comprehensive comparison of X:31, Udorn and Brisbane, we chose to use the buffer exchange method in the following experiments so that we could probe the behavior of each strain below pH 4.5, which is unavailable in the current iteration of the uncaging method. The Udorn strain of influenza has a similar trend as a function of pH to X:31. Both strains exhibit a near linear increase in fusion

rate until plateauing at an optimal pH for fusion where the fusion rate reaches it's maximum. However, the optimal pH for fusion is approximately 5.1, which is 0.4 pH units higher than the optimal pH for X:31fusion (*figure 6*). This indicates that after endosomal uptake, Udorn can fuse with the endosomal membrane and release its genome earlier in the pathway than X:31. Interestingly, the least lab adapted strain, Brisbane has a markedly different dependence on pH. The rate of Brisbane hemifusion is almost an order of magnitude slower than X:31 and Udorn at the former's optimal fusion pHs. At higher, more physiological pHs, hemifusion kinetics for Brisbane are almost independent of pH. There are several possibilities for these differences. The source of sialic acid in the supported lipid bilayers to which all viruses bound and fused is total ganglioside extract. The main component of total ganglioside extract is GM_1, which contains α (2-3) sialic acid linkages. Brisbane is the most clinical strain and has been passaged through eggs far less than X:31 and Udorn. It is possible that the affinity of Brisbane for α(2-3) sialic acid is not as strong as Udorn or X:31 and this could slow the rate of hemifusion. Egg adaptation of influenza can also cause morphological changes. Dynamic light scattering was used to measure the average diameter of X:31, Udorn and Brisbane (see figure A3). Both X:31 and Udorn had monodisperse populations with an average hydrodynamic diameter of 140nm and 155nm respectively. However, Brisbane was found to be more polydisperse, with two populations arising at 145nm and 760nm. The second larger population may be small filaments or viral aggregates. It is very difficult to distinguish the fusing spherical virions from aggregates or filaments due to quenching of the membrane dye. It is therefore possible that a second, slower population of fusing

viruses are captured in the cumulative distribution function for Brisbane hemifusion and this results in slower fusion kinetics.

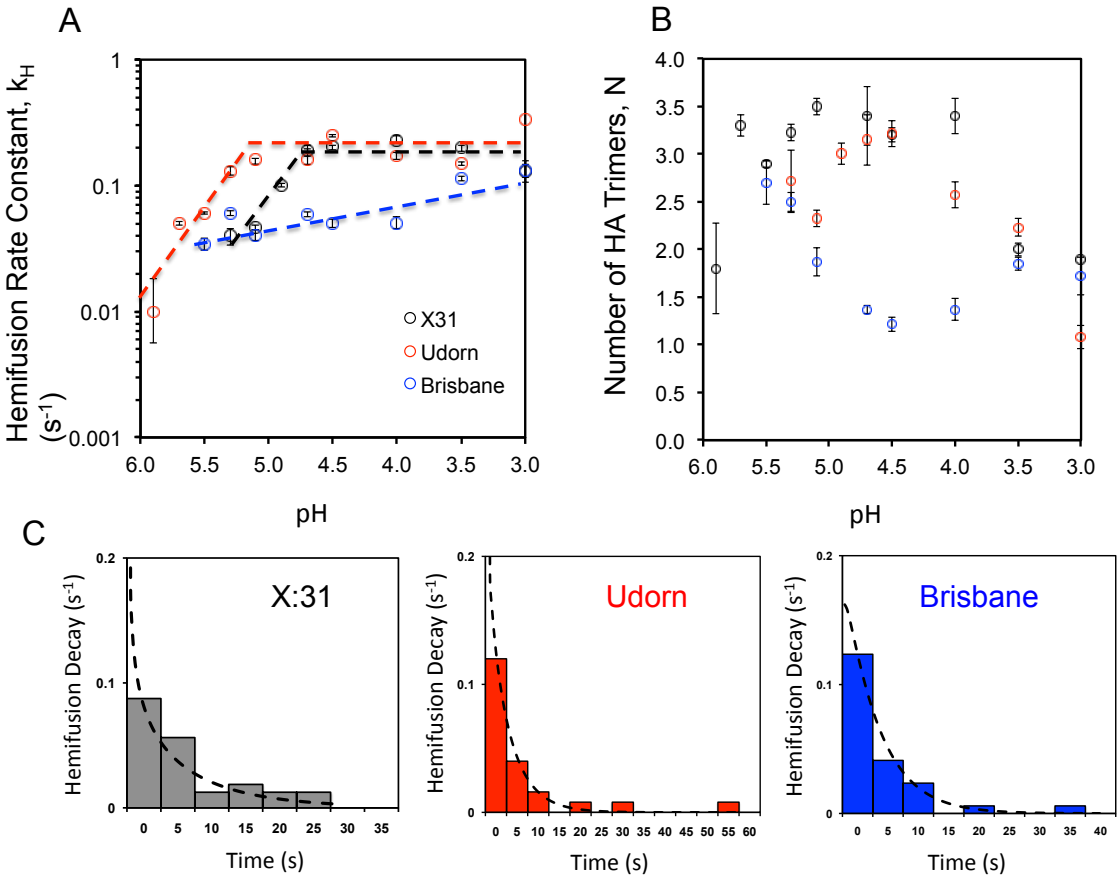

Figure 7. A) Hemifusion rate constant as a function of pH for X:31 (open black circles), A/Udorn/1972 (open red circles) and A/Brisbane/2007 (open red circles). Dashed lines are a guide to the eye and not linear fits to sections of the data . B) Number of HA trimers as a function of pH for X:31 (open black circles), A/Udorn/1972 (open red circles) and A/Brisbane/2007 (open red circles). C) Probability distribution of hemifusion decay of X:31 (grey bars), A/Udorn/1972 (red bars) and A/Brisbane/2007 (blue bars).

The rate constant for transition from hemifusion to pore formation was determined to be $0.08s^{-1}$, $0.09s^{-1}$ and $0.23s^{-1}$ for X:31, Udorn and Brisbane respectively. For each strain N was less than or equal to 1 which is agreement with

literature stating that the transition from hemifusion to pore formation is a one step process(21). We also found that the in all cases SRB was not released before R110C18 dequenched eliminating the possibility of leaky pore formation.

2.4 Conclusion

The dynamics of the HA protein conformational changes measured by variations in intrinsic tryptophan fluorescence are known to be on the millisecond timescale near pH 5.0(27). While at the "optimal" pH (4.9), the protein conformational change is not thought to be the rate-limiting step in the fusion process; at "suboptimal" pHs (5.1 and above), a slower transition to the fusogenic conformational form of HA could explain slower fusion kinetics(27). To eliminate proton transport effects on the measurement of the fusion kinetic parameters at "suboptimal" fusion pHs greater than 5.0, we used a proton uncaging strategy. The immediate availability of protons not only reduces or eliminates proton transport limitations, but also synchronizes individual initiation times, increasing the resolution of the measurements obtained from analysis of the hemifusion data. Our data are consistent with the prevailing mechanism for influenza fusion mediated by HA, and the main finding here is that the number of trimers required for fusion is closer to two rather than three.

The commercially available *o*-NBA compound employed in this work is limited by its solubility in aqueous solutions to yielding a maximum change in pH from 7.0 to ~ 4.5, thus we did not examine fusion below pH 4.5. We note that under physiological conditions, influenza fusion occurs within this pH range in the endosome. However, other more soluble proton caged- compounds can be synthesized(88, 89) and used to

study fusion at lower pH values using the uncaging method, which may be advantageous for studying other virus strains. Additionally, this approach is adaptable to studies of other membrane fusion processes (e.g., SNARE-mediated fusion) by changing the effector molecule to calcium(90, 91), for example.

The impact of this work from a practical standpoint is that obtaining higher temporal resolution measurements of kinetic parameters between different virus strains aids in characterizing mutations that lead to enhanced fusion and viral infection. Furthermore, the fusion step, and in particular the HA protein, has become a target for anti-viral drug development. Anti-fusogenic drugs, such as tert-butyl hydroquinone have been shown to strongly interact with the HA binding pocket to stabilize the neutral pH structure, which then presumably inhibits the conformational changes required for membrane fusion(49); and more recently, antibodies have been developed that target the stem region of the HA and are expected to disrupt fusion activity(92, 93). With the method described here, the inhibition of viral fusion using these compounds could be tested directly and at a level of detail not available to date. This information will further refine anti-viral drug design and characterization

Acknowledgements

We thank the NIAID Centers of Excellence for InfluenzaResearch and Surveillance (CEIRS) and, in particular, the NewYork Influenza Center of Excellence (NYICE) pilot program atthe University of Rochester (grant 414529-G to S.D. and L.P.), the Nanobiotechnology Center at Cornell University (to L.P., G.R.W., and S.D.), the National Institutes of Health (grant R0AI48678 to G.R.W.), and start-up funds from

Cornell University (to S.D.) for supporting this work

CHAPTER 3

SINGLE PARTICLE ASSAY OF CORONAVIRUS MEMBRANE FUSION WITH PROTEINACEOUS RECEPTOR-EMBEDDED SUPPORTED BILAYERS

3.1. Introduction

Coronaviruses are membrane-enveloped viruses that show a high degree of adaptability for infecting a wide range of host cells and different species. It is not well-understood how these viruses adapt to new hosts, yet they are an increasing concern as a source of emerging viruses for the human population, including SARS-CoV and the newly emerging MERS-CoV(39, 94, 95). Both SARS-CoV and MERS-CoV produce fatal disease in the majority of people who contract the infection. Quantitative studies of the entry process of the virus are therefore necessary for understanding the cues that mitigate host adaptation and for developing strategies to prevent infection. But accurately establishing the impact of various triggers on membrane fusion requires experimental techniques capable of quantifying fusion kinetics to characterize the fusion intermediates, the kinetic rate constants for transitional steps, and the fusion pathway.

A relatively new approach for quantitatively studying viral entry kinetics is single particle imaging using total internal reflection fluorescence microscopy (TIRFM)(64). TIRFM requires that a supported lipid bilayer (SLB) containing viral receptors is located within 100 nm of an evanescent wave produced by total internal reflection at the interface between two dissimilar materials. This requirement is easily achieved by

coating the walls of a glass microfluidic channel with an SLB. SLBs preserve many properties of the cell membrane, like chemical tunability, lipid diversity, and mobility of its constituents in a planar geometry, but without the experimental complications imposed by live cells. However, a significant limitation of this platform has been capturing the complexity of cell membranes, especially the incorporation of membrane proteins. This limitation has precluded studies of viruses that use proteinaceous receptors (like coronaviruses) to date. As such, these platforms have been limited to the study of a few viruses, such as influenza virus(21, 22, 96), Sindbis virus(20), and vesicular stomatitis virus (VSV)(97), because these viruses have either known glycolipid receptors or are known to interact with specific lipids that are easily incorporated into SLBs. Herein we describe a method to integrate the proteinaceous receptor for feline alphacoronavirus WSU 79-1683 (referred to here as FCoV) into a supported bilayer and measure membrane fusion kinetics using single particle tracking. Importantly, this new method of forming proteinaceous supported bilayers for virus fusion studies opens single particle fusion assays to any enveloped virus that binds to proteinaceous receptors.

To initiate infection, coronaviruses typically engage specific proteinaceous receptors on the surface of host cells. The specificity of receptor binding is believed to be one of the key factors in the host range of a given coronavirus(95). One of the best-characterized receptors is aminopeptidase N (APN), which is utilized by the majority of coronaviruses in the alphacoronavirus genus(98-100). Baby hamster kidney (BHK) cells are transfected with the feline aminopeptidase N (fAPN) and encapsulated into vesicles using a cell blebbing technique(43-46, 101). These vesicles are then used to

form proteinaceous supported bilayers to which coronavirus can fuse and be observed at the single particle level using TIRF microscopy. This method for creating proteoliposomes is in contrast to the usual approach to incorporate membrane proteins into vesicles, where proteins are reconstituted into proteoliposomes using detergent. Detergents solubilize the proteins out of the cell membrane and can result in loss of native conformation of the proteins. For pathogenesis, the conformation of proteins in the membrane and its glycosylation are critical to controlling the host-pathogen interaction. We show here that fAPN in the supported bilayer made from blebs is enzymatically active, oriented properly, and competent to bind FCoV prior to membrane fusion.

Feline coronavirus was chosen for this work because it has a well-characterized receptor (APN), grows readily in cell culture, and is not infectious in humans. FCoV, therefore, serves as a safe and effective model virus to demonstrate the use of the single particle approach to characterize membrane fusion of a virus requiring a proteinaceous receptor.

3.1.1. Membrane-enveloped virus entry via class I fusion proteins

Like influenza virus, many coronaviruses can use the endocytic pathway to enter cells(102). Once inside the endosome, the challenge for viruses is delivering their genetic material across the membrane and into the cytosol for viral replication. All enveloped viruses have membrane proteins that facilitate the fusion of their lipid envelope with the host cell membrane(103). Coronavirus particles possess at their surface the spike (S) envelope glycoprotein, which is a class I fusion protein(16).

Whereas the structure and function of the prototypical class I fusion protein, influenza virus hemagglutinin (HA), is well understood, structure-function relationships for coronavirus S proteins are not well characterized. For coronaviruses, the S protein mediates virus entry and determines cell tropism and pathogenesis(15). Like influenza virus HA, the coronavirus S protein has two primary functions: 1) it controls the binding of the virus to a cell membrane receptor, and 2) it mediates membrane fusion between the viral and host membranes(103). In general, receptor binding is controlled by the S1 domain of the protein, while membrane fusion is mediated by the S2 domain. A conformational change in the S2 domain is believed to drive the viral membrane to fuse with the host membrane. For most coronaviruses, this conformational change is triggered by the acidification of the endosome, although pH-independent fusion can also be observed.

It is generally believed that all class I fusion proteins follow a common fusion pathway that has been well-established in the prototypical class I influenza virus. Class I fusion proteins go through a multi-step process to achieve a fusion pore that begins with a fusion protein conformational change triggered by low pH. During the conformational change the fusion protein unfolds and thrusts the fusion peptide into the hydrophobic region of the host membrane. Next, the protein folds back, bringing the anchored membrane in close contact with the viral membrane until a stalk-like structure is formed. The stalk structure results from the mixing of the outer leaflet of the host membrane with the viral membrane, referred to as hemifusion. After a short lag time, the stalk is converted into a fusion pore through which the viral contents can exit. It may be necessary for multiple fusion proteins to work in concert to bend the

membrane to induce fusion.

Analogous to influenza HA, it is believed that the coronavirus S protein, undergoes proteolytic cleavage prior to fusion activation(15). Proteolytic cleavage is believed to expose specific regions of the S protein, including the fusion peptide(104). Because proteolytic cleavage dictates fusion competency, the availability of proteases in the extracellular milieu is another key factor in tropism of coronavirus. A dramatic example of this is human SARS-CoV. The bound virus is able to fuse at the cell surface in absence of acidic pH, when exposed to exogenous proteases(105). This route of entry may even be 2 to 3 orders of magnitude more efficient that the endosomal pathway(105). In this case, proteolytic cleavage *changed* the fusion pathway. By combining single particle fusion with proteinaceous supported bilayers and microfluidics, the sequence of triggers can be controlled and the associated fusion pathway and kinetics quantitatively measured.

3.2. Materials and Methods

3.2.1. Cells, plasmids, and viruses

Baby hamster kidney-21 (BHK-21) cells, obtained from the American Type Culture Collection (ATCC, Manassas, VA), were grown and maintained in Dulbecco's modified Eagle medium (DMEM, CellGro) supplemented with 10% fetal bovine serum (Gibco), 100 U/ml penicillin and 10 μg/ml streptomycin (CellGro), 1% HEPES buffer (CellGro) in a 37°C, 5% CO_2 incubator. The pcDNA-fAPN and pCI-neo-hAPN plasmids were used for transfections of BHK-21 cells. They encode the feline aminopeptidase N (fAPN) and human aminopeptidase N (hAPN), respectively, and

are generous donations from Kathryn Holmes of the University of Colorado. pCAGGS-FCoV-1683S plasmid encodes the S protein of FCoV-1683(106). The pCAGGS vector was used as an empty vector control.

Feline Coronavirus (FCoV) strain WSU 79-1683, also referred to FCoV-1683, was obtained from the Cornell Animal Health Diagnostic Center (Cornell University, Ithaca, NY). The virus was grown in canine A-72 cells provided by Dr. Colin Parish (Baker Institute of Animal Health, Cornell University, Ithaca, NY).

3.2.2. Preparation of cell blebs

The formation of cell blebs was established in the mid-1970's(101). An excellent review of cell blebbing protocols is available by Sezgin et al (43). Here, we use a blebbing procedure published previously by our group (46). For transfections, 1.5×10^6 cells were seeded in 10 cm culture dishes, and incubated for 24 hours. Transfections were performed using TurboFect transfection reagent (ThermoScientific) according to manufacturer's instructions and using 6 µg of plasmid DNA for each plate. Twenty-four hours after transfection, cells were washed twice with buffer A (2 mM $CaCl_2$, 10 mM HEPES, 150 mM NaCl at pH 7.4). 3 ml of buffer B (2 mM $CaCl_2$, 10 mM HEPES, 25 mM formaldehyde, 2 mM dithiotreitol (DTT) and 150 mM NaCl at pH 7.4) was added to each dish to induce cell blebbing. The dishes were then incubated for 1 hr at 37^oC with gentle rocking. After incubation, the cell supernatant, containing detached cell blebs, was decanted into a 15 ml falcon tube and placed on ice for 20 minutes to allow any detached cells to settle out. The supernatant was transferred to new test tube. Blebs were then dialyzed using cellulose dialysis

tubing (Fischer Scientific), in two 100 ml volumes of buffer A for 24 hours. The size of cell blebs was determined by dynamic light scattering using a Malvern Zetasizer Nano (Worcestershire, UK). The sample registered 3 peaks at approximately 38 nm, 106 nm, and 530 nm.

3.2.3. Preparation of liposomes

The following lipids/materials were used in the experiments: 1-oleoyl-2-palmitoyl-*sn*-glycero-3-phosphocholine (POPC), 1-oleoyl-2-palmitoyl-sn-glycero-3-phosphoethanolamine (POPE), 1,2-dioleoyl-sn-glycero-3-phosphocholine (DOPC), cholesterol, and sphingomyelin. These materials were all purchased from Avanti Polar Lipids (Alabaster, AL). Oregon green DHPE purchased from Molecular Probes (Eugene, OR) was used to label supported bilayers and as a pH sensor to mark acidification of the bilayer during membrane fusion experiments. Octadecyl Rhodamine (R18), a red-emitting, lipophilic fluorophore, was used to label cell bleb membranes and was purchased from Molecular Probes. We also synthesized in house a green-emitting, lipophilic fluorophore, Rhodamine 110 Octadecyl ester (R110C18), from Rhodamine 110 Chloride and 1-octadecanol purchased from Sigma Aldrich. The synthesis procedure has been published previously(22). R110C18 was used to label viral membranes during dual-labeling virus fusion experiments. Sulforhodamine B (SRB), a red-emitting, water-soluble fluorophore purchased from Molecular Probes was used to label virus interiors.

The liposome formulation used in these studies (BHK-liposome) contained POPC, POPE, sphingomyelin and cholesterol in the ratio 37.3:34.2:5.7:22.8. This

composition was formulated to match the native lipid content of BHK cells as closely as possible(107) and primarily used in the formation of bleb-derived supported bilayers.

To form liposomes, appropriate amounts of each component were mixed in biotechnology grade chloroform in a scintillation vial. For formulations containing sphingomyelin, this component was first dissolved in a 4:1 mixture of chloroform: methanol then added to the mixture. The bulk solvent was removed from the vial under a stream of high purity nitrogen gas and then placed in a desiccator under vacuum overnight to ensure complete evaporation of all solvent. Phosphate-buffered saline at pH 7.4 was added to the dried lipid film and gently re-suspended in a sonication bath (Model # BD2500A-DTH; VWR) for twenty minutes on the lowest setting. The final lipid concentration was approximately 2 mg/ml. Liposomes were then extruded twice through a polycarbonate filter (Whatman Nucleopore) with pore size 100 nm, and five times through a filter with a pore size of 50 nm. The average liposome diameter for all formulations ranged between 90 and 100 nm as determined by dynamic light scattering.

3.2.4. Fluorescent labeling of cell blebs or viruses

To visualize both the formation of the fAPN-bleb supported bilayer formation and viral membrane fusion, blebs and viruses were fluorescently labeled. To visualize fusion using a fluorescence dequenching technique, viral membranes must be labeled with a semi-quenched amount of fluorophores following standard procedures(50, 73).

In these experiments, FCoV was labeled with R110C18 according to the following general procedure.

3.2.4.1. General membrane labeling procedure (single color)

To fluorescently label the bleb membranes for the visualization of bilayer formation and photobleaching experiments (FRAP), blebs were incubated with 1µl 0.18 mM R18, dissolved in ethanol, for 15 minutes in a sonicating bath (VWR) on the lowest setting.

To fluorescently label FCoV membranes for fusion experiments, R110C18, dissolved in ethanol, was used. 5 µl of virus solution was diluted with 250 µl of buffer A and mixed with 3 µl of 2 mM R110C18 for 1 hour in a sonicating bath. In this case, it is desired to label membranes with a quenched amount of R110C18 to trigger dequenching during membrane fusion. Free R110C18, which did not insert into the membranes, was removed from the solution by centrifuging (Eppendorf, Centrifuge 5451C, Hauppauge, NY) through a G-25 spin column for two minutes at rate of 3x1000 min^{-1}. The supernatant containing the purified virus was diluted with 0.8 ml of buffer A and gently vortexed to mix.

3.2.4.2. General virus interior labeling procedure

For pore formation experiments, 5 µl of virus solution was mixed with 10 µl of 20 mM Sulforhodamine B (SRB) solution and incubated overnight. Excess SRB, which did not partition into the virus interior, was removed from the solution by centrifuging through a using a G-25 spin column for two minutes at rate of 3x1000 min^{-1}. The supernatant was diluted in 0.8 ml of buffer A prior to use.

3.2.4.3. Feline coronavirus dual-color labeling

For FCoV hemifusion experiments, it was necessary to label the membrane with a green fluorophore to distinguish it from the red internal fluorophore label. For these experiments, virus that had been labeled with SRB as described in the previous section, was labeled with 3μl of R110C18 (2 mM). The mixture was sonicated gently for 1 hour and excess dye was removed as previously described using at G-25 spin column.

3.2.5. Preparation of microfluidic devices and PDMS wells

3.2.5.1. Preparation of glass surfaces for supported bilayers

Glass microscope coverslips (25 mm x 25 mm; No. 1.5) from VWR were cleaned in piranha solution consisting of 70% sulfuric acid and 30% hydrogen peroxide. Slides were immersed in 150 ml of piranha solution for 10 minutes then rinsed for 30 minutes with copious amounts of deionized water with a minimum resistance of 18.2 MΩ·cm obtained from a Siemens Purelab Ultra water purification system. Clean slides were stored under deionized water and dried with a stream of ultra-pure nitrogen gas prior to use. For bilayer formation, glass surfaces were used either with PDMS wells or microfluidic devices.

3.2.5.2. Fabrication of Polydimethylsiloxane (PDMS) wells

To form the PDMS wells, a thin sheet of PDMS was made in a Petri dish using 10:1 elastomer/crosslinker mixture of Sylgard 184 (Robert McKeown Company; Branchburg, NJ). The PDMS was baked for 3 hours at 80ºC, cut into small squares approximately the same size as a coverslip, and a hole punched through each square to form the wells. PDMS squares were then attached to a clean glass coverslips, which formed the bottom of the wells. The approximate volume of a well was 100 μl.

3.2.5.3. Fabrication of microfluidic devices

Microfluidic devices for the fusion experiments were fabricated using soft lithography. The microchannel pattern was designed using the CAD software program L-Edit (Tanner EDA) and a master of the flow pattern was made on a silicon wafer at Cornell Nanoscale Science and Technology Facility (CNF). Each microfluidic device contained six channels. The dimensions of each channel are 1 mm wide by 70 μm deep with a total length of the channel of 1.5 cm. The spacing between the centers of each channel is 1 mm. The silicon wafer was coated with P-20 primer in a spin coater, followed by SPR220 (Megaposit) photo-resist. The wafer was baked for 90 seconds at 115ºC and then exposed to UV light for 7.5 seconds in an ABM contact aligner to pattern the wafer with the flow cell design. Following this step, the wafer was baked again for 90 seconds at 115ºC and then developed for 60 seconds in a Hamatech-Steag Wafer Processor. The pattern was then etched into the wafer using a Unaxis 770 Deep Si Etcher. The depth of the channel was determined using a Tencor P10 Profilometer.

Microfluidic devices were formed using PDMS in a molding process. To facilitate the release of the cured PDMS after molding on the etched silicon master, the master slide was first coated with Sigmacote (Sigma). A 10:1 (elastomer/crosslinker) mixture of Sylgard 184 was mixed and then degassed before pouring on the silicon master slide etched with the flow cell pattern. The PDMS was then baked for 3 hours at 80ºC. After baking, PDMS microfluidic devices were peeled off of the wafer, and inlet and exit ports were punched in each channel of the device. Both the clean glass coverslip and PDMS mold were treated with oxygen plasma using a Harrick Plasma Cleaner (Model # PDC-32G; Ithaca, NY) at a pressure of 750 μm on the high setting for 25

seconds. Gently pressing the surfaces together resulted in a tight bond between the glass and PDMS and formed the four walls of the microfluidic channel.

3.2.6. Creating supported bilayers in microfluidic channel

A solution containing a 1:4 dilution fAPN-blebs in buffer A was drawn into the microchannel at a flow rate of 30 μl/min for 1 minute and incubated on the glass surface for 20 minutes. The microchannel was then rinsed with buffer A at 100 μl/min for 2 minutes. A solution of BHK-liposomes (0.5 mg/ml) was drawn into the microchannel at 100 μl/min for 1 minute and incubated for 10 minutes. To heal any defects in the membrane, more vesicle solution was drawn into the microchannel at 10 μl/min for 5 minutes. Finally, the microchannel was rinsed with buffer A at 100 μl/min for 2 minutes to remove any excess liposomes.

3.2.7. Diffusion measurements in supported bilayers

Integrity of bilayers and diffusion of the lipids within it was examined by fluorescence recovery after photobleaching (FRAP). Bilayers were formed following the above procedures inside PDMS wells. R18 was used to label the bilayer and carry out the photobleaching experiments. Once formed, bilayers were gently scratched with a dissection tool to remove a thin section to aid in focusing on the plane of the bilayer on the microscope. Following this step, the bilayer was rinsed again for one minute with buffer A to wash out any lipids removed by scratching. A 20 μm diameter spot in the supported lipid bilayer was bleached with a 4.7 mW 488 nm krypton/argon laser for 200 ms. The recovery of the intensity of the photobleached spot was recorded for

15 minutes at regular intervals. The fluorescence intensity of the bleached spot was determined after background subtraction and normalization for each image. The recovery data was fit using a Bessel function following the method of Soumpasis(108). The diffusion coefficient is then calculated using the following equation: $D = \frac{w^2}{4t_{1/2}}$, where w is the full width at half-maximum of the Gaussian profile of the focused beam.

For protein mobility, single particle tracking at 100x magnification was conducted. Fluorescently labeled fAPN-specific antibodies (see next section for antibody and labeling details) were bound to fAPN in the bilayer and monitored for at least 40 minutes to determine if any proteins diffused during that time. **Figure S3** summarizes the protein mobility results.

3.2.8. Antibody binding to confirm presence and orientation of APN in the supported bilayer

To confirm that fAPN proteins were incorporated into the supported bilayer and the active, extracellular end was oriented facing the bulk solution (i.e., not inverted towards the glass support), the bilayer was incubated with an fAPN-specific antibody, RG4(109) (generously donated by Tsutomu Hohdatsu), which recognizes an epitope (residues 251-582)(99) located in the C-terminal ectodomain (extracellular-facing domain) of the protein. The bilayer was incubated with 1 μg/ml of a primary antibody anti-fAPN mouse monoclonal antibody (RG4) for 20 minutes. The unbound primary antibody was rinsed and 1 μg/ml of Alexa Fluor 488 conjugated-goat anti-mouse IgG

secondary antibody was added and incubated for 20 minutes. Excess secondary antibody was rinsed and the sample was imaged on an inverted fluorescence microscope with appropriate filter set, described below.

3.2.9. Functionality of APN in cell blebs and supported bilayers (APN enzyme activity assay)

Many cells and species express aminopeptidase N. APN is a membrane-bound enzyme that cleaves the N-terminal amino acids from bioactive proteins, leading to their inactivation or degradation(110). This function is believed to be integral to several biological processes including antigen processing and presentation, cell adhesion, tumor cell metastasis, neurotransmitter degradation. APN also serves as a well-characterized receptor for certain coronaviruses(111), including FCoV-1683(99) used in these experiments.

To ensure the APN proteins maintain their native enzymatic functionality in the supported bilayers, we performed an enzymatic activity assay. In this assay, the substrate for APN is non-fluorescent until the enzyme cleaves it. Therefore, functionality of APN in blebs or supported bilayers can be verified by detecting fluorescence after introducing the substrate into a cuvette of bleb solution or into a microfluidic device containing supported bilayers. For these experiments, human APN (hAPN), instead of feline APN, was expressed in BHK cells and tested for activity. This change was necessary because there is no activity assay specific for the feline APN. The control cases are the empty vector blebs or empty vector-SB.

3.2.9.1. Blebs in Solution

Blebs containing human APN (hAPN) were formed as previously described for fAPN-blebs. The activity of hAPN and empty vector cell blebs in solution was tested using bulk fluorescence measurements in fluorimeter (Photon Technologies International Inc) at an excitation/emission of 380/460nm. The substrate for hAPN, H-Ala-AMC, was purchased from Bachem. A 50:50 mixture of blebs and H-Ala-AMC substrate at 270 μM in a 50 mM Tris buffer at pH 7.4 were mixed in a quartz cuvette and intensity of the mixture was monitored for 30 minutes.

3.2.9.2. Supported lipid bilayer

Bleb-derived supported bilayers containing hAPN were formed in microfluidic channels as previously described for fAPN-SBs. The substrate, at concentration of 270 μM in 50 mM Tris buffer at pH 7.4, was drawn into the channel at a flow rate of 100 μl/min for 2 minutes. The fluorescence intensity of the channel was observed at 10x magnification at an excitation/emission of 380/455nm. A control channel containing an empty vector bleb-derived supported bilayer devoid of exogenous APN proteins was subjected to the same conditions as described above.

Figure S5 summarizes the enzyme activity assay results. In **Fig. S5a**, blebs with and without hAPN were loaded into cuvettes and the fluorescence monitored temporally using a fluorimeter after the substrate was added. The empty vector blebs show no appreciable fluorescence, while the hAPN blebs continue to increase in signal as increasing amount of substrate is cleaved during the course of the experiment. In **Fig. S5b**, supported bilayers with and without hAPN are loaded into a microfluidic

channels with substrate. The microfluidic device is monitored at specific time points and the two channels are compared in the inset. In the control case, no fluorescence is detected above the background, but the hAPN-SB shows significant intensity after several hours.

3.2.10. Cleavage of FCoV spike protein by trypsin protease (Western blot)

In order for class I fusion proteins to become fusion-competent, they must first be activated by proteolytic cleavage, a modification performed by cellular proteases. There are numerous enzymes capable of proteolytically cleaving the coronavirus spike protein. These proteases can be found in either the intra- or extra- cellular environment. For example, cathepsin proteases found in the endosomal compartment are naturally used to breakdown proteins taken up into the lysosome(112). Once a virus gets endocytosed, cathepsins can also cleave the coronavirus spike protein(102, 106, 113, 114)Trypsin is a common extracellular protease found in the digestive tract of many vertebrates(115) to break down proteins during digestion(115). We show here that trypsin is also capable of cleaving the spike protein of coronaviruses.

Cleavage likely occurs at two distinct sites for coronavirus S: at the junction of the S1/S2 domains, as well as within the S2 domain (S2')(18). Proteolytic cleavage is believed to expose specific regions of the S protein, including the fusion peptide(104). For some coronaviruses, cleavage at S1/S2 is necessary to allow subsequent cleavage at S2', and allow the S2 domain to respond a low pH trigger that initiates the conformational change required for fusion(18). In other coronaviruses, in particular

alphacoronaviruses, like FCoV-1683, the S1/S2 site does not need to be cleaved. In these cases, activation is likely mediated solely through the S2' cleavage site.

We used trypsin as a means to activate FCoV-1683 S. To confirm that trypsin can proteolytically cleave FCoV-1683 S in an appropriate manner, FCoV-1683 viral suspensions were ultracentrifuged at 42,000 rpm in a TLA 55 rotor using a Optima Max-E ultracentrifuge (Beckman Coulter) for 2 hours at 4°C. The viral pellets were resuspended in 50 µL of PBS (non treated sample), or PBS containing 3 µg/mL of L - 1-Tosylamide-2-phenylethyl chloromethyl ketone (TPCK)-treated trypsin (ThermoScientific) (trypsin treatment), or MES buffer pH 5.0 supplemented with 2.5 mM EDTA and 2 mM DTT and containing 0.5 µM Cathepsin B (Calbiochem). The samples were incubated at 37°C for one hour, except the cathepsin-treated sample which was incubated for 15 min at 37°C. All samples were then subjected to treatment with the deglycosylating enzyme PNGase F (New England Biolabs), using 2500 units and supplied buffer at 37°C for 16 hours. This was done to avoid having differentially glycosylated species of S protein. LDS loading buffer (Invitrogen) with DTT (50 mM final) was added to samples, and were subjected to 5 min 95°C incubation for denaturation. The samples were then analyzed by Western blot using FCoV-S-specific mouse mAb 22G6.4, provided by Dr. Ed Dubovi (Animal Health Diagnostic Center, New York State College of Veterinary Medicine, Cornell University) followed by incubation with HRP-conjugated goat anti-mouse IgG (AbCam).

As shown in **Fig. S6**, cathepsin B and trypsin treatment yield major cleavage products at approximately 100 kDa, while in the non-treated sample, the majority of S protein migrated as a single band around 200 kDa, indicating little cleavage event

occurred without protease treatment. These results show that trypsin cleaves FCoV 1683 S in a similar way as does cathepsin B, and are consistent with published results for this virus cleaved with cathepsin B(106).

3.2.11. TIRF microscope configuration

Membrane fusion assays were conducted with total internal reflection fluorescence (TIRF) microscopy using an inverted Zeiss Axio Observer.Z1 with a α Plan-Apochromat 100x oil objective with a numerical aperture (NA) of 1.46. Index-matching liquid (Carl Zeiss, Inc.) was used to couple the glass coverslip of the microfluidic device to the objective. In this setup, two lasers can be used simultaneously to excite different color fluorophores; we used 561 nm and 488 nm excitation wavelengths from solid-state lasers. These were coupled into the optical pathway of the microscope using a Laser TIRF 3 slider (Carl Zeiss, Inc.), which controlled the angles of incidence. Exceeding the critical angle for glass/water interface (~ 62^{o}) ensured total internal reflection of the lasers and created evanescent waves about 100 nm thick. At this thickness, the evanescent waves excited fluorophores positioned within the supported bilayer, or virions labeled R18. The excitation laser light was band-pass filtered through a Semrock 74 HE GFP/mRFP filter cube, and then combined with a dichroic mirror before being focused on the outer edge of the back aperture of the objective. The fluorescence emission signal was filtered through a 525/31 and 616/57 nm dual band-pass emission filter and then sent to an electron multiplying CCD camera (Hamamatsu ImageEM C9100-13, Bridgewater, NJ).

3.2.12. Data Analysis

3.2.12.1. Image Processing

The images acquired during the membrane fusion assays were analyzed using both ImageJ (NIH) and MATLAB (Mathworks). Fusing particles were manually selected in ImageJ and the fluorescence intensity in a 4x4 pixel region around each particle was collected as a function of time. In videos where background noise was high due to a large amount of fusion events, a rolling ball background subtraction algorithm was applied to all of the images to remove excess background noise as the fluorophores diffused into the membrane after hemifusion. The rolling ball algorithm determines the local background for every pixel by averaging over a large circular region around the pixel. This background value is then subtracted from the original image. The fluorescence trajectories for the particles were then imported to MATLAB (Mathworks) for further analysis. A code written in MATLAB determined the onset time of the dequenching 'spike' for each particle by finding the time of the maximum intensity in each particle trajectory.

The accuracy with which N and k_H can be determined depends on both the number of experimental observations and the number of steps in the process(116). To accurately estimate N from a gamma distribution a minimum number of a fusion events must occur for statistical significance. For example, to distinguish a 2-step process from a 3-step process i.e. $N = 2$ from $N = 3$, a minimum of 50 fusion events must be observed(116). The number of fusion events that occurred during each experiment reported here varied from 70 to 120.

3.3. Results and Discussion

3.3.1. Proteinaceous supported bilayer formation from cell blebs expressing APN protein

Pure liposome solutions, prepared as described in the *Methods* section, self-assemble on glass to form supported bilayers via vesicle fusion(78, 80). Proteoliposomes, on the other hand, generally do not readily form supported bilayers on their own. We discovered that proteoliposomes derived from cell blebs could be induced to form supported bilayers with the addition of pure liposomes(46). We describe this self-assembly process here in the context of forming fAPN-supported bilayers (fAPN-SB) as substrates for FCoV fusion studies. The process is illustrated in **Fig. 1 (top)** and begins with the formation of cell blebs containing fAPN. The detailed procedure for forming cell blebs containing fAPN from BHK cells can be found in the *Methods* section. fAPN blebs are then used to form proteinaceous supported bilayers, as will be described in detail next. Once the proteinaceous supported bilayer is formed, FCoV binds to fAPN, localizing the virus within the evanescent wave and enabling single particle fusion experiments that will be described in a later section.

To visualize the formation of the supported bilayer from fAPN-blebs derived from BHK cells, the bleb membranes were labeled with a lipophilic fluorophore, Octadecyl Rhodamine (R18) (see *Methods* section). A small aliquot of the labeled bleb solution was added to a PDMS well and incubated for 10 minutes at room temperature. During this time, blebs contact and adsorb to the glass surface. Excess blebs that did not adsorb to the glass surface were removed by gently rinsing the well with buffer A (2

mM $CaCl_2$, 10 mM HEPES, 150 mM NaCl at pH 7.4). At this stage, the adsorbed intact blebs stick to the glass surface as intact proteoliposomes, as seen in **Fig. 1, t = 0 image**, as punctuate spots.

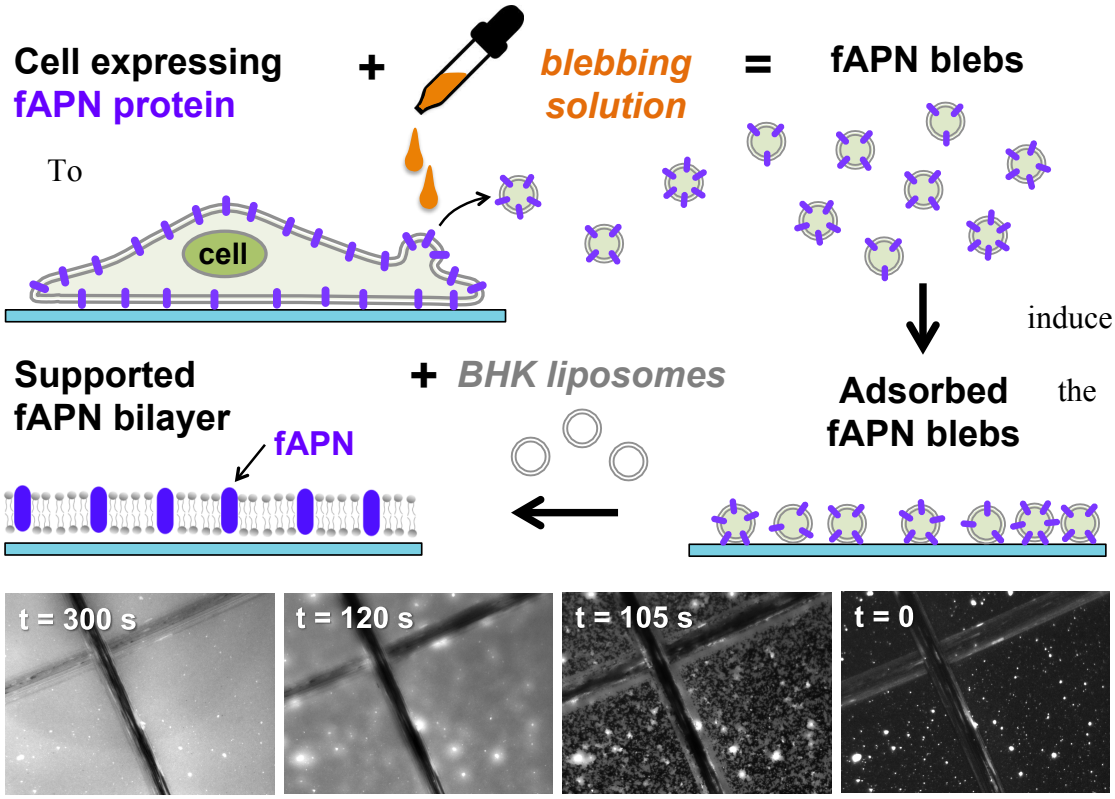

Figure 1 (Top) Illustration of the formation of a fAPN-bleb supported bilayer from cell blebs derived from BHK cells. (Bottom) Fluorescence images of fAPN-SB formation, corresponding to the above cartoon. (Left, t = 0) fAPN-blebs containing R18 adsorbed to glass substrate. Note that some larger blebs dominate the signal, but many smaller blebs are adsorbed as well. (Middle images) ~ 100 seconds after the addition of BHK-liposome solution to adsorbed blebs. Note that the BHK-liposome solution is devoid of fluorescent label, thus all signal comes from release of R18 initially confined to the bleb vesicle before rupture. (Right, t = 300 s) Continuous supported bilayer observed 300 seconds after the addition of liposomes. These images are all taken under 40x magnification. The dark lines in each image are scratches intentionally made with a dissection tool that is used to find the focal plane of the bilayer. The continuous focus of this line throughout the rupture process indicates that the focal plane not change and that the uniform distribution of fluorescence at t = 300 s is due to mobility of fluorophores redistributed throughout the newly-formed planar bilayer.

formation of a supported bilayer from the adsorbed blebs, we formulated liposomes to match closely the BHK endosomal membrane composition(107) (referred to as BHK-liposome) and added this solution to the PDMS well containing the adsorbed blebs. In this experiment, the BHK-liposomes are devoid of fluorophore labels. This labeling scheme assists in observing the formation of the supported bilayer as the initially punctuate blebs rupture and the R18 disperses throughout the newly-formed planar bilayer **(Fig. 1, bottom image series)**. Note that as the R18 spreads in the bilayer and gets diluted with the unlabeled BHK lipids, the fluorescence signal increases due to fluorophore dequenching.

Bilayer formation is verified by fluorescence recovery after photobleaching (FRAP). In this technique, a laser beam is used to photobleach a 20 μm diameter spot in the newly-formed fluorescently-labeled (R18) supported bilayer. The recovery of the fluorescence in this photobleached area is used to determine the 2D mobility of R18 embedded in the planar supported bilayer, which in turn, verifies that the R18 is no longer confined to discrete bleb vesicles adsorbed to the glass surface, but freely moving throughout a 2D bilayer plane. FRAP interrogates a macro scale area (~ microns) and thus is useful for characterizing how well the bilayer has formed over this length scale. Note that the largest population of blebs is on the order of 500 nm in diameter (**Fig. S1**), so if the blebs have not ruptured into a contiguous planar bilayer, then the fluorescence will not be able to recover after the sample is photobleached. This lack of recovery was confirmed by preparing samples containing only adsorbed cell blebs (no addition of BHK-liposomes). Photobleached spots did not recover on

these samples.

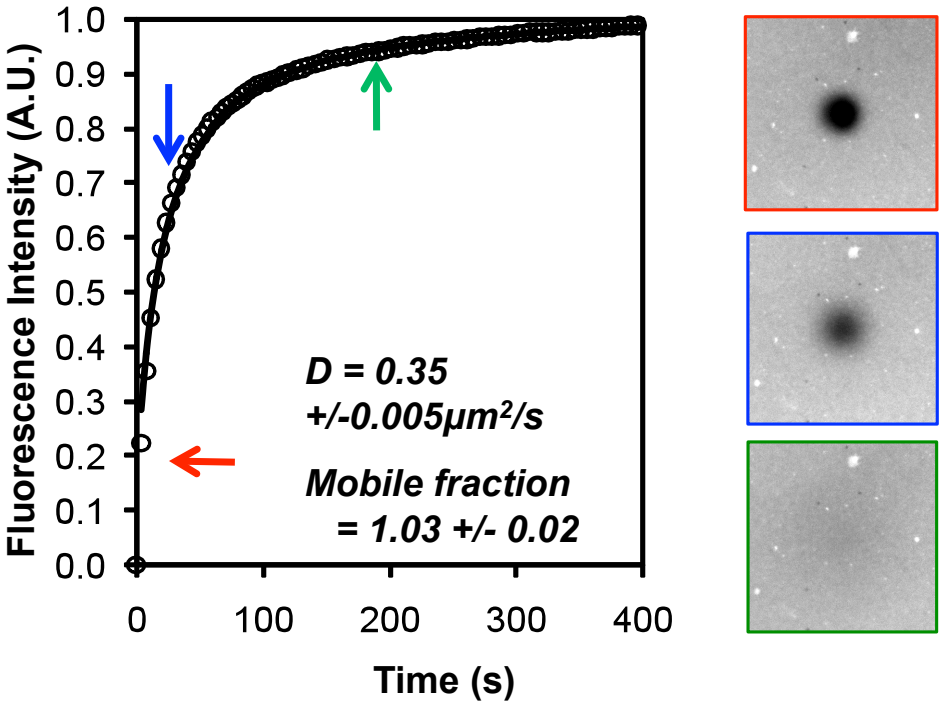

Figure 2 fAPN supported bilayer characterization and mobility. (a) R18 fluorescence recovery after photobleaching in a fAPN supported bilayer (similar to t = 300 s in Fig. 1). The images correspond to the times for each color-coded arrow on the plot. The data are fit to curve (black line) to obtain the diffusion coefficient. At t = 0, the bilayer was bleached with a 561 nm laser beam. The diameter of the bleached area is ~ 20 mm. The reported diffusion coefficient on the plots is averaged from several experiments.

For mobile samples, we obtain two quantitative measurements from these experiments: the mobile fraction and the 2D diffusion coefficient. Samples were prepared on glass surfaces in PDMS wells, as described above. **Figure 2** is a typical fluorescence recovery of R18 in a fAPN-SBs. From this plot, the recovery is nearly restored to 100%, indicating that the mobile fraction of R18 in the fAPN-SB is quite high. The reported diffusion coefficient, averaged over several, similarly-prepared

samples, is 0.35 ± 0.005 $\mu m^2/s$. Mobile fraction and diffusion coefficient values compare well with a control bilayer made of only R18-labeled BHK-liposomes (see *Appendix C* for data, **Fig. C2**).

Note that the recovery curve is smooth and fits well to the 2D diffusion model (black line). Irregular recovery could indicate either disconnected, isolated, bilayer patches that did not heal to form a contiguous film over this length scale, or the presence of lipid microdomain formation. This data indicates that the bilayer has a relatively uniform distribution and is contiguous. Other possibilities for the structure of the bilayer include partial bleb rupture (such as only the outer leaflet fusing to the BHK-liposomes). However, because the diffusion coefficients and mobile fractions in the pure BHK-liposome SLB and fAPN-SB bilayers are comparable, this structure can be ruled out by the following argument. If the blebs were only partially fused, then the R18 trapped in the inner leaflet could not readily exchange with the surrounding lipids after being photobleached. This behavior would manifest as a slower recovery and reduced mobile fraction, relative to the pure BHK-liposome case, over the same timescale of recovery experiment.

Once the bilayer was formed, we verified that the fAPN proteins were incorporated into the supported bilayer and the active, extracellular end was oriented facing the bulk solution (i.e., not inverted towards the glass support) by labeling with a fAPN-specific antibody against the extracellular portion of the protein. Details of these experiments and controls are provided in the *Methods* section (**Fig. S4**) and confirm that fAPN is in the bilayer and oriented properly. Next, we tested APN activity in the blebs and support bilayers using an enzyme activity assay (see *Methods* section). **Fig.**

S5 summarizes the enzyme activity assay, and the results show that APN is enzymatically active in the supported bilayer derived from cell blebs.

Taken together, the antibody binding assay and the enzymatic assay results corroborate that APN protein is functional and maintains its native activity and orientation in the supported bilayer. We note that while the R18 and lipids are mobile in the fAPN-SB (**Fig. 2**), the proteins do not appear to be mobile to the same extent (Fig. S3). Because APN is the binding receptor for the virus, immobility will reduce the strength of binding (avidity) of the virus to the supported bilayer. However, as long as one receptor bond in able to hold the virus in close proximity to the supported bilayer (and within the evanescent field) prior to fusion initiation, we can still track individual virus fusion events using TIRFM, as will be shown in the next section.

We coated microfluidic channels with supported bilayers devoid of, or containing, fAPN. To make the bilayers, either empty-vector blebs or fAPN blebs were used, following the procedure described above for PDMS wells, but modified slightly to be compatible with a microfluidic device. A description of this procedure is in the *Methods* section.

We prepared two suspensions of FCoV virus. The first was treated with the protease, trypsin, (2.5 μg/ml) for 15 minutes at 37^{o}C prior to fluorescence labeling, and the second suspension was left untreated. **Fig. S6** demonstrates, by Western blot analysis, that trypsin treatment of FCoV-1683 virions results in proper cleavage activation of the S protein. This cleavage step is necessary to prime the S protein for the fusion assay that will be carried out following virus binding.

Next, suspensions of fluorescently-labeled, trypsin-treated FCoV were sent through

the channels and incubated for 20 minutes. During this time, virus bound to the fAPN in the supported bilayer, but virus introduced to the channels containing empty-vector-SBs showed no visible binding (**Fig. 3**). Comparing these results emphasizes the requirement that the supported bilayer contain fAPN to localize the virus at the bilayer surface.

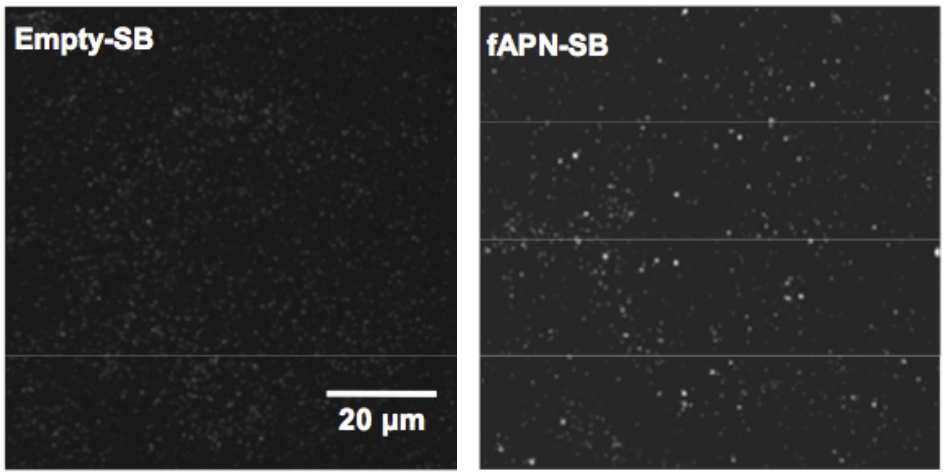

Figure 3 A comparison of FCoV binding to (top) empty vector-SB and (bottom) fAPN-SB. The fAPN-SB exhibits specific binding of the virus. Note that due to the random intercalation of R18 in the viral membranes, fluorescence quenching varies among the virions, so some viruses are dimmer than others in this image.

3.3.3. pH-triggered fusion

To monitor and distinguish the intermediate steps in the fusion pathway from each other in the single particle fusion assay, we use a dual-color labeling scheme **(Fig. 4)**, as described in the *Methods* section. Here, the viral membrane is labeled with a green-emitting, lipophilic fluorophore (R110C18), and the internal contents are labeled with a red-emitting fluorophore (SRB). With this scheme, hemifusion of the outer leaflets is marked by fluorescence dequenching of R110C18 when the outer leaflets mix. Pore

formation is marked by a drop in SRB fluorescence at the fusion site, indicating release of the internal contents. These colors are co-localized in one particle by simultaneous monitoring of both emission wavelengths using TIRFM. In this way, three important time intervals can be obtained for each individual particle: 1) the time for the onset of hemifusion; 2) the lag time between hemifusion and pore formation; and 3) the time when the internal contents are released.

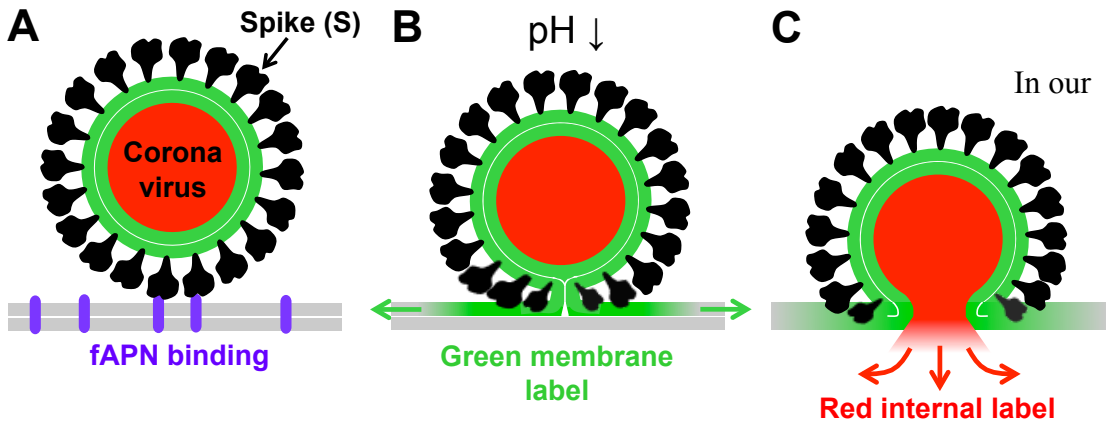

Figure 4 Dual-labeling scheme of coronavirus for single particle fusion experiments that facilitate the capture of intermediate states. The viral membrane is labeled with a green-emitting, lipophilic fluorophore. The viral contents are labeled with a red-emitting fluorophore. The two leaflets of the membranes are distinguished by the thin white line. (top) Spike proteins bind to fAPN (purple) present in the supported bilayer (gray). (middle) A drop in pH triggers hemifusion between the viral membrane and supported bilayer, leading to the mixing of the outer leaflets of each and the formation of a stalk. (bottom) Collapse of the stalk into a fusion pore, which results in the release of viral contents.

assay, membrane fusion between bound trypsin-treated FCoV and supported bilayers is primarily initiated with acidic buffer, although on occasion, some cleaved viruses spontaneously fuse prior to acidification. To test the influence of triggering pH on fusion kinetics, buffer solutions (150 mM NaCl, 1.5 mM MES, 5 mM citric acid) pre-calibrated over a range of acidic pH values (up to pH 7.0) were used. Each solution was sent through a microfluidic channel at a flow rate of 100 μl/min for 2

minutes to acidify the system. The time at which acidification of the flow cell occurred was marked by an obvious decrease in fluorescence of the pH-sensitive fluorophore, Oregon green DHPE, present in the supported bilayers for this purpose. TIRFM images were collected at an interval of 100 ms for three or four minutes. A series of images of a single virion undergoing hemifusion triggered at pH 5.3 is provided in **Fig. 5a**. The dequenching spike is traced in the plot beneath the images. The time at

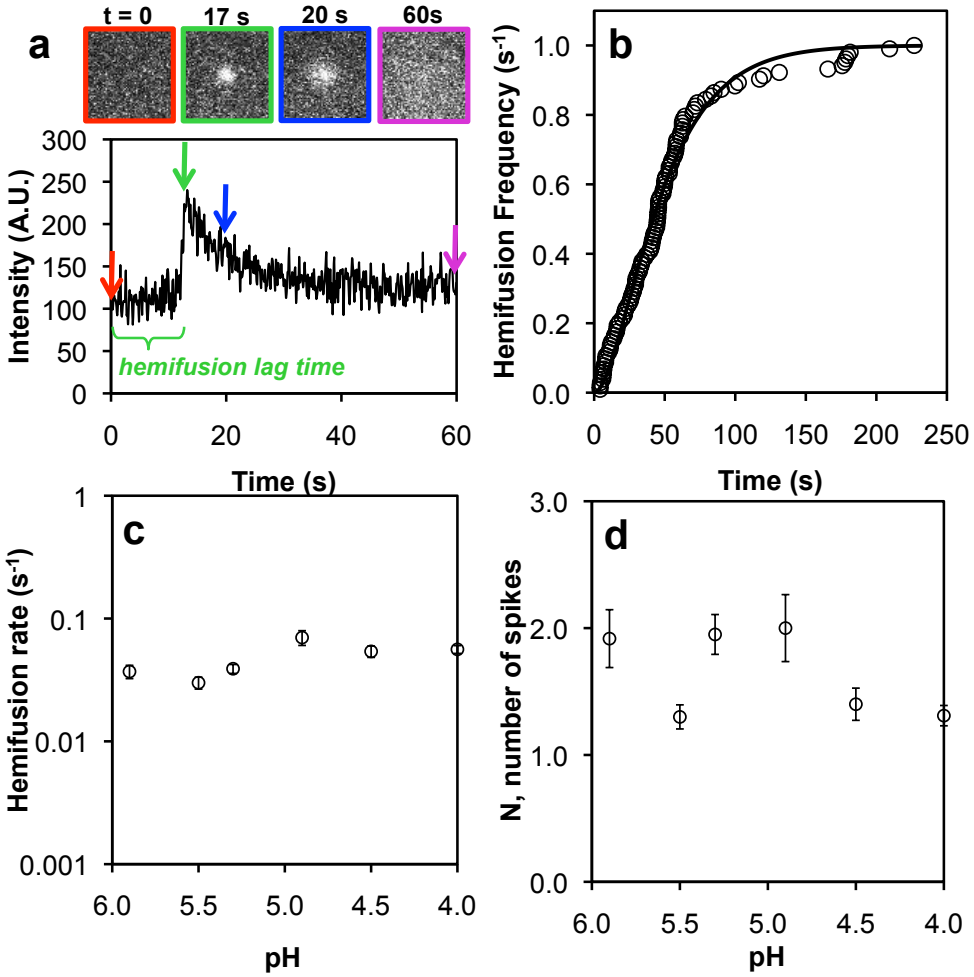

Figure 5 Coronavirus hemifusion kinetics after pretreatment with trypsin. (a) Images of a single coronavirus hemifusion dequenching event. The system was acidified at t = 0 to pH 5.3. The color-coded frames correspond to the time points in the curve marked with arrows. The trace plots the fluorescence in a small 4 x 4 mm region around the virus. The spike in intensity is when the hemifusion event begins. The lag time leading up to this point

is the hemifusion lag time between acidification and hemifusion. (b) Many events like those in (a) are cataloged and plotted as a cumulative distribution function and fit with equation 2 for several pH values. (c) Hemifusion rate constants over a range of pH. (d) The corresponding number of spike proteins, N, determined from the statistical analysis of data.

which the onset of hemifusion occurs (following acidification at t = 0) is declared as the start of the dequenching spike for each individual virus fusion event in the field of view.

A cumulative distribution curve for each triggering pH was generated by plotting the frequency of hemifusion events as a function of the times of the onset of each hemifusion event. For a given triggering pH, a curve (like in **Fig. 5b**) is then fit with a cumulative gamma distribution (equation 1) to estimate the kinetic parameters:

(1)

where k_H is the hemifusion rate constant, t is time, and N is an additional fit parameter, often correlated to the number of steps or the number of fusion proteins that act together to initiate fusion(21).

A gamma distribution is commonly used to fit single particle kinetics of membrane-enveloped viral fusion because individual fusion events occur independently of each other. The gamma distribution describes a multistep reaction scheme, where each step is a stochastic Poisson process with a rate constant k. This model has been used to analyze the kinetics of single particle influenza fusion(21, 22), and because of the similarity between the class I fusion proteins of HA and S, this model is used to analyze coronavirus fusion here. The probability distribution was fit to our data using a non-linear least squares fitting algorithm.

Figure 5c-d summarizes the hemifusion kinetic parameters obtained for trypsin-treated FCoV over a range of triggering pH: 4.0 to 6.0. We note that at pHs above 6.0, the number of fusing particles was too low to obtain statistically significant kinetic parameters. The data presented here (pH 4.0 – 6.0) corresponds to experiments where at least 50 fusion events occurred. What is clear from this data is that FCoV-1683 S cleaved with trypsin requires at least a mildly an acidic environment to fuse, but the rate dependence on pH is negligible. This may indicate that there is a mildly acidic pH threshold at which FCoV-1683 S becomes fusogenically active. As such, we show here that acidic pH may be considered as a subtle trigger for fusion, along with the better characterized triggers of receptor binding and proteolytic processing of S.

A second finding from these experiments is that trypsin can substitute for cathepsins in activating membrane fusion. In the absence of trypsin treatment, the total number of fusion events is less than 10% of the number of events that occur with treatment, post acidification (data not shown).

A third finding is that protease activation can occur before the virus binds the APN receptor, in contrast to the situation with SARS-CoV where the virus must first be bound to the receptor before cleavage. It is interesting to note that FCoV-1683 is one of the coronaviruses that does not need to be cleaved at the S1/S2 junction, and so this result highlights that there may be differences in receptor priming of fusion, depending on how individual coronaviruses are proteolytically activated.

3.3.4. Fusion pore formation

The lag time between the onset of hemifusion and pore formation can be determined from the relative time stamps of the onset of hemifusion dequenching and the onset of the release of fluorophores initially inside the virion. In **Fig. 6**, a series of images of a

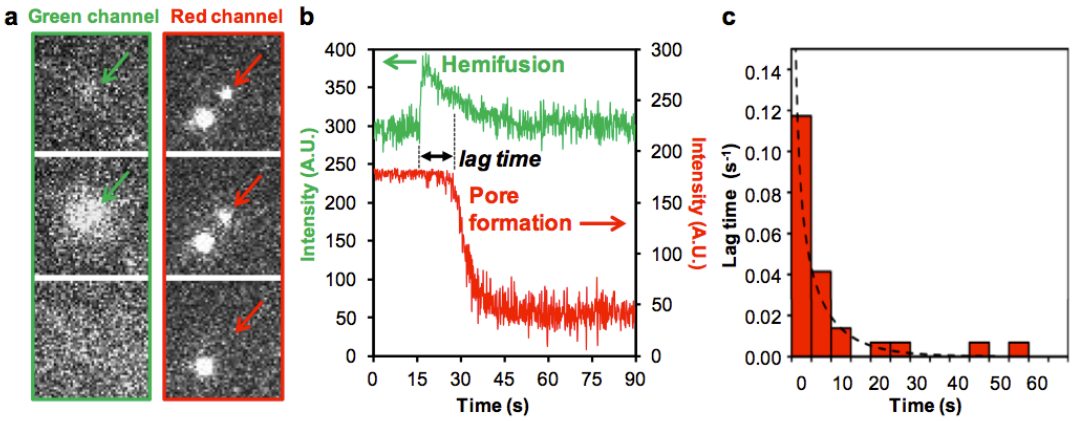

Figure 6 (a) A single, dual-labeled coronavirus fusion event at pH 4.5. Green and red channel images of this virion undergoing hemifusion (green) and then pore formation (red). The arrows denote the virion being analyzed, which has both labels co-localized in one particle. In the red channel, a second particle is visible; however, during this span of time, it does not fuse. (b) The corresponding fluorescence intensity traces of the virion in (a). The lag time between hemifusion and pore formation for this virion is denoted by the black double-ended arrow. (c) Pore formation statistics at pH 4.5 taken from single particle fusion events, like those in (b).

dual-labeled, trypsin-treated FCoV fusing to the supported bilayer is shown in **Fig. 6a**, with the intensity quantified in **Fig. 6b**. The initiating pH in this experiment was 4.5. In **Fig. 6b** it is straightforward to determine the lag time as a difference between the dequenching spike of the green label and the drop in fluorescence of the red label. Lag times for the virions in this sample are cataloged and plotted in the bar graph in **Fig. 6c**. Fitting this histogram with an exponential decay, we determine that the rate constant for the formation of the pore is 0.07 ± 0.01 s^{-1}. Pore formation was also conducted with an initiating pH of 5.0. Here the rate constant for the formation of the

pore is ~0.09 s^{-1}. For both initiating pH's, the transition to pore formation histogram fit best to a one-step process.

These experiments reveal that FCoV exhibits a distinct hemifusion event *before* the release of internal label, which supports that coronavirus, like influenza, proceeds to pore formation via a stalk intermediate. No release of internal red label was observed prior to hemifusion of dual-labeled virions.

3.3.5. Comparison between class I fusion proteins, HA and S

With our results, it is now also possible to compare the fusion kinetics obtained for CoV S with the prototypical protein of this class, influenza HA. In our previous single particle kinetics studies of influenza X-31 HA membrane fusion(22), we found hemifusion and pore formation rate constants at pH 4.5 of $k_H \sim 0.2$ s^{-1} and $k_{pore} \sim 0.08$ s^{-1}, respectively. Here, for FCoV S at the same pH, we obtain $k_H \sim 0.05$ s^{-1} and $k_{pore} \sim 0.07$ s^{-1}, respectively. One main difference we observe between HA and S is the pH-dependence of the hemifusion rate constant. FCoV-1683 S apparently requires an acidic environment to fuse, but the rate dependence on pH is negligible. Influenza, on the other hand, exhibits pH-dependent k_H(21, 22). However, the pore formation kinetics for both viruses are approximately the same. This result is not surprising because the pore formation step is not believed to be pH dependent(54, 58), but controlled to some extent by the physico-chemical properties (e.g., lipid composition, protein content, cholesterol quantity, etc.) of the membranes involved in fusion. Since cell blebs can be made from various cell types, the method presented here for forming

supported bilayers from blebs also provides a new way to interrogate the impact of cell membrane type on viral fusion kinetics.

A second difference between influenza HA and FCoV S is the value of N obtained from the kinetic analysis. N represents the number of steps in a multi-step scheme convoluted into a gamma distribution. In the case of influenza, N has been interpreted as the number of HA proteins that work in parallel to induce hemifusion(21, 22). For influenza, N varies depending on the pH, but within the range of pH 4.0 to 6.0 is ~ 3 using the same experimental acidification conditions employed in these studies. In the case of FCoV S, if this interpretation were used, our data indicates that on average 1-2 S proteins are required to induce hemifusion across the same pH range. For this interpretation, a single S protein appears to have more energy stored within it to induce fusion compared to HA. An alternative interpretation is that N in this case simply means that ~ 1 step is dominating the kinetics, and that step apparently does not vary much with pH. Future experiments are required to shed more light on the mechanism of FCoV fusion and provide a conclusive interpretation of this parameter. Such studies are now ongoing in our laboratory.

3.3.6. Implications of this work

The formation of proteinaceous supported bilayers using the cell blebbing technique opens the possibility for quantitative characterization of membrane fusion kinetics of any enveloped virus that binds to membrane proteins in the host membrane (beyond coronaviruses) and also enables studies of unknown viral receptors in the cell membrane. Because supported bilayers can be made from many cell types(43, 101),

this method can be used to obtain kinetics of virus fusion as it depends on the kind of cell membrane host. In particular, for the many viruses that engage multiple receptors or co-receptors, this method allows the role of individual receptors to be defined in the context of the fusion event. Through biochemical means, proteins can be expressed or suppressed in the plasma cell membrane. Thus, supported bilayers can be tailor-made for fundamental studies of specific host-pathogen interactions that mitigate infection. In addition, by the incorporation of pseudoparticles(97), the method may be expanded to study viruses of high biomedical importance that require enhanced biosafety procedures (BSL-3 and BSL-4).

3.4. Conclusions

In this work, we obtain the membrane fusion kinetics of a less-studied, but clinically important, class I fusion protein: coronavirus S. Overall, the fusion results here recapitulate what is observed *in vivo*, that coronavirus entry requires binding to specific receptors and that membrane fusion is both receptor- and protease-dependent. These results indicate that the *in vitro* method described here is a suitable substitute for studying fusion *in vivo*, but our method of creating and combining proteinaceous bilayers with single particle tracking, now provides a convenient way to obtain quantitative kinetic rate parameters for intermediate steps in the coronavirus fusion pathway, which to our knowledge have not been obtained before. The single particle approach combined with microfluidics offers versatile control over the sequence of triggers of binding, protease exposure, and acidification. Control of the sequence of these triggers is important, as the order may define the fusion pathway, tissue tropism, and pathogenicity of coronaviruses. Systematically varying these complex triggers

using this platform provides a new way to study this virus's ability to rapidly adapt to other hosts. Versatile platforms are of critical importance to providing data that can be leveraged to limit the infection of the human population, especially in light of the recently-emerging strain of MERS-CoV.

Acknowledgements

We thank David Holowka and Barbara Baird for training D.A.C. on the blebbing technique and for useful discussions. We thank the National Science Foundation (Grant CBET-1149452) for supporting some of this work. Some experiments were performed at the Nanobiotechnology Center and Cornell NanoScale Facility, a member of the National Nanotechnology Infrastructure Network, which is supported by the National Science Foundation (Grant ECS-0335765). Work in the Whittaker lab is supported by grants from the Cornell Feline Health Center, the Winn Feline Health Foundation, and the Morris Animal Foundation.

CHAPTER 4

MEMBRANE FUSION-COMPETENT VIRUS-LIKE PROTEOLIPOSOMES AND PROTEINACEOUS SUPPORTED BILAYERS MADE DIRECTLY FROM CELL PLASMA MEMBRANES

4.1 Introduction

Mammalian cell membranes are composed of a mixture of phospholipids, cholesterol and proteins. Membranes are coated with a carbohydrate layer composed of glycosylated proteins and glycolipids that are collectively referred to as the glycocalyx. The properties of the glycocalyx dictate host-pathogen interactions, and these interactions play a key role in the pathogenesis of infectious viruses such as influenza.

Influenza is a membrane-enveloped virus that causes seasonal outbreaks and occasionally pandemic illnesses in humans. Outbreaks occur because continuous viral evolution produces mutants capable of optimal interactions with the glycocalyx of target cells while also being able to successfully evade the immune system.

Continuous viral evolution, therefore, requires scientists to be vigilant in determining both the host and viral factors that facilitate infection. Researchers must have tools available to quickly and safely assess virus-host interactions to: 1) monitor virus evolution necessary for future vaccine development, 2) screen new antiviral drugs, and 3) study fundamental membrane fusion processes.

A relatively new approach for quantitatively studying virus-cell interactions and viral entry kinetics is single particle imaging using total internal reflection fluorescence microscopy (TIRFM) (64). A key ingredient in this platform is a supported lipid bilayer (SLB) that coats the walls of microfluidic channels and acts as a host membrane mimic (78, 117). This biomimetic material preserves lipid mobility in the bilayer plane and the planar geometry removes many experimental complications imposed by live cells. These features facilitate the study of virus-cell interactions and the membrane fusion processes required for viral infection, but in a convenient platform for imaging and quantitative data collection. These platforms have provided useful information about seasonal influenza (21, 22, 96), Sindbis (20), and other low pathogenic viruses. However, to study fusion processes of highly pathogenic membrane-enveloped viruses, like pandemic strains of influenza, Ebola virus, or Severe Acute Respiratory Syndrome (SARS) coronavirus, one must have laboratory biosaftey level of 3 or more. Fewer facilities have this classification, which effectively limits the number of researchers that study these pathogens.

One strategy to safely study highly pathogenic viruses uses pseudovirus particles. One of the most common constructs for pseudovirus particles is the Vesicular Stomatitis Virus (VSV) (118, 119). In the VSV pseudoparticle approach, a cell is

transfected with a viral fusion protein of interest so that this protein is expressed at the cell surface. The transfected cell is then infected with a modified, laboratory strain of VSV (designated VSVΔG*-G) that has the gene for the fusion protein (G) deleted. The infected cells replicate the VSV following its usual infection pathway via endocytosis: endosomal escape, genome replication in the nucleus, viral protein production, and repackaging at the membrane surface. At the conclusion of this process, nascent viral particles bud from the cell plasma membrane surface. During the budding process, the emerging virions membrane acquires the fusion protein that was expressed in the plasma cell membrane of the infected cell. It is important to note that the pseudovirus does not contain the gene for the fusion protein of either VSV-G or the fusion protein coded in the plasmid that was used to transfect the cells prior to its infection with the VSVΔG*-G strain. Thus, the emerging pseudovirus cannot propagate further infection, making it a safe strategy to study the activity of fusion proteins of virulent viruses.

Combining these virus-like particles with analytical techniques that can quantitatively assess virus-host interactions, such as single particle imaging, gives researchers powerful tools to study viral entry. However, the production of the pseudovirus particles is complex, requiring trained technicians and several days of culture, growth, and infection, which limits its wider use beyond research laboratories. Our goal was to create a simpler method to produce virus-like proteoliposome particles that can be used for fundamental virus entry studies, as probes to assess virus-host interactions, or as packages for therapeutics where the viral fusion machinery ensures the delivery of cargo to cytosol of a target cell.

Herein we describe a simple method to create virus-like proteoliposomes from cell plasma membranes that express a viral membrane protein of interest using a cell blebbing technique. Cell blebs are chemically-induced membrane vesicles that bud from the cell plasma membrane. These chemically-induced vesicles were first generated in the 1970s(101, 120). Since then, blebs have been used to make giant plasma membrane vesicles (GPMV) to study lipid raft and domain formation (44, 45), to test membrane permeability for drug delivery applications (121, 122), and to elucidate membrane protein behavior (43), but not as a means to produce virus-like particles, to our knowledge. We show here that influenza virus-like proteoliposomes (VLPs) produced from cell blebs contain fusion proteins that maintain full fusion functionality, like native virions. Membrane fusion of these VLPs is assessed using single particle imaging and demonstrates their utility as non-infectious virus surrogates for studies of pathogen-host interactions and virus fusion mechanisms. We also found that we can also use cell bleb proteoliposomes to create virus-like supported bilayers (VLSB) that contain viral fusion proteins. These VLSBs are also capable of carrying out membrane fusion with lipid vesicles containing the viral receptor.

In this paper, we create cell blebs from baby hamster kidney (BHK) cells, transfected with the transmembrane influenza fusion protein, hemagglutinin (HA). Pure blebs have difficulty self-assembling into supported bilayers presumably because of high protein and cholesterol content. Our strategy for inducing the SLB formation of the cell blebs is adapted from Dodd et al (123), where liposomes are added to blebs adsorbed onto a glass substrate. The rupturing of the liposomes in spaces in-between

the adsorbed blebs induces bleb rupture. To closely mimic the native BHK cell membrane, we use a liposome composition to match that reported by Sobo et al (107) for BHK endosomes.

One key advantage of making supported bilayers using cell bleb proteoliposomes, compared to traditional methods to produce proteoliposomes (124), is that proteins can be incorporated directly into supported bilayers without the requirement of detergent membrane solubilization, protein purification steps, and reconstitution into liposomes. These steps can result in loss of native conformation of the membrane protein and disruption of the local lipid-protein interactions that may be necessary for regulating protein activity (125). Thus, a virus-like supported bilayer produced from cell blebs with fully-functional proteins, combined with a microfluidic platform, could facilitate high throughput screening of antiviral drugs and host cell-pathogen interactions.

4.2 Materials and Methods

4.2.1. Cells and plasmids

Baby hamster kidney-21 (BHK-21) cells, a generous gift from Michael Whitt, were grown and maintained in Dulbecco's modified Eagle medium (DMEM, CellGro) supplemented with 10% fetal bovine serum (Gibco), 100 U/ml penicillin and 10 μg/ml streptomycin (CellGro), 1% HEPES buffer (CellGro) in a 37°C, 5% CO_2 incubator.

The following plasmids were used: pCAGGS-H3/X31, encoding the influenza hemagglutinin HA X-31, a generous gift from David Steinhauer. The pCAGGS vector was used as an empty vector control.

4.2.2. Preparation of cell blebs

For transfections, 1.5×10^6 cells were seeded in 10-cm culture dishes, and incubated for 24 hours. Transfections were performed using TurboFect transfection reagent (ThermoScientific) according to manufacturer's instructions and using 12 μg of plasmid DNA for each plate. Buffer used in cell culture will be referred to as buffer A (2 mM $CaCl_2$, 10 mM HEPES, 150 mM NaCl at pH 7.4) and to induce cell blebbing, as buffer B (2 mM $CaCl_2$, 10 mM HEPES, 25 mM formaldehyde, 2 mM dithiotreitol (DTT) and 150 mM NaCl at pH 7.4). Cell blebs were dialyzed using cellulose dialysis tubing (Fischer Scientific) in two 100 ml volumes of buffer A for 24 hours to remove the blebbing buffer. The size distribution of cell blebs was determined by dynamic light scattering using a Malvern Zetasizer Nano (Worcestershire, UK). A plot of the size distributions is provided in the Appendix A.

4.2.3. Preparation of liposomes

The following lipids were used in the experiments: 1-oleoyl-2-palmitoyl-*sn*-glycero-3-phosphocholine (POPC), 1-oleoyl-2-palmitoyl-sn-glycero-3-phosphoethanolamine (POPE), 1,2-dioleoyl-sn-glycero-3-phosphocholine (DOPC), cholesterol, sphingomyelin and total ganglioside extract. These materials were all purchased from Avanti Polar Lipids (Alabaster, AL). Fluorescent lipids and lipophilic labels used to label membranes include, Oregon green DHPE and Octadecyl

Rhodamine (R18), all purchased from Molecular Probes, Eugene, OR. The water-soluble fluorophore, Sulforhodamine B (SRB), was purchased from Molecular Probes, and used to label interiors of liposomes and virus.

Two formulations of liposomes were used in these studies. The first preparation, referred to as BHK-liposome, contained POPC, POPE, sphingomyelin and cholesterol in the ratio 37.3:34.2:5.7:22.8. This composition was formulated to match the native lipid content of BHK cells as closely as possible (107) and primarily used in the formation of bleb supported bilayers. The second preparation, referred to as SA-liposome (SA = sialic acid), was composed of DOPC, POPC, cholesterol and total ganglioside extract (which contain sialic acid) in the ratio 4:4:2:0.5. SA-liposomes were used both to form supported lipid bilayers containing SA and as liposomes to verify HA functionality in cell bleb-derived HA-supported bilayers. Standard procedures were used to form the liposome solutions (117). Our detailed procedure is described in the Appendix A.

4.2.4. Formation of supported lipid bilayers from pure liposome solutions

Liposome solutions were added to either a polydimethylsiloxane (PDMS) well or drawn into a microfluidic device and incubated for at least 5 minutes before rinsing with buffer A. fabrication procedures for PDMS wells and microfluidic devices is provided in the Appendix A. Supported lipid bilayers self-assemble on clean glass during vesicle fusion (78-80) of these liposome formulations. In some experiments, liposome membranes were fluorescently-labeled with Oregon green DHPE or with R18 prior to bilayer formation. Fluorescent labels enabled visualization of the supported lipid bilayer; were indicators of bilayer acidification in fusion experiments;

and were probes for mobility measurements.

4.2.5. Fluorescent labeling of blebs, liposomes, or native virus

Influenza X-31 (H3N2) with a hemagglutinin (HA) concentration of 2 mg/ml (as determined by Charles River Labs) was used in virus membrane fusion experiments. To visualize membrane fusion using a fluorescence dequenching technique, membranes must be labeled with a semi-quenched amount of fluorophores following standard procedures(50) (73, 80). In these experiments, HA-bleb membranes, SA-liposome membranes, and virus membranes of influenza X-31 virus were labeled with R18 according to the general procedure outlined in the Appendix A.

4.2.6. Antibody binding experiments

To label HA proteins in cell bleb-derived support bilayers, the bilayer was incubated with Alexa Fluor 488-conjugated mouse monoclonal IgG_1 anti-hemagglutinin antibody (16B12) (Invitrogen) at a concentration of 1 μg/ml for 20 minutes. Following incubation, bilayers were rinsed extensively with buffer A to remove unbound antibodies and visualized using an inverted fluorescence microscope with appropriate filter set.

4.2.7. Single particle membrane fusion to supported bilayers: TIRF microscope configuration

Membrane fusion assays were conducted using total internal reflection fluorescence (TIRF) microscopy using an inverted Zeiss Axio Observer.Z1 with a α Plan-Apochromat 100x oil objective with a numerical aperture (NA) of 1.46. Index-

matching liquid (Carl Zeiss, Inc.) was used to couple the glass coverslip of the microfluidic device to the objective. In this setup, two lasers can be used simultaneously to excite different color fluorophores; we used 561 nm and 488 nm excitation wavelengths from solid-state lasers. These were coupled into the optical pathway of the microscope using a Laser TIRF 3 slider (Carl Zeiss, Inc.), which controlled the angles of incidence. Exceeding the critical angle for water-glass system (~ 62°) ensured total internal reflection of the lasers and created evanescent waves about 100 nm thick. At this thickness, the evanescent waves excited fluorophores positioned within the supported bilayer, within fluorescently-labeled liposomes bound to hemagglutinin proteins embedded in the supported bilayer, or within fluorescently-labeled virions bound to SA-containing lipid bilayers. The excitation laser light was band-pass filtered through a Semrock 74 HE GFP/mRFP filter cube, and then combined with a dichroic mirror before being focused on the outer edge of the back aperture of the objective. The fluorescence emission signal was filtered through a 525/31 and 616/57 nm dual band-pass emission filter and then sent to an electron multiplying CCD camera (Hamamatsu ImageEM C9100-13, Bridgewater, NJ).

4.2.8. pH-triggered membrane fusion assay

Membrane fusion between bound virions (or liposomes) and supported bilayers was initiated by flowing buffer (150 mM NaCl, 1.5 mM MES, 5 mM citric acid) pre-calibrated to the optimal acidic triggering pH for X-31, pH = 4.5 (27). This acidic buffer was sent into the microfluidic device at a flow rate of 100 μl/min for 2 minutes. The time at which acidification of the flow cell occurred was marked by an obvious decrease in fluorescence of the pH-sensitive fluorophore, Oregon green DHPE,

present in the supported bilayer for this purpose. TIRFM was used to monitor fusion and images were collected at an interval of 100 ms for 3 to 4 minutes.

4.2.9. Image processing

The images acquired during the membrane fusion assays were analyzed using both ImageJ (NIH) and MATLAB (Mathworks). Fusing particles were manually selected in ImageJ and the fluorescence intensity in a 4x4 pixel region around each particle was collected as a function of time. In videos where background noise was high due to a large amount of fusion events, a rolling ball background subtraction algorithm was applied to all of the images to remove excess background noise as the fluorophores diffused into the membrane after hemifusion. The rolling ball algorithm determines the local background for every pixel by averaging over a large circular region around the pixel. This background value is then subtracted from the original image. The fluorescence trajectories for the particles were then imported to MATLAB (Mathworks) for further analysis. A code written in MATLAB determined the onset time of the dequenching 'spike' for each particle by finding the time of the maximum intensity in each particle trajectory.

4.3. Results and discussion

4.3.1. Formation of cell blebs and size characterization

Cell blebs are produced from baby hamster kidney (BHK) cells, transfected with the transmembrane influenza fusion protein hemagglutinin (HA). Twenty-four hours

after transfection of BHK cells with the desired plasmid, cells were washed twice with buffer A. 3 ml of buffer B, which contains the chemical that induce the formation of bleb vesicles from the cell plasma membrane, was added to each culture dish. The dishes were then incubated for 1 hr at 37ºC with gentle rocking. After incubation, the cell supernatant, containing detached cell blebs, was decanted into a 15 ml falcon tube and placed on ice for 20 minutes to allow any detached cells to settle out. The supernatant was then transferred to new test tube. Buffer B was removed from the supernatant by dialysis with buffer A for 24 hours. An excellent recent review of protocols for cell bleb production is given in Sezgin et al (43).

The size and distribution of cell blebs in the supernatant was determined by dynamic light scattering. The bleb supernatant showed three populations typically, with three main peaks at 40 nm, 100 nm, and 600 nm. A plot of the size distribution is provided in the Appendix A (Fig. S1). The size of BHK-liposomes and SA-liposomes were relatively monodisperse with diameters ranging between 90 – 100 nm. Aliquots of these solutions were used to carry out single particle membrane fusion experiments, as will be described later.

4.3.2. Formation of proteinaceous supported bilayers from cell blebs

To visualize the formation of supported bilayers derived from BHK cell blebs, the membranes of HA-blebs were first labeled with a lipophilic fluorophore, R18. A small aliquot of the labeled bleb solution was added to a PDMS well and incubated for 10 minutes at room temperature. During this time, blebs contact and adsorb to the glass surface. Excess blebs that were not adsorbed to the glass surface were removed by gently rinsing the well with buffer A. Observation of samples under 40x and 100x

magnification show that the blebs are not ruptured at this stage, but are adsorbed to the glass surface intact, as seen in Fig. 1(A) as punctuate bright spots. Although the absolute concentration of the bleb solution is unknown, the solution was observed to be sufficiently concentrated to absorb blebs over the entire glass surface.

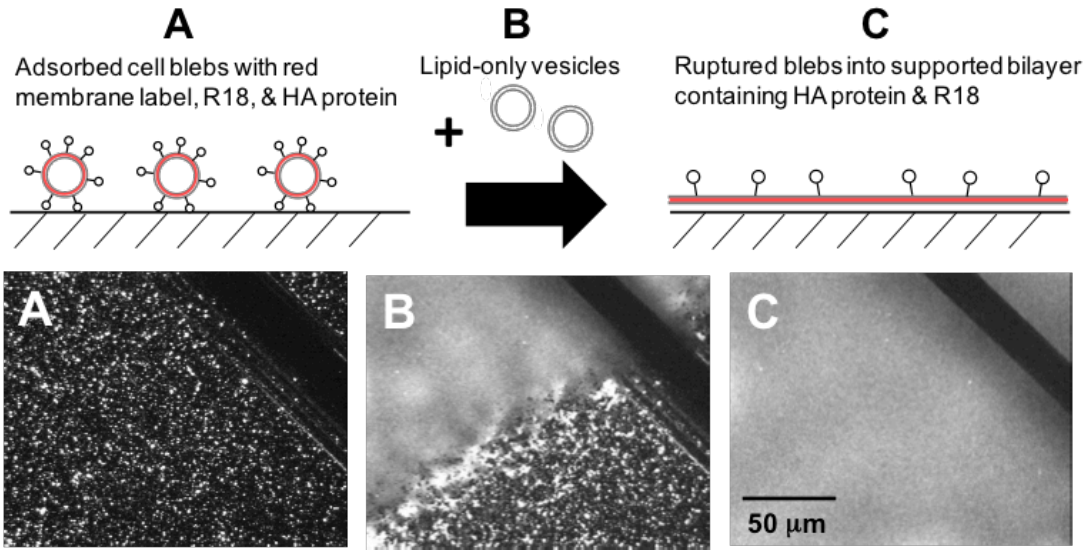

Fig. 1. Formation of HA-bleb VLSB containing hemagglutinin from influenza X-31. (A) Intact HA-blebs containing R18 adsorbed to glass substrate. (B) 15 seconds after the addition of BHK-liposome solution to (A). Note that the BHK-liposome solution is devoid of fluorescent label. (C) Continuous supported bilayer observed 2 minutes after the addition of BHK-liposomes. The images are all taken under 40x magnification. The dark line in the right corner of the images is a scratch intentionally made with a dissection tool to aid in finding the focal plane of the bilayer. The continuous focus of this line throughout the rupture process indicates that the focal plane does not change during this series of experiments and that the uniform distribution of fluorescence in (C) is due to mobility of fluorophores redistributed throughout the newly-formed planar bilayer.

To induce the formation of a supported bilayer from the adsorbed blebs, we adapted a procedure Dodd et al (123) used to form supported bilayers from the inner membrane vesicles of *E. coli*. In our case there are two distinct procedural differences from Dodd et al. First, the liposomes used to rupture the BHK cell blebs were formulated to closely match the BHK endosomal composition (107) (referred to as BHK-liposome) so that the resulting bilayer would most closely resemble the native cell membrane lipid content. Second, we adsorb cell blebs to the substrate *first*, rather than mix in solution with BHK-liposomes prior to adding to the well. This latter step ensures that the liposomes do not outcompete the cell blebs for glass adsorption.

In this experiment, the BHK-liposomes do not contain any fluorophore labels. The rupturing of the liposomes in the spaces in-between the adsorbed blebs rapidly induced the rupture of the blebs, as indicated by the dispersion of the bright, punctuate spots (Fig. 1B - C). This observed dispersion in fluorescence is due to the spread of R18 that originated in the membranes of the adsorbed blebs, diffusing within the newly-formed bilayer plane after rupture. Photobleaching a small section of this newly-formed bilayer and monitoring the temporal recovery also confirms that the blebs have ruptured to form a planar film. Photobleaching experiments are used to determine diffusion coefficients in the supported bilayers and will be described in a later section.

The newly-formed supported bilayer was monitored for 12 hours after formation. During this time it remained visually stable and uniform (e.g., no domain formation was observed or growth of defects).

4.3.3. Supported bilayer quality, planarity, and thickness characterization

AFM and ellipsometry were used to confirm the formation of supported bilayers from cell blebs, visually assess their uniformity, and to characterize the film thicknesses. Three different samples were characterized by each method: A) a supported lipid bilayer formed from protein-free, BHK-liposome solution only, B) a supported bilayer formed from HA-blebs+BHK-liposomes (VLSB), and C) non-ruptured, adsorbed HA-blebs (VLPs) on glass, prior to BHK-liposome addition.

4.3.3.1 AFM

Samples for AFM were prepared in PDMS wells as described in the *Methods* section. Details of the AFM setup and images (Fig. S2) are provided in the Appendix A. Contact mode under water was used to image and measure the thickness/height of the bilayer. For a point of comparison, we first characterized a standard bilayer made from BHK-liposome solution only (Sample A). Typical supported bilayers formed by vesicle fusion to glass are ~ 4 nm thick and have about a 1 nm water layer between the bottom leaflet and glass support. An AFM image in Fig. 2SA in the Appendix A shows that the BHK-liposome bilayer is a relatively uniform film of thickness ~ 4 - 6 nm, as determined by scanning across the depth of a thin line intentionally scratched on the bilayer. This thickness is in good agreement with literature values for similar supported lipid bilayers (126-128).

In the next experiment, we imaged the VLSB (Sample B). From the AFM image (Fig. 2SB, Appendix A) we see in general that the bilayer is uniform, but there are some defects present in the film. The thickness of the VLSB was determined by measuring the depth of a defect. The measured depths of several defects were

consistently between 3 and 4 nm, which are consistent with the thickness measured for the standard BHK-liposome bilayer. However, to be sure we were not measuring thicknesses based on areas primarily consisting of BHK-liposome bilayer; we also measured film thicknesses of these samples over and extended area (0.5 cm x 0.5 cm) using ellipsometry.

We also attempted to image adsorbed cell blebs prior to supported bilayer formation (Sample C), but found that images were very irregular and difficult to interpret as is consistent with irregularly adsorbed material and incomplete film formation.

4.3.3.2. Ellipsometry

To corroborate that the addition of lipid vesicles to adsorbed cell blebs induced the formation of a supported bilayer film, ellipsometry was also performed on the same three kinds of samples used in AFM imaging. For these measurements, it was necessary to prepare samples on silicon wafers instead of glass coverslips, but the procedure was otherwise the same as described in the *Methods* section. Additional experimental details are provided in the Supplementary Information Appendix A. The thickness of the oxide layer of the silicon wafer used for these experiments was determined to be approximately 4.1 nm. This value was into account when modeling the supported lipid bilayer data to determine the film thickness, as described in the Appendix A. A water layer of ~ 1 nm exists between the oxide support and a supported lipid bilayer film typically. We did not determine the thickness of protein layer protruding from the supported cell-bleb bilayer. The total amount of expressed HA protein is not dense enough to create a contiguous film, as inferred by results of

antibody binding experiments presented in the next section.

The film thicknesses are summarized in Table S1 in the Appendix A and match reasonably well to the thicknesses measured using AFM. No film thickness could be determined from the sample of adsorbed cell blebs prior to BHK-liposome addition, presumably because of the irregularity of the adsorbed bleb surface density.

4.3.4. Antibody binding to confirm presence of proteins derived from cell blebs in the supported bilayer

To confirm that the hemagglutinin proteins expressed in the cells used to produce blebs were both incorporated into the supported bilayer and oriented facing the bulk (i.e., not inverted towards the glass support), the bilayer was incubated with anti-HA antibodies specific for X-31 HA protein. Anti-HA labeled with Alexa Fluor 488 conjugate was incubated with HA-bleb supported bilayers for 20 minutes. The bilayer was then rinsed extensively with buffer A to remove unbound antibodies. Control experiments were performed where the anti-HA antibodies were incubated for 20 minutes on an HA-free bilayer (derived from empty vector blebs). Binding was assessed by imaging samples with an inverted fluorescence microscope. The images for the antibody binding experiments are provided in the Appendix A (Fig. S3) and show that a significant amount of specific anti-HA binding occurs on the VLSB, while minimal non-specific binding occurs for the HA-free bilayer. This specific binding not only indicates that HA was present in the bilayer, but also that a significant amount of protein was in the correct orientation facing the bulk solution, and not towards the glass support.

4.3.5. Mobility in supported bilayers

4.3.5.1. Lipid mobility

Fluorescence recovery after photobleaching (FRAP) was employed to determine the fluidity of the cell bleb bilayers. Details for the experiment and data analysis are provided in the Appendix A. Samples were prepared on glass surfaces as described in the *Methods* section. Fig. 2(A-C) shows the typical bleaching and recovery of R18 probes in various supported bilayers after bleaching with a 561 nm circular laser beam. Sample A is the BHK-liposome supported lipid bilayer, sample B is a glass surface coated with adsorbed VLPs (HA-blebs) prior to BHK-liposome solution addition, and sample C is a VLSB derived from HA-blebs after BHK-liposome addition. The diffusion coefficients of R18 in samples A and C were found to be around 0.25 $\mu m/s^2$ with mobile fractions near 1. For the samples containing only absorbed cell blebs (sample B), photobleached spots did not recover, as expected if lipids and R18 fluorophores were confined to the adsorbed proteoliposomes and unable to exchange with surrounding unbleached adsorbed blebs.

To determine if the binding of an anti-HA antibody to HA in the VLSB reduces the mobility of R18 in the supported bilayer, the mobility of R18 was tested before and after antibody binding. It was found that antibody binding did not hinder the diffusion of R18 or cause the bilayer to lose mobility (Fig. 2D). This result indicates that the VLSB is not near a phase transition (129) and should remain in the fluid state after receptor binding. This is a key point as binding-induced phase transition could impact the ability of membrane fusion to occur, or at minimum, slow down the membrane fusion kinetics

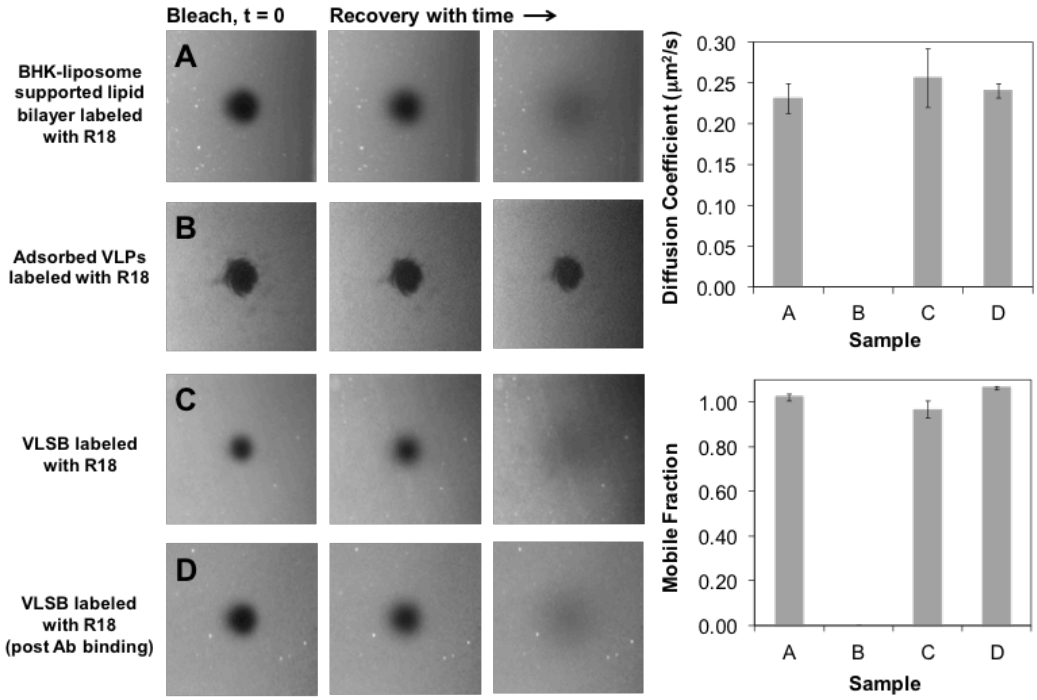

Fig. 2. Fluorescence images of intensity recovery with time after photobleaching. Data from these images if used to determine diffusion coefficients and mobile fractions in various supported bilayers. (A) R18 in BHK-liposome supported lipid bilayer: protein-free, control case. (B) Adsorbed R18-labeled VLPs. (C) R18-labeled VLSB. (D) R18-labeled VLSB after anti-HA antibody binding. The top bar graph summarizes the diffusion coefficients for each sample. The bottom bar graph summarizes the mobile fraction for each sample.

4.3.5.2. Protein mobility

The mobility of HA protein in the supported bilayers was assessed by two methods. First, the position of bound, fluorescently-labeled antibodies to HA were tracked at 100x magnification for an extended period of time. Second, fluorescence recovery after photobleaching was monitored as described for the lipid diffusion measurements. In both methods, limited protein mobility was observed.

There are two possibilities to explain immobilization of the protein. First, the thin water layer beneath the supported bilayer is may not be thick enough to keep the

extended portions of the HA from coming into contact with the underlying support and non-specifically adsorb to it. Second, because the fluorescent antibody used to label the HA can bind multiple proteins, it is possible that cross-linking due to antibody binding can cause a reduction in mobility as well.

There are a number of cushioning strategies that can be used to improve protein mobility, from tethered polymer layers (130-132) to dextran cushions (133, 134). None of these cushioning strategies were integrated here because, as we will describe next, protein immobility did not seem to block hemagglutinin's ability to bind sialic acid or carry out its function of inducing the fusion of membranes. We elected not to use cushions to keep the system simple for this study.

4.3.6. Membrane fusion functionality of HA protein in cell blebs and in bleb-derived supported bilayers

The function of hemagglutinin (HA) in influenza entry virus is to mediate the fusion between viral and host endosomal membranes. HA protein undergoes a conformational change at pH values less than 5.5 to trigger the fusion of the viral and endosomal membrane during virus infection (48). Antibody binding experiments verified that HA was present in the supported bilayer in the correct orientation. However, the blebbing buffer, which contains a small amount of DTT and formaldehyde, can induce the cleavage of disulphide bonds and the cross-linking of HA proteins before dialysis takes place to remove these chemicals from the blebs. Thus, the fusion function of the proteins must be tested to ensure the blebbing buffer did not destroy the function of the protein. To test the functionality of HA proteins expressed in cell blebs and in bleb-derived bilayers, we performed the following series

of experiments.

4.3.6.1. Membrane hemifusion

Membrane hemifusion is the merging of the two outer-most leaflets of the viral and host membranes. At this stage, the complete fusion pore has not opened, but a stalk-like structure connects the viral and host membrane. When this stalk forms, fluorescent labels can mix with lipids from the host cell and radially diffuse away from the hemifusion site. By labeling one membrane with a quenched amount of fluorophore, and the other membrane with nothing, hemifusion can be marked by a "dequenching" event when the stalk is formed (5, 50). These dequenching events are easy to observe using TIRFM at the individual virion level.

In the first experiment, we tested the ability of HA expressed in cell blebs (VLPs) to hemifuse to sialic acid-containing supported lipid bilayers. SA-liposomes were drawn into a microfluidic device at a flow rate of 100 μL /min for 1 minute and incubated in the channel for 20 minutes. The channel was rinsed with buffer A at 100 μL /min for 2 minutes to form a supported lipid bilayer containing sialic acid receptor. HA-blebs labeled with R18 were drawn into the channel at a flow rate of 30 μL/min for 5 minutes and bound to SA in the supported bilayer during 20 minute incubation. Unbound HA-blebs were removed from the channel by rinsing with buffer A at 100 μL/min for 2 minutes. HA-mediated fusion of the blebs to the supported lipid bilayer was initiated by flowing pH 4.5 buffer into the channel at 100 μL/min for 2 minutes. Hemifusion was marked by dequenching of the R18 that originated in the HA-bleb,

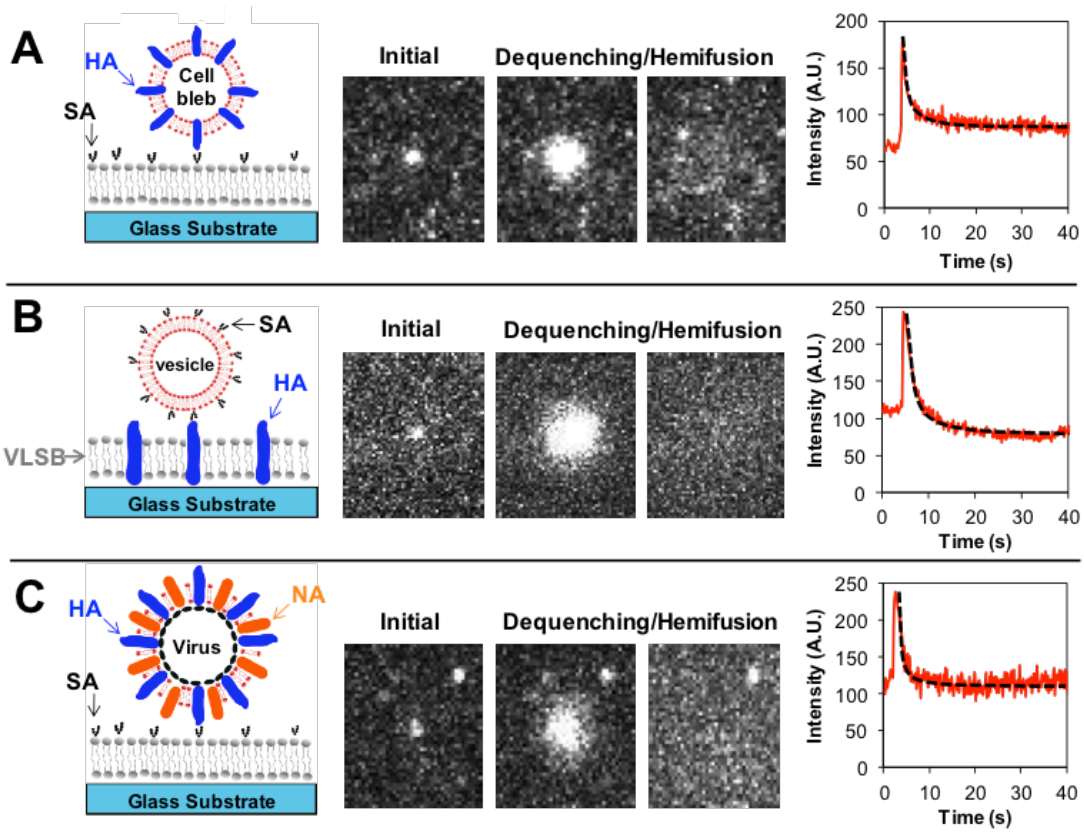

Fig. 3. Single particle hemifusion and lipid mixing experiments compare HA fusion functionality in the HA-bleb VLP, the HA-VLSB, and in a native influenza virus. HA = hemagglutinin; NA = neuraminidase; SA = sialic acid. (A) VLP labeled with R18 fusing to sialic acid-containing supported lipid bilayer. (B) Sialic acid-containing vesicle labeled with R18 fusing to VLSB. (C) Influenza X-31 virion labeled with R18 fusing to sialic acid-containing supported lipid bilayer. The plots to the right trace the fluorescence intensity around each particle and show the dequenching event and the 2D diffusion of the R18 fluorophores away from the fusion site until background levels are reached. The black dashed lines are fits to equation 2 of the decay portion of the curve to obtain diffusion coefficients, as described in the text.

and its subsequent radial diffusion among the lipids in the supported SA-bilayer (Fig. 3A).

In a second set of experiments, we tested the functionality of HA in supported bilayers derived from HA-blebs. HA-VLSB were formed at neutral pH in microfluidic

channels, following the general procedure outlined above. First, HA-bleb solution was drawn into the microchannel at a flow rate of 30 μl/min for 1 minute and incubated for 20 minutes to allow the blebs to adsorb to the channel walls. The channel was subsequently rinsed with buffer A at 100 μl/min for 2 minutes to remove excess blebs. Second, BHK-liposome solution was drawn into the microchannel at 100 μl/min for 2 minutes and incubated to induce the rupture of adsorbed blebs. After 10 minutes elapsed, more BHK-liposome solution was drawn into the channel at 10 μl/min for 5 minutes to heal defects in the membrane. Third, the channel was rinsed with buffer A at 100 μl/min for 2 minutes to rinse out the excess liposomes. Following the formation of the VLSB, SA-liposomes labeled with R18 were then added to the channel and incubated for 20 minutes. During this time, the SA-liposomes bound to the HA proteins in the supported bilayer. Excess vesicles were rinsed from the channel. To activate the HA protein to induce hemifusion, buffer A at pH 4.5 was drawn into the channel. Hemifusion of the SA-liposome to the VLSB was indicated by R18 dequenching and radial diffusion through the bleb membrane away from the point of fusion (Fig. 3B).

The third experiment was a control case of an R18-labeled X-31 influenza virion fusing to SA-containing supported lipid bilayer. The SA-bilayer was formed as described above in the first experiment of this series, and fusion initiated in the same manner. The hemifusion results for this control case are presented in Fig. 3C. A qualitative comparison of the HA-bleb VLP and HA-VLSB results to the native virion shows that hemifusion proceeds without much variation among these geometries.

For a more quantitative comparison among the hemifusion events, the fluorescence

intensity curves plotted to the right of Fig. 3 can be fit with a two-dimensional diffusion equation to determine the diffusion coefficient of the R18 fluorophores as they move radially away from the fusion site. The equation used to fit the decay in the fluorescence intensity data is:

$$I(t) = I(0)\left[1 - \exp\left(\frac{-r^2}{4Dt}\right)\right] \quad (1)$$

where *I(t)* is the intensity at time, *t*; *I(0)* is the intensity value at maximum dequenching (the peak intensity in each plot); *r* is the initial size of the radial spot containing the fluorophores (here taken to be 0.85 μm to match the area monitored for intensity); and *D* is the diffusion coefficient. In fitting these data, we chose only the portion from the highest part of the dequenching peak to the decay to the background level. At the highest intensity of the peak, the curve reflects a transition from fluorescence dequenching to the relaxation of fluorescence (decay of fluorescence signal) due to only the radial diffusion of the fluorophores away from the fusion site.

The intensity data was fit with equation 1. *D* was determined as the value that minimized the sum of the square of the error between the data and fit. The results for each kind of sample are summarized in Table A2 in the Appendix A. These values are averages of the diffusion coefficients obtained from several (at least 4) single particle fusion events for each sample type and fall within the range of values obtained from the FRAP experiments. This good match confirms that the lipids remain mobile during the fusion process and that the VLP and VLSB exhibit similar characteristics during hemifusion as the native virion.

4.3.6.2. Pore formation

Membrane hemifusion is directly followed by the formation of a fusion pore, where in the native virus, the viral RNA is released into the cytosol of the host cell. To show that HA maintained full functionality to induce pore formation after membrane hemifusion, the single vesicle fusion experiments carried out for hemifusion were repeated here. In this case, the interior compartment was fluorescently labeled instead of the membrane. Release of the interior contents and subsequent loss of fluorescence indicates pore formation.

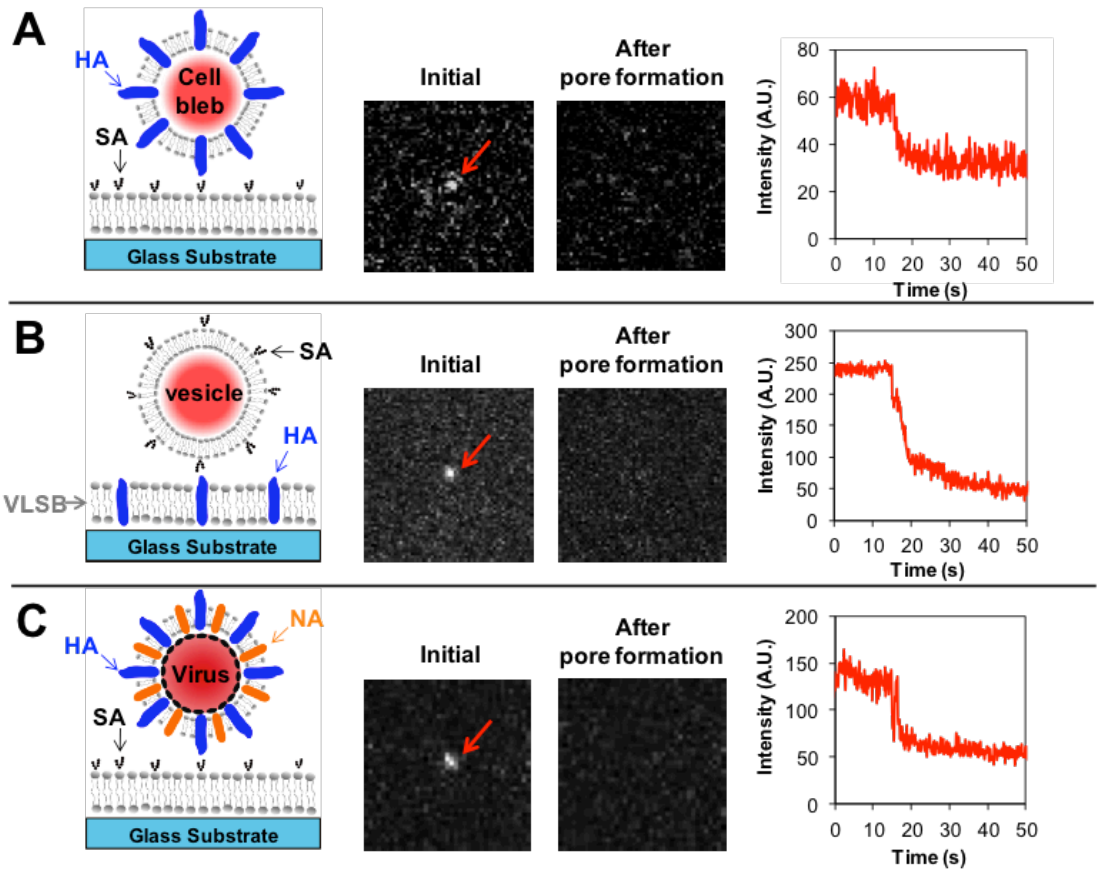

Fig. 4. Pore formation between: (A) SRB-labeled HA-bleb VLP and SA-containing supported lipid bilayer; (B) SRB-labeled SA-liposome and HA-VLSB, and (C) SRB-labeled native X-31 influenza virus and SA-containing

supported lipid bilayer. The initial images are the particles (indicated with the arrow) just before the internal fluorophores are release; the second images show the same location after the release of SRB. The plots to the right track the intensity in the local region around the particle during the release.

HA-blebs, sialic acid liposomes, and native virus were labeled with SRB, a water-soluble dye that intercalates through lipid membranes and partitions into the aqueous interiors of liposomes and virions. When the fusion pore opens the SRB is released and diffuses away from the fusion site, so a drop in fluorescence indicates when the pore formation event occurred. Both the HA-blebs and SA-liposomes dropped in fluorescence, indicating pore formation occurred in both these cases (Fig. 4, A-B). For comparison, we also ran the control case of the native virion forming a pore with a SA-containing supported lipid bilayer, shown in Fig. 4 C.

The hemifusion and pore formation experiments taken together show that HA membrane proteins, in either cell bleb proteoliposomes or embedded in supported bilayers, remain fully fusion-competent. There are two important outcomes of these results. First, these results illustrate that virus-like particles can be created using a straightforward cell blebbing technique. This simple approach to creating virus-like particles has several advantages over a prominent strategy that employs VSV virus to create pseudovirus particles. Both approaches require that a cell express the viral fusion protein of interest in its plasma membrane. In the blebbing approach, the bleb-inducing buffer is added to the culture and induces proteoliposomes “bud” from the cell resulting in virus-like proteoliposomes containing the fusion protein of the virus. In the pseudovirus approach, several more intricate infection steps with VSV and pseudovirus are required; these steps take about 3 - 4 additional days. Depending on

the application, the cell bleb approach may be advantageous for producing virus-like particles because of its much simpler procedure. Additionally, it should be possible to co-express additional viral coat proteins into the cell bleb to incorporate components of the virus as desired (in the case of influenza this might be neuraminidase or the M2 ion channel). By doing so, a useful research tool emerges that can decouple or isolate specific proteins or protein pairs for fundamental fusion studies. An exciting and related application for this technique is incorporating other desired proteins in cell blebs, in addition to the virus fusion machinery, as an avenue to reconstitute virus-like particles with designer functions such as therapeutic protein delivery. These applications are currently being undertaken in our laboratory.

The second important outcome these data illustrate is that functional, virus-like planar surfaces can be created from the cell blebs. This geometry may be useful for biosensing applications or for high throughput assays designed to quantify pathogen-host or pathogen-antiviral drug interactions. Additionally, if one can express a membrane protein of interest (not necessarily a viral protein) in a cell bleb, this technique can be used to incorporate that protein into supported bilayers without having to detergent-solubilize the membrane, purify, and reconstitute extracted proteins into liposomes. This is a significant advantage for reducing the possibility of: 1) denaturing proteins and suffering a consequent loss of function, and 2) disrupting critical protein-lipid interactions necessary to maintain proper protein activity. This method also affords the possibility to create support bilayers that capture much more of the complexity of the cell membrane, i.e. the glycocalyx, into a planar format. A planar version of the complex plasma membrane architecture can offer new features

for many in vitro biological assays and biosensing applications that already use standard supported lipid bilayers and biophysical-biochemical analytical techniques compatible with these materials.

4.4. Conclusion

In this work, membrane fusion-competent virus-like proteoliposomes and proteinaceous supported bilayers were made directly from cell plasma membranes using a cell blebbing technique. It was demonstrated in both geometries that hemagglutinin from X-31 influenza maintained both the ability to bind and fuse to sialic acid containing membranes. Analysis of the decay dynamics of the fluorescent probe during membrane hemifusion showed that fusion dynamics in the HA-proteoliposome and HA-supported bilayer are in line with the native virus fusing to chemically-similar host membrane mimics. Both the virus-like proteoliposomes and proteinaceous supported bilayers could also proceed to full pore formation, illustrating that fusion function of the HA is not disrupted by the blebbing technique. The spherical or planar geometry of the virus-like membrane has many possible applications from fundamental fusion studies and therapeutic delivery to high throughput screening of host-pathogen interactions and antiviral drugs.

Acknowledgments

We thank David Holowka and Barbara Baird for training D.A.C. on the blebbing technique and useful discussions. We thank the National Science Foundation (Grant CBET-1149452) for supporting some of this work. Some experiments were performed

at the Nanobiotechnology Center and Cornell NanoScale Facility, a member of the National Nanotechnology Infrastructure Network, which is supported by the NationalScience Foundation (Grant ECS-0335765)

CHAPTER 5

CHARACTERIZATION OF VIRAL FUSION CHARACTERISTICS USING VSV AND MLV PSEUDOTYPES

5.1 Introduction

Worldwide influenza epidemics, known as pandemics, occur when novel subtypes of influenza mutate and infect a population that has no preexisting immunity. Pandemics can result in global devastation and millions of deaths worldwide(135). Influenza A viruses are subtyped according to the antigenic properties of the hemagglutinin (HA) and neuraminidase (NA) glycoproteins. As discussed in previous chapters, HA plays a crucial role in determining host tropism, by controlling the binding and fusion of the virus to the host cell. NA plays a key role in egress, by cleaving the sialic acid-HA linkages that bind newly made viral progenies to the cell membrane. HA also contains a cleavage site that must be activated by host cell proteases before membrane fusion can take place. There are currently sixteen HA subtypes and nine NA subtypes circulating in wild birds and two subtypes circulating in humans: H3N2 and H1N1(136). Only three strains are known to have caused pandemics in humans, H3N2, H1N1 and H2N2(137, 138) (this strain is not currently circulating in humans but caused epidemics between 1957 and 1968).

In recent years, highly pathogenic avian influenza (HPAI) has emerged as a new global pandemic threat. The first case of HPAI H5N1 was reported in humans in 1997(120) and since then 562 human cases have been confirmed in 15 countries, with

a fatality rate of 59%(139). The biosafety hazard associated with such a highly pathogenic virus means that studying the native H5N1 virus is restricted to biosafety level 3 facilities, which can limit the type of experiments performed and speed at which data can be collected. However, certain aspects of H5N1's pathogenicity may be attributed to the HA protein. It is hypothesized that HPAI H5N1 viruses arose from mutations in the HA cleavage site, when a low-pathogenic avian virus jumped from wild birds into domestic birds(140). Another important aspect of HPAI H5N1 infection is host cell receptor type. H5N1 preferentially binds to α-2-3 linked sialic acid, which is predominantly found in birds(141, 142). Human sialic acid moieties typically have an α-2-6 linked sialic acid. These binding properties make it difficult for H5N1 to spread rapidly among humans, like H1N1 did. However, it has been shown that α-2-3 linked sialic acids are present in the lower respiratory tract of humans and there is a constant threat of mutations in H5N1, which could confer preferential binding to α-2-6, linked sialic acids. Thus by studying the envelope glycoproteins of highly pathogenic influenza in isolation from the native virus more insight into how pandemic strains arise could be gained in safe manner. One, well-established way of studying viral envelope glycoproteins is to use utilize viral pseudotyping.

Pseudotyped viruses contain the backbone and genome of one type of virus, which propagates readily in cell culture and is safe to work with, and the envelope protein of a different virus(143). Vesicular stomatitis virus (VSV) is commonly used as the viral backbone as it readily forms pseudotypes with envelope proteins from many different viruses(144-146). In 1997, Takada et al(118) developed a VSV-

pseudotyping system to study the Ebola Reston virus glycoprotein (ResGP). Using techniques developed by Lawson et al(147) and Whelan et al(148) they generated recombinant VSV that contained the green fluorescent protein gene (GFP), instead of the VSV G protein, which was designated VSVΔG*-GFP. The recombinant viruses are non-infectious unless the viral proteins required for binding and fusion are supplied by transfection. GFP was used as a fluorescent readout to measure the transduction efficiency of VSVΔG*-GFP in cells that were transfected with Ebola Reston GP. Upon egress from the transduced cell line, VSVΔG*-GFP budded through the plasma membrane, which coated the VSV nucleocapsid with Ebola Reston GP and the resultant pseudotyped viruses were designated VSVΔG*-ResGP. By infecting Vero cells, Takada et al, demonstrated that Ebola virus GP is sufficient for attachment and entry into cells.

Gammaretroviruses like murine leukemia virus, MLV, has also been used for influenza pseudotyping(149-151). Construction of MLV pseudotypes is achieved by introducing a foreign envelope gene, retroviral gag-pol construct and a transfer gene into producer cells, typically human embryo kidney (HEK) 293T cells (152). The gag-pol construct contains two genes that encode the matrix nucleocapsid p7 from gag and reverse transcriptase, protease and integrase expressed from pol. The transfer gene usually contains GFP or luciferase to measure transduction. MLV-HA pseudotypes have been used to develop in cell-based antiviral assays to screen for anti HA and NA drug resistance(149). Wang et al constructed retroviral particles pseudotyped with high pathogenicity H5 from A/Vietnam/1194/04, with a luciferase reporter gene. These pseudoviruses were used in a high-throughput assay to screen for HA inhibitors.

Entry of H5 pseudotypes into human lung carcinoma A549 was blocked by α-2,3SialGal oligosaccharides and also by a newly discovered synthetic peptide P7B3(149)

However there are some drawbacks to using pseudotyped systems to study viral entry. Some viruses acquire a lipid membrane at the endoplasmic reticulum e.g. flaviviruses(153) and produce low titers when their envelope proteins are expressed in pseudotype producer cells. A second important difference between native viruses and their pseudotyped analogues is the density of glycoproteins on the viral surface. The density of envelope glycoproteins on the pseudotype surface is difficult to control and predict(152). If the protein density is significantly lower, antibodies may more readily neutralize the pseudovirus compared to the native virus(152). Finally for VSV based pseudotyping, morphology may also impact entry dynamics when compared to the live virus. VSV is bullet shaped and there is some evidence that fusion usually occurs between the flat end of the virus and the viral membrane (154). In the case of HA-VSV pseudotypes this could significantly change the energetics associated with fusion, since native HA-mediated membrane fusion typically takes between a spherical of pleomorphic particle and the endosomal membrane. It is therefore important to evaluate entry kinetics of pseudoviruses with a resolution technique, like the single virion fusion assay(23, 97). In this chapter we compare the fusion kinetics of native influenza X:31 to VSV-H3/X31 and observe that the presence of neuraminidase in the viral envelope could impact fusion kinetics. We also evaluate the binding and fusion behavior of influenza H2/Japan/57 in pseudotyped form, a strain that unfortunately cannot be compared to the native virus. By doing so, new insight

into the relationship between receptor binding and fusion of H2 viruses is shown. Finally, we show that the MLV pseudotyping system can be used to learn new information regarding the cellular entry process of the newly emerged Middle Easter respiratory virus (MERS)(155, 156).

5.2 Materials and Methods

5.2.1 Materials

The following lipids were used in these experiments: 1, 2 dioleoyl-*sn*-glycero-3-phosphocholine (DOPC), 1-oleoyl-2-palmitoyl-sn-glycero-3-phosphocholine (POPC), cholesterol, total ganglioside extract (bovine, brain) and total liver extract. These were obtained from Avanti Polar Lipids (Alabaster, AL). The fluorescently labeled lipid, Oregon green 488 DHPE (Molecular Probes, Eugene, OR), was used to conduct fluorescence recovery after photobleaching experiments and to detect the pH drop in acidic flow experiments. Biotechnology grade chloroform and methanol for preparation of vesicles were purchased from Sigma-Aldrich. Polycarbonate filters (Whatman Nucleopore) with pore diameters of 100 nm and 50 nm were used in the preparation of vesicles. Glass coverslips (25 mm x 25 mm; No. 1.5) from VWR were used as supports for the bilayers. Sulfuric acid and hydrogen peroxide used to clean the glass coverslips were purchased from VWR. Polydimethylsiloxane (PDMS; Sylgard 184) used to fabricate microfluidic flow cell devices was purchased from Robert McKeown Company (Branchburg, NJ). Sodium chloride salt (NaCl) and (2-(N-Morpholino) ethanesulfonic acid sodium salt (MES) used to make buffers were

purchased from VWR. Influenza X:31 (H3N2) was purchased from Charles River Labs (Wilmington, MA). Octadecyl Rhodamine B chloride (R18) and Sulforhodamine B (SRB) used to label the virus were purchased from Molecular Probes (Eugene, OR). G-25 spin columns used in virus labeling and purification were purchased from GE Healthcare. Triton-X (J.T. Baker) detergent used in virus labeling optimization was purchased from VWR.

Rhodamine 110 chloride and 1-octadecanol were purchased from Sigma Aldrich for the synthesis of the Rhodamine 110 octadecyl ester (R110C18). The concentrated sulfuric acid used to start the synthesis reaction was purchased from VWR and the triethylamine used to stop the reaction was purchased from Acros Organics. Silica Gel 60 (63-200 μm particle diameter) was purchased from EMD and Neutral Alumina (50-200 μm particle diameter) was purchased from Dynamic Adsorbents, Inc.) in order to purify the dye product using column chromatography. Isopropanol, chloroform, and methanol were all purchased from VWR to make the elution solvents.

5.2.2 Surface Preparation

Glass microscope coverslips (25 mm x 25 mm; No. 1.5) were cleaned in piranha solution (70% sulfuric acid, 30% hydrogen peroxide). Slides were immersed in 150 ml of piranha solution for ten minutes. The slides were subsequently rinsed for 30 minutes with copious amounts of deionized water with a minimum resistance of 18.2 MΩ·cm obtained from a Siemens Purelab Ultra water purification system. Clean slides were stored under deionized water, then dried with a stream of ultra pure nitrogen gas prior to use.

5.2.3 Microfluidic Device Fabrication

Microfluidic devices for the fusion experiments were fabricated as described in previous chapters.

5.2.4 Synthesis of R110C18

For experiments examining just the hemifusion step, R110C18, a green-emitting fluorophore, was used. R110C18 was synthesized following the procedure in Floyd et al(21, 157).

5.2.5 Cells and plasmids

Baby hamster kidney-21 (BHK-21) and madine darby canine kidney (MDCK) cells, obtained from the American Type Culture Collection (ATCC, Manassas, VA), were grown and maintained in Dulbecco's modified Eagle medium (DMEM, CellGro) supplemented with 10% fetal bovine serum (Gibco), 100 U/ml penicillin and streptomycin and 10% HEPES.

The following plasmids were used: pCAGGS-H3/X31, pCDNA3-H2/Japan/1957, pCAGGS-VSVG, pCAGGS-N2/MS96 encoding the influenza hemagglutinin HA X-31, influenza hemagglutinin H2/Japan/1962, vesicular stomatitis virus G protein and influenza neuraminidase MS96 respectively. pCAGGS-H3/X31 was a generous gift from David Steinhauer. The pCAGGS vector was used as an empty vector control.

5.2.6 Preparation of VSV pseudoparticles

BHK-21 cells were transfected with pCAGGS-H3/X31, pCAGGS-H2/Japan/1962, pCAGGS-VSVG or pCAGGS by using TurboFect (Invitrogen). 24 hours after transfection cells were infected with VSVDG*-G. Cells were incubated with rocking at 37^{o}C, 5% CO_2 for 2 hours to facilitate virus adsorption and entry. Cell were washed three times with DPBS and incubated in DMEM for 24 hours at 37^{o}C, 5%CO_2. Transduction of BHK-21 cells with VSVDG*-G was confirmed by the observation of GFP expression using a Zeiss inverted microscope. Cell supernatant was collected and cell debris was cleared by centrifugation at 3000RPM for 10 minutes at 4^{o}C. Virus stock was then stored at -80^{o}C.

5.2.7 Infection of MDCK cells with influenza VSV pseudoviruses

MDCK cells were grown seeded at a density of 6 x 10^4 cells/ml in 24 well plates. VSV pseudoviruses containing hemagglutinin were treated with TPCK-treated trypsin at 2μg/ml and incubated at 37^{o}C for 15 minutes. Trypsin inhibitor was then incubated with the virus for at least 5 minutes.

5.2.8 Lipid Vesicle Preparation

The following lipids were used in these experiments: 1, 2 dioleoyl-*sn*-glycero-3-phosphocholine (DOPC), 1-oleoyl-2-palmitoyl-*sn*-glycero-3-phosphocholine (POPC), cholesterol, and total ganglioside extract (bovine, brain). Lipid vesicles were prepared

using a molar ratio of 4:4:2:0.5.01 of DOPC, POPC, cholesterol, total ganglioside extract and Oregon green DHPE. Liposomes were prepared using the same techniques described in previous chapters

5.2.9 Virus Membrane Labeling and Purification

To fluorescently label the viral pseudotype membranes, 20 μL of virus and 3.5 μL of R110C18 were added to 250μL of buffer A. The mixture was sonicated gently in a water bath for one hour. Free R110C8, which did not insert into the viral membrane, was removed from labeled virus using a G-25 spin column for two minutes in a centrifuge (Eppendorf, Centrifuge 5451C, Hauppauge, NY) at rate of 3x1000 min^{-1}. The supernatant containing the purified virus was diluted with 600μL of buffer A and gently vortexed to mix the virus and buffer.

5.2.10 Marking the Onset of Hemifusion by Fluorescence Dequenching

In this assay, membrane hemifusion events are detected by the dequenching of a fluorescent membrane probe R110C18 located in the viral membrane. In this example, VSV-H3N2 was incubated with R110C18, until enough R110C18 partitioned into the viral membrane so that neighboring fluorophores quench each other, as described in the virus labeling procedure above. During fusion, when the outer monolayers of the viral and supported membranes mix, the fluorophore gets diluted and a sharp increase (spike) in fluorescence (dequenching) is observed as shown in Figure S2. Following the ‘spike’ in fluorescence, the fluorescent probe diffuses away from the hemifusion site, thus indicating that these are true fusion events and the fluorescence increase,

which marks the onset of hemifusion, and is not a result of a viral particle changing its position in the evanescent field.

5.3 Results & Discussion

5.3.1 Production of H3 and H2 VSV-pseudotypes

VSV pseudotypes were produced according to procedures designed in the Whittaker lab. In this study we investigated the effect of producing HA-VSV pseudotypes with and without endogenous neuraminidase (NA). We produced 6 different types of HA-VSV pseudotypes, VSV-H3/X31, VSV-H2/Japan, VSV-H3X31/N2MS96, VSV-H3X31/N1ACal09, VSV-H2Japan/N2MS96 and VSV-H2Japan/N1ACal09, which shall be hereafter referred to as VSV-H3, VSV-H2, VSV-H3N2, VSV-H3N1, VSV-H2N2 and VSV-H2N1 respectively. To produce pseudotyped viruses, BHKmw cells were transfected with the appropriate DNA plasmids for the membrane protein to be expressed or co-expressed in the BHKmw plasma membrane. Transfected cells were then transduced with a recombinant VSV supplied by the Whittaker lab, VSVΔG/GFP-G*. The recombinant virus contains the gene for GFP instead of the VSV G fusion protein and GFP expression is used as a fluorescent readout for successful cell infection with recombinant virus. VSVΔG/GFP is replicated within the cells and upon egress through the plasma membrane, pseudotyped viruses are formed because the viral membrane envelope contains the heterologous membrane proteins HA and NA *(figure 1)*. MDCK cells, which contain receptors for influenza, are infected with pseudotyped viruses and GFP expression indicates successful infection as shown in *figure 2*. The highest levels of fluorescence were obtained in cells infected

with H3N2 and H2N2. VSV-G and VSV-Δenv pseudotypes were produced as positive and negative controls (*figure 2*). Cells infected with VSV-Δenv exhibited almost no fluorescence, while VSV-G showed high levels of infection, which is typical for VSV infection in MDCK cells.

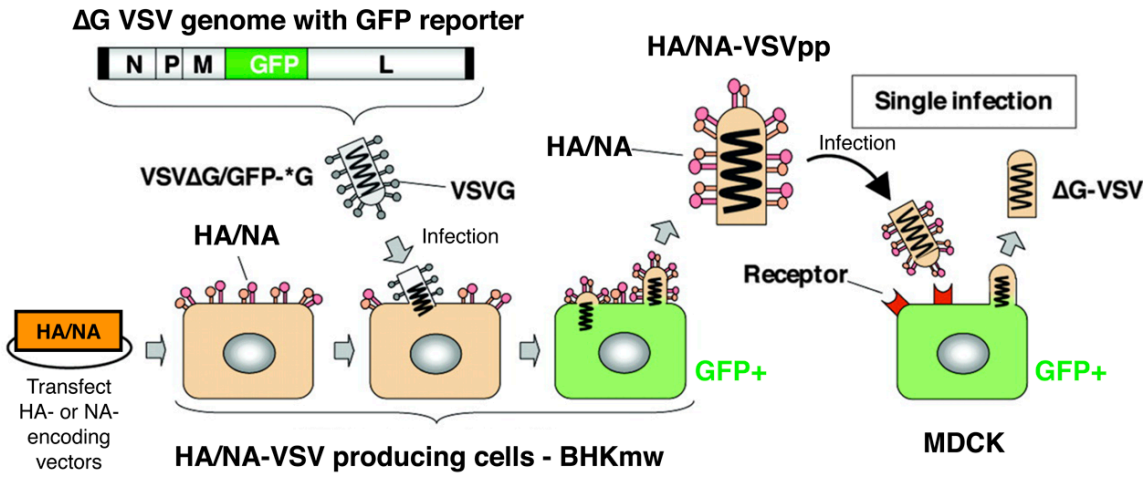

Figure 1. Schematic representation of vesicular stomatitis virus (VSV) pseudotyping. BHKmw cells are transfected with heterologous HA and NA proteins and infected with the recombinant VSV virus, VSVΔG*-GFP. Successful transducion of BHKmw cells results in expression of GFP gene encoded in the VSV genome. HA/NA proteins are acquired by VSV as it buds from the BHKmw cells to prodcue VSV-HA/NA. MDCK cells are infected with VSV-HA/NA and GFP expression indicates successful pseudotyping with HA protein.

5.3.2 Single particle kinetic measurements of pseudotype VSV-H3N2 fusion to supported lipid bilayers

Influenza HA binds to sialic acid residues on the plasma membrane and triggers the uptake of the virus into the cell via clathrin-mediated endocytosis. Inside the endosome, the HA undergoes a conformational change at acidic pH's and induces

fusion of the viral and endosomal membranes and viral RNA is released. Fusion is a multistep process involving hemifusion (merging of the outer lipid monolayers of the viral and endosomal membrane) and pore formation (the formation of pore in the merged membranes that facilitates the release of RNA). We used total internal reflection microscopy (TIRFM) to visualize the binding, hemifusion individual pseudotyped virions to supported lipid bilayers in microfluidic channels. To visualize hemifusion, virions were incubated with a quenched concentration of the lipophilic dye, R110C18, which inserts into the viral membrane. Excess dye that did not insert into the membrane was removed in a size exclusion column. Prior to labeling with R110C18, pseudoviruses were treated with TPCK-trypsin for 15 minutes in order to cleave the precursor HA0 into HA1 and HA2, which is essential for membrane fusion. The virus solution is then drawn into a microfluidic channel coated with a supported lipid bilayer containing a mixture of DOPC, POPC, cholesterol and 5 mol% total ganglioside extract, which contains the sialic acid receptor. Fusion is triggered by buffer exchange with low pH buffer in the channel and the time at which acidification is indicated by a drop in fluorescence of a pH sensitive fluorophores (Oregon green DHPE) in the bilayer. Hemifusion is marked by a sharp increase in fluorescence as the dye from the viral membrane mixes with the supported bilayer and diffuses radially away from the site of hemifusion. The hemifusion lag time (t) is defined as the time elapsed between acidification and the

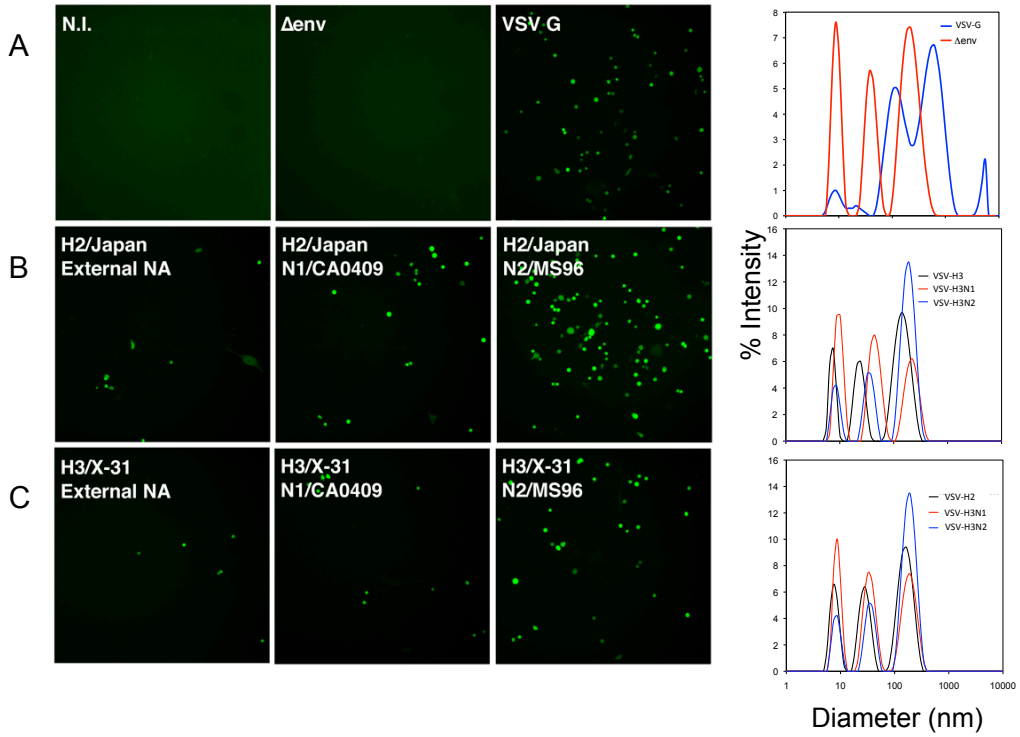

Figure 2. Infection of MDCK cells with VSV-pseudotypes. The level of GFP expression in MDCK cells is indicative of successful infection. Panel A) shows postive and negative control experiments, N.I. cells were not infected, Δenv particles contain no heterologous membrane protein and VSV-G shows high expression of GFP due to recombinant of the pseudotype virus with G protein. Dynamic light scattering (DLS) results show the size distributions of particles obtained from each supernatant. Panel B) depicts infection with 3 pseudotypes of H2/Japan/1952 either treated with exogenous neuraminidase (NA) or co-transfected with plasmids for N1/ACal/09 or N2/MS96 and the respective DLS results. Panel C) is the same as panel B except the H2/Japan/1957 plasmid has been switched for H3/X31

peak of the hemifusion traces shown in figure 3. This lag time is collected for each fusing virus in the field of view and plotted as a cumulative distribution (figure 3D) as a function of time. This distribution is described by the gamma distribution:

$$p_H = \int_0^t \frac{k_H^N t^{N-1}}{\Gamma(N)} e^{-k_H t} dt \qquad (1)$$

where k_H is the hemifusion rate constant and N is the number of HA proteins required for hemifusion (figure 3). The gamma distribution is used as fusion events occur stochastically and independent of each other. Each fusion event is a multistep process,

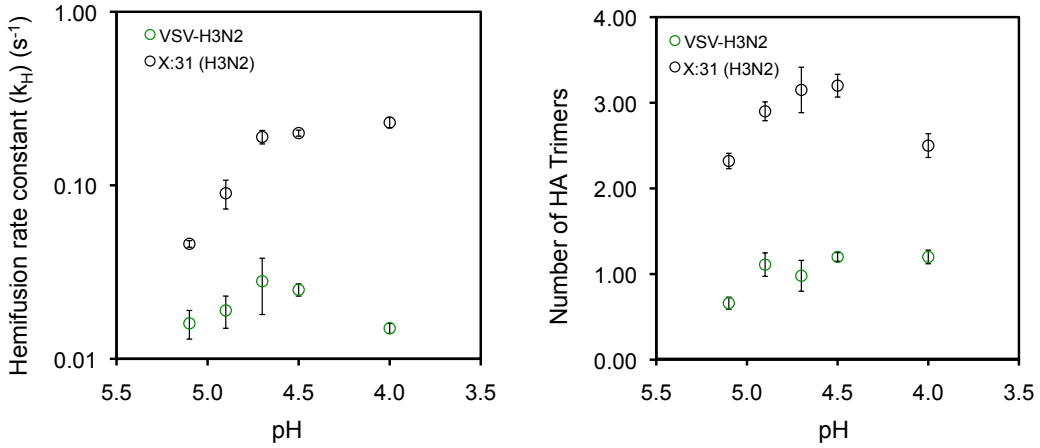

Figure 4 compares the hemifusion rate constants and number of HA trimers, determined from the gamma distribution, as a function of pH for native X:31 (black open circles) and pseudotypes VSV-H3N2 (green open cirlces).

with each step in the process being described by a Poisson distribution. The gamma distribution is thus a convolution of a multistep Poisson process. Fusion experiments were monitored for 3-4 minutes at rate of 10 frames per second.

The kinetic parameters k_H and N, were determined for VSV-H3N2 fusion for pH values ranging from 5.1 to 4 (figure 3). As shown in figure 3, the rate of fusion of VSV-H3N2 is significantly slower than native X:31 (data from chapter 2) at each pH

value. At pH 4.7, the maximum kH value for X:31, VSV-H3N2 is an order of magnitude slower than H3N2/X:31. As previously discussed in chapter 2, the hemifusion kinetics of X:31 are strongly dependent on pH. The rate of hemifusion increases almost linearly at from pH 5.3 to 4.7 and plateaus at the 'optimal' fusion pH. It is not evident from the data shown in figure 3 that VSV-H3N2 exhibits the same dependence on pH. While the maximum rate of fusion of VSV-H3N2 also occurs at pH 4.7, the error associated with the parameter falls within the rate constants values associated with the adjacent pHs, thus it can be concluded that the fusion of VSV-H3N2 is independent of pH.

The number of HA trimers (N) required for VSV-H3N2 fusion was also calculated and compared to native X:31 (figure 3). At high, physiological pH values, N for X:31 is found to be approximately 3. Our fusion data shows that for VSV-H3N2, N is consistently close to unity as a function of pH. This suggests that only one HA trimer is required for fusion in this VSV pseudotyped system. However, since hemifusion is a multi-step process, an N value equal to 1 could indicate that one step in hemifusion process e.g. the conformational change of HA, may occur so slowly that kinetics are dominated by this single steps, thus resulting in a gamma distribution where N=1.

There are several possibilities for the reduction fusion rates of VSV-H3N2. It is possible the bullet shaped morphology of VSV is responsible for the reduction in k_H and N for VSV-H3N2. It has been suggested that VSV fuses to membranes at the flat end of the 'bullet'(158). Native X:31 is spherical to pleiomorphic in shape. Thus the energy required to mediate fusion between two almost planar membranes may be

markedly higher than for VSV pseudotypes than the native virus. Hemifusion could therefore be limited by the timescale for a sufficient number of HA trimers to undergo conformational changes and induce fusion. A second possibility is that the density of HA trimers on the surface of VSV-H3N2 is markedly reduced compared to native influenza viruses and this may have a profound effect on the hemifusion kinetics of influenza-VSV pseudotypes. While VSV is less selective than MLV pseudotypes when acquiring membrane proteins during egress, it is still very difficult to quantify the level of HA coverage on the VSV surface. The density of HA on native influenza has been shown to be vital for membrane fusion(14, 54, 159). We chose to co-transfect with NA to improve virus yield but it has also been suggested that NA helps in the trafficking of HA from the Golgi to the plasma membrane. In these experiments we co-expressed N2/MS96 with H3/X31. This combination of HA and NA resulted in the highest MDCK infection efficiency, however the mismatch between these proteins could play a role in the observed fusion kinetics. A more accurate VSV-pseudotype of X:31 requires co-expression of N2/X31 with H3/X31. This work is currently ongoing on in our lab.

5.3.3 Fusion of VSV-H2N2 to total liver extract supported bilayers

In the previously described pseudotype production, we produced VSV-H2N2 pseudoviruses. The HA protein for these pseudoviruses was originally cloned from influenza A/H2N2/Japan/305/57. These experiments describe the first single virion kinetic analysis of hemifusion mediated by the H2 protein. Influenza A/H3N2/Japan/305/57 is a biosafety level 3 virus, thus we cannot compare the kinetics

to those of the native strain. However, the kinetics of fusion mediated by H2 rather than H3 may be analyzed by comparing VSV-H2N2 to VSV-H3N2, which demonstrates the utility of viral pseudotyping systems. Fusion experiments involving VSV-H2N2 were set up as described in the previous section. As show in figure 2, VSV-H2N2 showed the highest level of GFP expression upon inoculation in MDCK cells. However, fusion of VSV-H2N2 with DOPC, POPC, cholesterol and 5 mol% total ganglioside extract (TGE), supported bilayers was unsuccessful. As show in figure 5, binding of VSV-H2N2 was observed but upon buffer exchange with low pH buffer almost no fusion events occurred. The predominant species in total ganglioside extract is monosialoganglioside (GM_1), with an avian type, α (2,3) sialic acid-galactose linkage. Previous work by Suzuki et al(160), showed that native A/H2N2/Japan/305/57 bound preferentially to α (2,6) sialic acid-sugar linkages. It is difficult to commercially procure purified α (2,6) sialic acid ganglioside for incorporation into supported bilayers. In order to more closely mimic an environment where α (2,6) sialic acids may be present, we decided to use bovine total liver extract (TLE) that is commercially available from Avanti polar lipids.

The exact composition of TLE is unknown. The approximate composition of is 42% phosphatidylcholine (PC), 22% phosphatidylethanolamine (PE), 8% phosphatidylinositide (PI), 1%Lyso PI, 7% cholesterol and 20% unknown lipids. We hypothesized that these unknown lipids may contain gangliosides containing α(2,6) and α(2,3) sialic acids. As described in previous chapters, lipid mobility on the glass substrate is essential for fusion to occur. We first tested the mobility of pure TLE in a microfluidic channel using standard fluorescence recovery after photobleaching

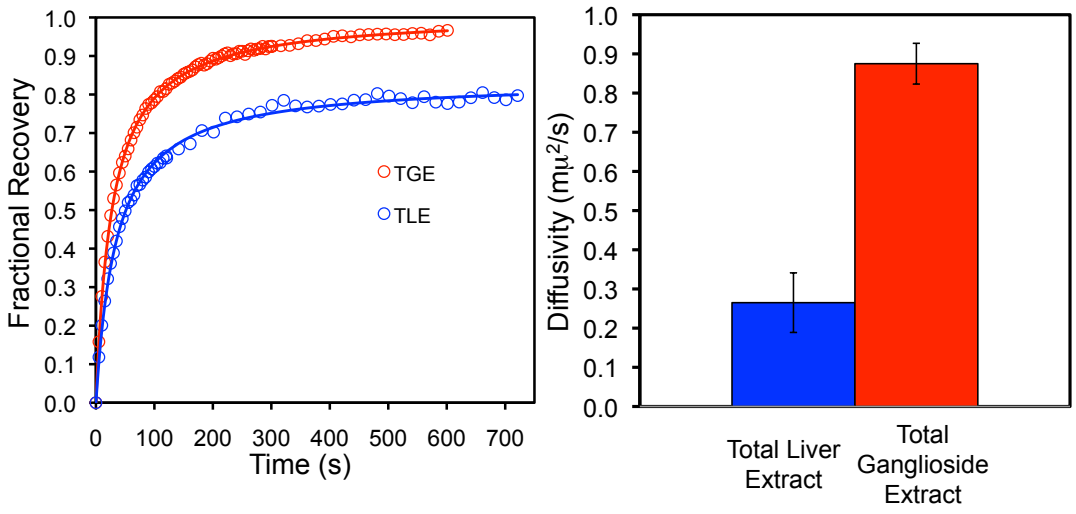

Figure 5. Fluorescence recovery after photobleaching (FRAP) of total ganglioside extract (TGE) and total liver extract supported lipid bilayers, characterized in microfluidic channels described in the methods section.

(FRAP) methods (108). Unfortunately we could not form consistently mobile and contiguous bilayers using pure TLE. Using the same method described in chapter 3 for making cell bleb bilayers, we diluted the TLE lipids and adsorbed the vesicles to the glass substrate. Using a similar strategy described in chapter 4(46), BHK lipids devoid of gangliosides were then flown into the channel and incubated for at least 4 hours to obtain mobile, contiguous supported lipids bilayers. The diffusion coefficient for the TLE/BHK mixture was determined using FRAP to be approximately 0.25$\mu m^2/s$.

Next we performed VSV-H2N2 fusion experiments as previously described using TLE/BHK supported bilayers. Due to the quenched state of the virions upon binding, it was difficult to quantify if binding had been significantly enhanced.

However upon the low pH trigger, VSV-H2N2 underwent the typical hemifusion reaction as shown in figure 4. In the same microfluidic device in different channels, it was found on separate days that while VSV-H2N2 could bind to bilayers containing TGE but could never fuse, while in the same device the virus could bind and fuse to TLE/BHK bilayers. Hemifusion kinetics were determined for VSV-H2N2 as previous described using a gamma distribution (figure 5). Despite the low mobility of TLE compared to TGE, hemifusion of VSV-H2N2 occurred at a rate comparable to native X:31 fusing to TGE lipids. However unlike native X:31 and VSV-H3N2, almost no hemifusion activity was observed above pH 5.

These results display the utility of using single virion fusion assays to examine viral entry. This data represents the first individual virion visualization of membrane fusion mediate by a H2 serotype. However, the observation that VSV-H2N2 fusion is dependent on the composition of the lipid bilayer is striking. VSV-H2N2 can bind to TGE bilayers but upon acidification the virions almost never undergo hemifusion, in stark contrast to experiments performed on TLE bilayers. Although LCMS must be carried out to determine the sialic acid composition of TLE, this data still reveals important information about H2N2 entry into cells. The requirement of HA-sialic acid binding for fusion has long been a source of debate for virologists. Work carried out using bulk assays to determine the effect of receptors on fusion indicated that HA-sialic acid binding actually impeded fusion(55). However both experiments described in this chapter and previous work by Niles et al(62) indicate that receptor binding is indeed essential for genome release. This data extends this observation by showing that although binding can occur between H2N2 and α(2,3) sialic acids, fusion will

almost never occur even upon triggering with low pH, unless bound to a specific sialic acid or unknown ganglioside or lipid found in TLE bilayers. This highlights the importance of using techniques to distinguish between binding and fusion, as this data shows successful binding does not guarantee successful genome release.

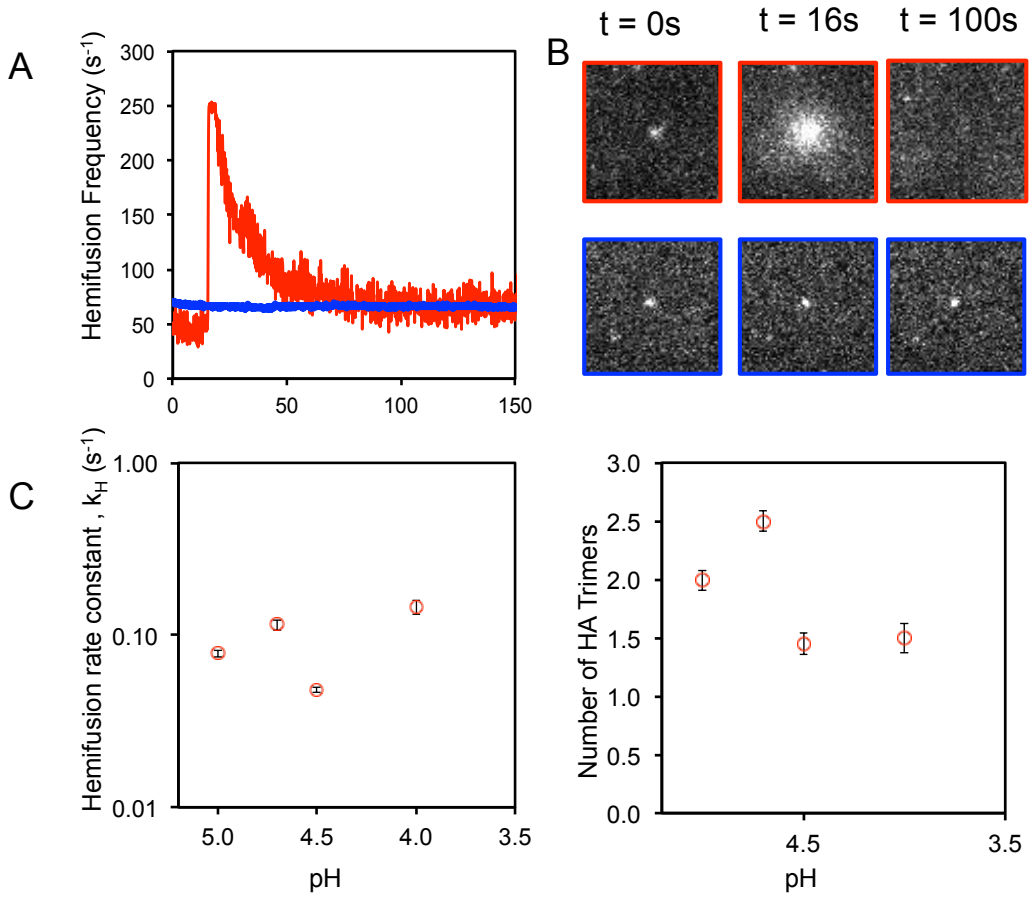

Figure 5 Fusion kinetics of VSV-H2N2 pseudotype viruses. A) Dequenching of R110C18 in the VSV-H2N2 in the lipid envelope upon lipid mixing with the target supported lipid bilayer (red line -TLE, blue trace – TGE). B) TIRFM images of VSV-H2N2 fusion to TLE (red) and TGE (blue) lipid bilayers. C) Hemifusion rate constant and number of H2 trimers required for hemifusion as function of pH determined from the gamma distribution.

5.3.4 Preliminary MLV-Pseudotyping fusion assay

One of key advantages of using viral pseudotypes is the ability to study the entry kinetics of highly pathogenic viruses with reduced risk of exposure to the pathogen. In the Whittaker laboratory at Cornell, pseudotyped MERS viruses were produced using retroviral pseudotyping. 293T cells were transfected with murine leukemia virus structural (*gag*), enzymatic (*pol*) genes, GFP and the spike gene (S) from MERS virus (*figure 6*). Mature retroviral particles containing MERS S protein in the lipid envelope were harvested from the supernatant. The receptor for MERS virus was recently identified to be dipeptidyl peptidase 4 (DPP4)(39). As described previously for coronavirus fusion(23), we utilized our cell blebbing method to integrate DPP4 into a supported lipid bilayer in our microfluidic platform for investigating viral fusion. MLV-MERS was treated with TPCK-trypsin to cleave the S protein. The virus was then labeled as previously described with R110C18. MLV-MERS did not bind or fuse to membranes devoid of DPP4. Unlike FECV-1683, MLV-MERS did not fuse upon binding at pH 7. Fusion was only triggered upon exposure to low pH. At pH 4.7, k_H and N were determined to be $0.03s^{-1}$ and 0.8 respectively. This preliminary work highlights the importance of integrating high resolution microscopy techniques and viral pseudotyping to study emerging viral pandemics.

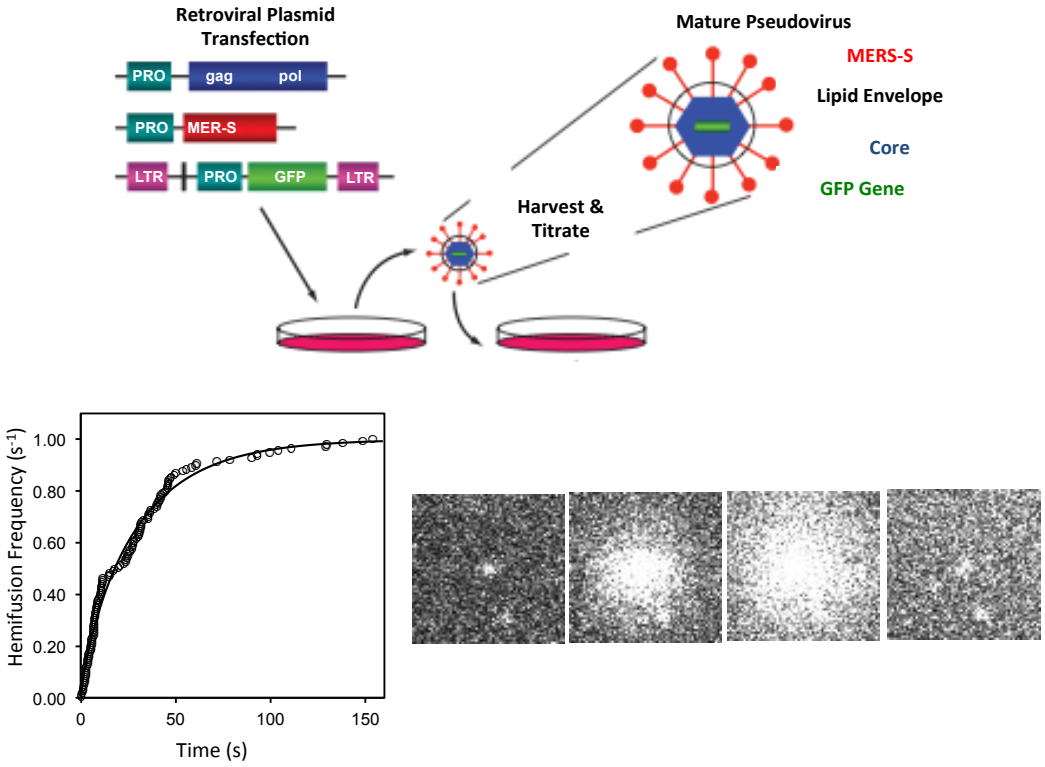

Figure 6 Murine leukemia virus (MLV) retroviral pseudotyping of MERS S protein. A) Schematic of MLV pseudotyping in HEK 293T cells. Cells are transfected with DNA coding for MLV *gag* and *pol* genes, green fluorescent protein (GFP) and the MERS S protein and MLV-MERS viruses are collected from the cell supernatant and titrated against Vero E6 cells) Cumulative distribution function depicting hemifusion frequency of MLV-MERS to supported bilayers containing human DPP4 protein at pH 4.5, fit with a gamma distribution. k_H and N were determined to be $0.03s^{-1}$ and 0.8 respectively. B) also shows TIRFM image series of MLV-MERS hemifusion to the aforementioned supported lipid bilayer at pH 4.5.

CHAPTER 6

CONCLUSIONS & OUTLOOK

This thesis has presented several advancements to methods of studying membrane-enveloped virus host interactions. Single particle tracking techniques (SPT) offer new insight into the mechanisms that govern how viruses enter cells and cause local or systemic infection. This work provides solutions to the drawbacks associated with current techniques and extends their applications to study a potentially wide range of membrane-enveloped viruses.

By integrating a novel proton uncaging technique into the previously described fusion assays(21), we have addressed inherent difficulties associated with using acidic hydrodynamic buffer exchange as a method to trigger pH dependent membrane fusion of influenza viruses. Employing this method, we found that optimal number of HA trimers required for fusion could be 1 or 2, which is less than previously determined using experimental techniques. From a practical standpoint, this work demonstrates the importance of techniques with high temporal resolution when monitoring fusion reactions with millisecond timescales. This novel proton uncaging technique could thus be extended to study the fusion of other membrane-enveloped viruses and other protein mediated fusion processes such as snare-mediated fusion. Another significant advantage of using this quiescent method of initiating membrane fusion is that now both virus binding and fusion can be observed for a single virus, in one combined assay. This option was not feasible using acid buffer exchange, as the shear force

generated washes many bound and unbound virions out of the field of view making combined binding and fusion analysis impossible.

One of the biggest limitations with using SPT assays to study virus fusion is the narrow range of viruses that can be studied. This thesis presents a method of extending SPT assays beyond influenza A, vesicular stomatitis virus and Sindbis virus (all viruses that bind glycolipids) to viruses that bind proteinaceous receptors(23). Using cell-blebs to create supported lipid bilayers that contain functional, enzymatically proteinaceous receptors, the first single virion fusion measurements of coronavirus were obtained. The ability to monitor binding and fusion with unprecedented detail revealed that the fusion of feline coronavirus (FCoV) requires a low pH, but unlike other class 1 fusion proteins like HA, the rate of conformational change of the spike protein S, is independent of proton concentration. This technique provides a new way to investigate and control the sequence of proteolytic cleavage of spike, binding and fusion, which could provide insight into how zoonotic viruses adapt to new hosts. In the future, the role of receptor co-factors in viral entry could also be investigated. By co-expressing both the viral protein receptor and a putative proteinaceous co-factors in cell blebs, the effect of these co-factors on entry or host tropism can be investigated in-vitro. One example where this would be beneficial is in studying HIV entry. The HIV fusion protein, gp160, interacts with the CD4 protein on the cell surface and a variety chemokine receptors also expressed on the cell surface (typically CCR5 or CXCR4)(161, 162). By selectively deleting certain species from the membrane, one could assess their impact on efficiency of HIV fusion.

Identification of new co-factors in HIV infection could lead to the development of new antiviral drugs.

Another important result outlined in this thesis, is the development of new tools to study highly pathogenic viruses with minimized safety concerns. RNA free virus-like proteoliposomes (VLPs)(46) are a simple system for examining the fusion kinetics of a range of dangerous pathogens, that naturally extended from our blebbing procedures developed here. VLPs are also versatile because they can be used to form virus-like supported bilayers (VLSBs), as demonstrated with HA protein. HA was shown to be capable of undergoing a pH triggered even when embedded in a supported bilayer. VLSBs thus have potential applications in high-throughput screening of small molecule antivirals or antibody therapies.

This research also presents the first single virion analysis of viral pseudotype fusion. VSV and MLVs are also useful and commonly used tools for studying the fusion proteins of highly pathogenic viruses. Until now, there have been no direct comparisons of the fusion activity of a native virus with its pseudotyped counterpart. This work highlights the importance of using high-resolution techniques to probe entry mechanisms of these proxy particles. While VSV-X31 underwent hemifusion in the same manner as native X:31, the kinetics were markedly different. This result calls into question the importance of neuraminidase in the fusion process, which has been previously unexplored. Future work on this project could involve co-expressing different combinations of HA and NA in VSV pseudotypes and comparing infection and fusion efficiency. Finally, by combining the method of embedding proteinaceous receptors in supported lipid bilayers and viral pseudotyping the first fusion events

mediated by MERS spike proteins were observed. This work highlights the multiple improvements made to SPT virus fusion assays and opens this technique to have a broader impact on how virus-host interactions are studied and the speed at which emerging pandemic strains may be characterized.

7. REFERENCES

1. Chernomordik LV, Kozlov MM. Membrane hemifusion: Crossing a chasm in two leaps. Cell. 2005;123(3):375-82.

2. Harrison S. Mechanism of membrane fusion by viral envelope proteins. Advances in virus research. 2005.

3. Steinhauer D. Role of hemagglutinin cleavage for the pathogenicity of influenza virus* 1. Virology. 1999.

4. Kemble GW, Henis YI, White JM. Gpi- and transmembrane-anchored influenza hemagglutinin differ in structure and receptor binding activity. The Journal of cell biology. 1993.

5. Hoekstra D, Düzgüneş N. [2] lipid mixing assays to determine fusion in liposome systems. Methods in enzymology. 1993;220:15-32.

6. Van Meer G, Davoust J, Simons K. Parameters affecting low-ph-mediated fusion of liposomes with the plasma membrane of cells infected with influenza virus. Biochemistry. 1985;24(14):3593-602.

7. Wilson I, Skehel J, Wiley D. Structure of the haemagglutinin membrane glycoprotein of influenza virus at 3 Å resolution. naturecom. 1981.

8. Weis W, Cusack S, Brown J, Daniels R. The structure of a membrane fusion mutant of the influenza virus haemagglutinin. The EMBO …. 1990.

9. Skehel J, Bayley P, Brown E. Changes in the conformation of influenza virus hemagglutinin at the ph optimum of virus-mediated membrane fusion. Proceedings of the …. 1982.

10. Gething M, McCammon K. Expression of wild-type and mutant forms of influenza hemagglutinin: The role of folding in intracellular transport. Cell. 1986.

11. Harrison SC. Viral membrane fusion. Nat Struct Mol Biol. 2008;15(7):690-8.

12. Danieli T, Pelletier S, Henis Y, White J. Membrane fusion mediated by the influenza virus hemagglutinin requires the concerted action of at least three hemagglutinin trimers. Journal of Cell Biology. 1996.

13. Imai M. Membrane fusion by single influenza hemagglutinin trimers: Kinetic evidence from image analysis of hemagglutinin-reconstituted vesicles The Journal of biological chemistry. 2006;281(18):12729-35.

14. Dobay MP, Dobay A, Bantang J, Mendoza E. How many trimers? Modeling influenza virus fusion yields a minimum aggregate size of six trimers, three of which are fusogenic. Molecular bioSystems. 2011;7(10):2741-9. Epub 2011/07/09.

15. Belouzard S, Millet JK, Licitra BN, Whittaker GR. Mechanisms of coronavirus cell entry mediated by the viral spike protein. Viruses. 2012;4(12):1011-33.

16. Bosch BJ, van der Zee R, de Haan CA, Rottier PJ. The coronavirus spike protein is a class i virus fusion protein: Structural and functional characterization of the fusion core complex. Journal of virology. 2003;77(16):8801-11.

17. Madu IG, Roth SL, Belouzard S, Whittaker GR. Characterization of a highly conserved domain within the severe acute respiratory syndrome coronavirus spike

protein s2 domain with characteristics of a viral fusion peptide. Journal of virology. 2009;83(15):7411-21. Epub 2009/05/15.

18. Belouzard S, Chu VC, Whittaker GR. Activation of the sars coronavirus spike protein via sequential proteolytic cleavage at two distinct sites. Proceedings of the National Academy of Sciences of the United States of America. 2009;106(14):5871-6. Epub 2009/03/27.

19. Hoekstra D, Klappe K, De Boer T, Wilschut J. Characterization of the fusogenic properties of sendai virus: Kinetics of fusion with erythrocyte membranes. Biochemistry. 1985.

20. Wessels L, Elting M, Scimeca D, Weninger K. Rapid membrane fusion of individual virus particles with supported lipid bilayers. Biophysical Journal. 2007.

21. Floyd DL, Ragains JR, Skehel JJ, Harrison SC, van Oijen AM. Single-particle kinetics of influenza virus membrane fusion. Proceedings of the National Academy of Sciences of the United States of America. 2008;105(40):15382-7. Epub 2008/10/03.

22. Costello DA, Lee DW, Drewes J, Vasquez KA, Kisler K, Wiesner U, et al. Influenza virus-membrane fusion triggered by proton uncaging for single particle studies of fusion kinetics. Anal Chem. 2012;84(20):8480-9.

23. Costello DA, Millet JK, Hsia C-Y, Whittaker GR, Daniel S. Single particle assay of coronavirus membrane fusion with proteinaceous receptor-embedded supported bilayers. Biomaterials. 2013;34(32):7895-904.

24. Axelrod D. Total internal reflection fluorescence microscopy. Methods in cell biology. 2008.

25. Leenhouts JM, De Kruijff B. Membrane potential-driven translocation of a lipid-conjugated rhodamine. Biochimica et biophysica acta. 1995;1237(2):121-6. Epub 1995/07/26.

26. Melikyan G, Deriy B, Ok D, Cohen F. Voltage-dependent translocation of r18 and dii across lipid bilayers leads to fluorescence changes. Biophysical Journal. 1996.

27. Krumbiegel M, Herrmann A, Blumenthal R. Kinetics of the low ph-induced conformational changes and fusogenic activity of influenza hemagglutinin. Biophysical Journal. 1994.

28. Burnet F, Bull DR. Changes in influenza virus associated with adaptation to passage in chick embryos. Aust J Exp Biol Med Sci. 1943;21:55-69.

29. Robertson J, Cook P, Attwell A, Williams S. Replicative advantage in tissue-culture of egg adapted influenza-virus over tissue-culture derived virus - implications for vaccine manufacture. Vaccine. 1995;13(16):1583-8.

30. Oxford J, Newman R, Corcoran T, Bootman J, Major D, Yates P, et al. Direct isolation in eggs of influenza a (h1n1) and b viruses with haemagglutinins of different antigenic and amino acid composition. Journal of general virology. 1991;72(1):185-9.

31. Oxford JS, Corcoran T, Knott R, Bates J, Bartolomei O, Major D, et al. Serological studies with influenza a (h1n1) viruses cultivated in eggs or in a canine kidney cell line (mdck). Bulletin of the World Health Organization. 1987;65(2):181.

32. Noguchi H, Gompper G. Shape transitions of fluid vesicles and red blood cells in capillary flows. … of Sciences of the United States …. 2005.

33. Choi J, Hirota N, Terazima M. A ph-jump reaction studied by the transient grating method: Photodissociation of o-nitrobenzaldehyde. J Phys Chem A. 2001.

34. Trentham D. Properties and uses of photoreactive caged compounds. Annual review of biophysics and …. 1989.

35. Abbruzzetti S, Viappiani C, Small J. Kinetics of histidine deligation from the heme in guhcl-unfolded fe (iii) cytochrome c studied by a laser-induced ph-jump technique. J Am Chem …. 2001.

36. Abbruzzetti S, Sottini S, Viappiani C, Corrie JET. Acid-induced unfolding of myoglobin triggered by a laser ph jump method. Photochemical & Photobiological Sciences. 2006;5(6):621.

37. Saxena A, Udgaonkar J. Protein dynamics control proton transfer from bulk solvent to protein interior: A case study with a green fluorescent protein. Protein …. 2005.

38. Li W, Moore MJ, Vasilieva N, Sui J, Wong SK, Berne MA, et al. Angiotensin-converting enzyme 2 is a functional receptor for the sars coronavirus. Nature. 2003;426(6965):450-4.

39. Raj VS, Mou H, Smits SL, Dekkers DHW, Müller MA, Dijkman R, et al. Dipeptidyl peptidase 4 is a functional receptor for the emerging human coronavirus-emc. Nature. 2013;495(7440):251-4.

40. Ciancaglini P, Simão A, Bolean M, Millán J, Rigos C, Yoneda J, et al. Proteoliposomes in nanobiotechnology. Biophysical Reviews. 2012;4(1):67-81.

41. Dogterom M, Koenderink G. Cell-membrane mechanics: Vesicles in and tubes out. Nature Materials. 2011;10(8):561-2.

42. Robertson AM, Bird CC, Waddell AW, Currie AR. Morphological aspects of glucocorticoid-induced cell death in human lymphoblastoid cells. The Journal of pathology. 1978;126(3):181-7. Epub 1978/11/01.

43. Sezgin E, Kaiser H-J, Baumgart T, Schwille P, Simons K, Levental I. Elucidating membrane structure and protein behavior using giant plasma membrane vesicles. Nature protocols. 2012;7(6):1042-51.

44. Baumgart T, Hammond AT, Sengupta P, Hess ST, Holowka DA, Baird BA, et al. Large-scale fluid/fluid phase separation of proteins and lipids in giant plasma membrane vesicles. Proceedings of the National Academy of Sciences of the United States of America. 2007;104(9):3165-70.

45. Holowka D, Baird B. Structural studies on the membrane-bound immunoglobulin e-receptor complex .1. Characterization of large plasma-membrane vesicles from rat basophilic leukemia-cells and insertion of amphipathic fluorescent-probes. Biochemistry. 1983;22(14):3466-74.

46. Costello DA, Hsia C-Y, Millet JK, Porri T, Daniel S. Membrane fusion-competent virus-like proteoliposomes and proteinaceous supported bilayers made directly from cell plasma membranes. Langmuir. 2013;29(21):6409-19.

47. Wilschut J, Hoekstra D. Membrane fusion: CRC; 1991. 902 p.

48. Skehel J, Wiley D. Receptor binding and membrane fusion in virus entry: The influenza hemagglutinin. Annual review of biochemistry. 2000.

49. Russell R, Kerry P, Stevens D. Structure of influenza hemagglutinin in complex with an inhibitor of membrane fusion. Proceedings of the …. 2008.

50. Hoekstra D, De Boer T, Klappe K, Wilschut J. Fluorescence method for measuring the kinetics of fusion between biological membranes. Biochemistry. 1984;23(24):5675-81.

51. Chernomordik L, Leikina E, Frolov V. An early stage of membrane fusion mediated by the low ph conformation of influenza hemagglutinin depends upon membrane lipids. The Journal of cell …. 1997.

52. Polozov IV, Bezrukov L, Gawrisch K, Zimmerberg J. Progressive ordering with decreasing temperature of the phospholipids of influenza virus. Nature chemical biology. 2008;4(4):248-55.

53. Ramalho-Santos J, Nir S, Duzgunes N, Pato de Carvalho A, Pedroso de Lima MdC. A common mechanism for influenza virus fusion activity and inactivation. Biochemistry. 1993;32(11):2771-9.

54. Clague M, Schoch C, Blumenthal R. Delay time for influenza virus hemagglutinin-induced membrane fusion depends on hemagglutinin surface density. Journal of virology. 1991.

55. Alford D, Ellens H, Bentz J. Fusion of influenza virus with sialic acid-bearing target membranes. Biochemistry. 1994.

56. Rachakonda P, Veit M, Korte T, Ludwig K. The relevance of salt bridges for the stability of the influenza virus hemagglutinin. The FASEB Journal. 2007.

57. Bentz J, Ellens H, Alford D. An architecture for the fusion site of influenza hemagglutinin. FEBS Letters. 1990;276(1-2):1-5.

58. Stegmann T, White J, Helenius A. Intermediates in influenza induced membrane fusion. The EMBO journal. 1990;9(13):4231.

59. Chanturiya A, Chernomordik L. Flickering fusion pores comparable with initial exocytotic pores occur in protein-free phospholipid bilayers. Proceedings of the …. 1997.

60. Melikyan G, Niles W, Cohen F. Influenza virus hemagglutinin-induced cell-planar bilayer fusion: Quantitative dissection of fusion pore kinetics into stages. The Journal of general …. 1993.

61. Georgiou GN, Morrison IE, Cherry RJ. Digital fluorescence imaging of fusion of influenza virus with erythrocytes. FEBS letters. 1989;250(2):487-92.

62. Niles W. Fusion of influenza virions with a planar lipid membrane detected by video fluorescence microscopy. The Journal of general physiology. 1991.

63. Sarkar DP, Morris SJ, Eidelman O, Zimmerberg J, Blumenthal R. Initial stages of influenza hemagglutinin-induced cell fusion monitored simultaneously by two fluorescent events: Cytoplasmic continuity and lipid mixing. The Journal of cell biology. 1989;109(1):113-22.

64. Axelrod D, Burghardt TP, Thompson NL. Total internal reflection fluorescence. Annual review of biophysics and bioengineering. 1984;13(1):247-68.

65. McCray JA, Trentham DR. Properties and uses of photoreactive caged compounds. Annual review of biophysics and biophysical chemistry. 1989;18(1):239-70.

66. Dantzig J, Higuchi H. [18] studies of molecular motors using caged compounds. Methods in Enzymology. 1998.

67. Gambaryan AS, Robertson JS, Matrosovich MN. Effects of egg-adaptation on the receptor-binding properties of human influenza a and b viruses. Virology. 1999;258(2):232-9. Epub 1999/06/15.

68. Gambaryan AS, Tuzikov AB, Piskarev VE, Yamnikova SS, Lvov DK, Robertson JS, et al. Specification of receptor-binding phenotypes of influenza virus isolates from different hosts using synthetic sialylglycopolymers: Non-egg-adapted human h1 and h3 influenza a and influenza b viruses share a common high binding affinity for 6′-sialyl(n-acetyllactosamine). Virology. 1997;232(2):345-50.

69. Robertson JS, Bootman JS, Newman R, Oxford JS, Daniels RS, Webster RG, et al. Structural changes in the haemagglutinin which accompany egg adaptation of an influenza a(h1n1) virus. Virology. 1987;160(1):31-7.

70. Burleigh LM, Calder LJ, Skehel JJ, Steinhauer DA. Influenza a viruses with mutations in the m1 helix six domain display a wide variety of morphological phenotypes. Journal of virology. 2005;79(2):1262-70.

71. Kilbourne ED. Genetic studies of influenza viruses: I. Viral morphology and growth capacity as exchangeable genetic traits. Rapid in ovo adaptation of early passage asian strain isolates by combination with pr8. Journal of Experimental Medicine. 1960;111(3):387-406.

72. Vaheri A, Penttinen K, Väänänen P. Hemagglutination activity and morphology of influenza virus: Studies during adaptation to chick embryo. … Health: An International …. 1970.

73. Loyter A, Citovsky V, Blumenthal R. The use of fluorescence dequenching measurements to follow viral membrane fusion events. Methods of Biochemical Analysis, Volume 33. 1988:129-64.

74. Stöber W, Fink A, Bohn E. Controlled growth of monodisperse silica spheres in the micron size range. Journal of colloid and interface science. 1968;26(1):62-9.

75. Ow H, Larson DR, Srivastava M, Baird BA, Webb WW, Wiesner U. Bright and stable core-shell fluorescent silica nanoparticles. Nano letters. 2005;5(1):113-7.

76. Burns A, Sengupta P, Zedayko T, Baird B, Wiesner U. Core/shell fluorescent silica nanoparticles for chemical sensing: Towards single-particle laboratories. Small. 2006;2(6):723-6.

77. Hidalgo G, Burns A, Herz E, Hay AG, Houston PL, Wiesner U, et al. Functional tomographic fluorescence imaging of ph microenvironments in microbial biofilms by use of silica nanoparticle sensors. Applied and environmental microbiology. 2009;75(23):7426-35.

78. Brian A. Allogeneic stimulation of cytotoxic t cells by supported planar membranes. … of Sciences of the United States …. 1984.

79. Mao H, Yang T. Design and characterization of immobilized enzymes in microfluidic systems. Anal Chem. 2002.

80. Yang T, Jung S-y, Mao H, Cremer PS. Fabrication of phospholipid bilayer-coated microchannels for on-chip immunoassays. Analytical chemistry. 2001;73(2):165-9.

81. Floyd DL, Ragain JR, Skehel JJ, Harrison SC, van Oijen AM. Single-particle kinetics of influenza virus membrane fusion. Proc Natl Acad Sci. 2008;105:15382-7.

82. Li Y, Han X, Tamm LK. Thermodynamics of fusion peptide–membrane interactions †. Biochemistry. 2003;42(23):7245-51.

83. Larson DR, Ow H, Vishwasrao HD, Heikal AA, Wiesner U, Webb WW. Silica nanoparticle architecture determines radiative properties of encapsulated fluorophores. Chemistry of Materials. 2008;20(8):2677-84.

84. Haugland RP. The handbook: A guide to fluorescent probes and labeling technologies: Molecular Probes; 2005.

85. Markovic I, Leikina E, Zhukovsky M. Synchronized activation and refolding of influenza hemagglutinin in multimeric fusion machines. The Journal of cell …. 2001.

86. Blumenthal R, Sarkar D, Durell S. Dilation of the influenza hemagglutinin fusion pore revealed by the kinetics of individual cell-cell fusion events. Journal of Cell …. 1996.

87. Redfield DC, Richman D, Oxman M, Kronenberg L. Psoralen inactivation of influenza and herpes simplex viruses and of virus-infected cells. Infection and immunity. 1981;32(3):1216-26.

88. Janko K. Proton concentration jumps and generation of transmembrane ph-gradients by photolysis of 4-formyl-6-methoxy-3-nitrophenoxyacetic acid. Biochimica et Biophysica Acta (BBA)-Biomembranes. 1987.

89. Barth A. Characterization of a new caged proton capable of inducing large ph jumps. Biophysical Journal. 2002.

90. Brown EB, Shear JB, Adams SR, Tsien RY, Webb WW. Photolysis of caged calcium in femtoliter volumes using two-photon excitation. Biophysical journal. 1999;76(1):489-99.

91. Burgalossi A, Jung S, Meyer G, Jockusch WJ, Jahn O, Taschenberger H, et al. Snare protein recycling by αsnap and βsnap supports synaptic vesicle priming. Neuron. 2010;68(3):473-87.

92. Corti D, Voss J, Gamblin SJ, Codoni G, Macagno A, Jarrossay D, et al. A neutralizing antibody selected from plasma cells that binds to group 1 and group 2 influenza a hemagglutinins. Science. 2011;333(6044):850-6.

93. Ekiert DC, Friesen RHE, Bhabha G, Kwaks T, Jongeneelen M, Yu W, et al. A highly conserved neutralizing epitope on group 2 influenza a viruses. Science. 2011;333(6044):843-50.

94. Bolles M, Donaldson E, Baric R. Sars-cov and emergent coronaviruses: Viral determinants of interspecies transmission. Current opinion in virology. 2011;1(6):624-34.

95. 7(th) international symposium on enabling technologies for life sciences (etp). Rapid communications in mass spectrometry : RCM. 2013;27(22):2570-80.

96. Ivanovic T, Rozendaal R, Floyd DL, Popovic M, van Oijen AM, Harrison SC. Kinetics of proton transport into influenza virions by the viral m2 channel. PLoS One. 2012;7(3):e31566.

97. Matos PM, Marin M, Ahn B, Lam W, Santos NC, Melikyan GB. Anionic lipids are required for vesicular stomatitis virus g protein-mediated single particle fusion with supported lipid bilayers. The Journal of biological chemistry. 2013.

98. Tresnan DB, Levis R, Holmes KV. Feline aminopeptidase n serves as a receptor for feline, canine, porcine, and human coronaviruses in serogroup i. Journal of virology. 1996;70(12):8669-74.

99. Tusell SM, Schittone SA, Holmes KV. Mutational analysis of aminopeptidase n, a receptor for several group 1 coronaviruses, identifies key determinants of viral host range. Journal of virology. 2007;81(3):1261-73.

100. Yeager CL, Ashmun RA, Williams RK, Cardellichio CB, Shapiro LH, Look AT, et al. Human aminopeptidase n is a receptor for human coronavirus 229e. 1992.

101. Scott RE. Plasma membrane vesiculation: A new technique for isolation of plasma membranes. Science. 1976;194:743-5.

102. Bosch BJ, Bartelink W, Rottier PJ. Cathepsin l functionally cleaves the sars-cov class i fusion protein upstream of rather than adjacent to the fusion peptide. Journal of virology. 2008.

103. White JM, Delos SE, Brecher M, Schornberg K. Structures and mechanisms of viral membrane fusion proteins: Multiple variations on a common theme. Crit Rev Biochem Mol Biol. 2008;43(3):189-219.

104. Madu IG, Belouzard S, Whittaker GR. Sars-coronavirus spike s2 domain flanked by cysteine residues c822 and c833 is important for activation of membrane fusion. Virology. 2009.

105. Matsuyama S. Protease-mediated enhancement of severe acute respiratory syndrome coronavirus infection. Proceedings of the National Academy of Sciences of the United States of America. 2005;102(35):12543-7.

106. Regan AD, Shraybman R, Cohen RD, Whittaker GR. Differential role for low ph and cathepsin-mediated cleavage of the viral spike protein during entry of serotype ii feline coronaviruses. Veterinary microbiology. 2008;in press.

107. Sobo K, Chevallier J, Parton R, Gruenberg J. Diversity of raft-like domains in late endosomes. PLoS One. 2007.

108. Soumpasis D. Theoretical analysis of fluorescence photobleaching recovery experiments. Biophysical Journal. 1983.

109. Hohdatsu T, Izumiya Y, Yokoyama Y, Kida K, Koyama H. Differences in virus receptor for type i and type ii feline infectious peritonitis virus. Archives of virology. 1998;143(5):839-50.

110. Taylor A. Aminopeptidases: Structure and function. The FASEB Journal. 1993;7(2):290-8.

111. Reguera J, Santiago C, Mudgal G, Ordoño D, Enjuanes L, Casasnovas JM. Structural bases of coronavirus attachment to host aminopeptidase n and its inhibition by neutralizing antibodies. PLoS pathogens. 2012;8(8):e1002859.

112. Kominami E, Ueno T, Muno D, Katunuma N. The selective role of cathepsins b and d in the lysosomal degradation of endogenous and exogenous proteins. FEBS letters. 1991;287(1):189-92.

113. Huang IC, Bosch BJ, Li F, Li W, Lee KH, Ghiran S, et al. Sars coronavirus, but not human coronavirus nl63, utilizes cathepsin l to infect ace2-expressing cells. J Biol Chem. 2005;10:3198-203.

114. Simmons G, Gosalia DN, Rennekamp AJ, Reeves JD, Diamond SL, Bates P. Inhibitors of cathepsin l prevent severe acute respiratory syndrome coronavirus entry. Proc Natl Acad Sci U S A. 2005;102:11876-81.

115. Rawlings ND, Barrett AJ. [2] families of serine peptidases. Methods in enzymology. 1994;244:19-61.

116. Floyd DL, Harrison SC, van Oijen AM. Analysis of kinetic intermediates in single-particle dwell-time distributions. Biophysical Journal. 2010;99(2):360-6.

117. Castellana ET, Cremer PS. Solid supported lipid bilayers: From biophysical studies to sensor design. Surface Science Reports. 2006.

118. Takada A, Robison C, Goto H. A system for functional analysis of ebola virus glycoprotein. Proceedings of the …1997.

119. Matsuura Y, Tani H, Suzuki K, Kimura-Someya T, Suzuki R, Aizaki H, et al. Characterization of pseudotype vsv possessing hcv envelope proteins. Virology. 2001;286(2):263-75.

120. Claas EC, Osterhaus AD, van Beek R, De Jong JC, Rimmelzwaan GF, Senne DA, et al. Human influenza a h5n1 virus related to a highly pathogenic avian influenza virus. The Lancet. 1998;351(9101):472-7.

121. Dubavik A, Sezgin E, Lesnyak V, Gaponik N. Penetration of amphiphilic quantum dots through model and cellular plasma membranes - acs nano (acs publications). … nano. 2012.

122. Säälik P, Niinep A, Pae J, Hansen M, Lubenets D, Langel Ü, et al. Penetration without cells: Membrane translocation of cell-penetrating peptides in the model giant plasma membrane vesicles. Journal of Controlled Release. 2011;153(2):117-25.

123. Dodd CE, Johnson BRG, Jeuken LJC, Bugg TDH, Bushby RJ, Evans SD. Native e. Coli inner membrane incorporation in solid-supported lipid bilayer membranes. Biointerphases. 2008;3(2):FA59.

124. Hinterdorfer P, Baber G. Reconstitution of membrane fusion sites. A total internal reflection fluorescence microscopy study of influenza hemagglutinin-mediated membrane fusion. Journal of Biological Chemistry. 1994.

125. Takeda M, Leser G, Russell C. Influenza virus hemagglutinin concentrates in lipid raft microdomains for efficient viral fusion. Proceedings of the …. 2003;100(25):14607-9.

126. Koenig BW, Krueger S, Orts WJ, Majkrzak CF, Berk NF, Silverton JV, et al. Neutron reflectivity and atomic force microscopy studies of a lipid bilayer in water adsorbed to the surface of a silicon single crystal. Langmuir. 1996;12(5):1343-50.

127. Johnson SJ, Bayerl TM, McDermott DC, Adam GW, Rennie AR, Thomas RK, et al. Structure of an adsorbed dimyristoylphosphatidylcholine bilayer measured with specular reflection of neutrons. Biophysical Journal. 1991;59(2):289-94.

128. Gutberlet T, Steitz R, Fragneto G, Klösgen B. Phospholipid bilayer formation at a bare si surface: A time-resolved neutron reflectivity study. Journal of Physics: Condensed Matter. 2004;16(26):S2469.

129. Yamazaki V, Sirenko O, Schafer RJ, Groves JT. Lipid mobility and molecular binding in fluid lipid membranes. Journal of the American Chemical Society. 2005;127(9):2826-7.

130. Tanaka M, Sackmann E. Polymer-supported membranes as models of the cell surface. Nature. 2005;437:656-63.

131. Wagner ML, Tamm LK. Tethered polymer-supported planar lipid bilayers for reconstitution of integral membrane proteins: Silane-polyethyleneglycol-lipid as a cushion and covalent linker. Biophysical Journal. 2000;79(3):1400-14.

132. Albertorio F, Daniel S, Cremer PS. Supported lipopolymer membranes as nanoscale filters: Simultaneous protein recognition and size-selection assays. Journal of the American Chemical Society. 2006;128(22):7168-9.

133. Sackmann E, Tanaka M. Supported membranes on soft polymer cushions: Fabrication, characterization and applications. Trends in Biotechnology. 2000;18:58-64.

134. Elender G, Kuhner M, Sackmann E. Functionalisation of si/sio2 and glass surfaces with ultrathin dextran films and deposition of lipid bilayers. Biosens Bioelectron. 1996;11:565-77.

135. Molinari N-AM, Ortega-Sanchez IR, Messonnier ML, Thompson WW, Wortley PM, Weintraub E, et al. The annual impact of seasonal influenza in the us: Measuring disease burden and costs. Vaccine. 2007;25(27):5086-96.

136. Medina RA, García-Sastre A. Influenza a viruses: New research developments. Nature Reviews Microbiology. 2011;9(8):590-603.

137. Schäffr JR, Kawaoka Y, Bean WJ, Süss J, Senne D, Webster RG. Origin of the pandemic 1957 h2 influenza a virus and the persistence of its possible progenitors in the avian reservoir. Virology. 1993;194(2):781-8.

138. Xu R, McBride R, Paulson JC, Basler CF, Wilson IA. Structure, receptor binding, and antigenicity of influenza virus hemagglutinins from the 1957 h2n2 pandemic. Journal of virology. 2010;84(4):1715-21.

139. http://Www.Who.Int/influenza/human_animal_interface/en/.

140. Vijaykrishna D, Bahl J, Riley S, Duan L, Zhang JX, Chen H, et al. Evolutionary dynamics and emergence of panzootic h5n1 influenza viruses. PLoS pathogens. 2008;4(9):e1000161.

141. Herfst S, Schrauwen EJA, Linster M, Chutinimitkul S, de Wit E, Munster VJ, et al. Airborne transmission of influenza a/h5n1 virus between ferrets. Science. 2012;336(6088):1534-41.

142. Imai M, Watanabe T, Hatta M, Das SC, Ozawa M, Shinya K, et al. Experimental adaptation of an influenza h5 ha confers respiratory droplet transmission to a reassortant h5 ha/h1n1 virus in ferrets. Nature. 2012:1-11.

143. Whitt MA. Generation of vsv pseudotypes using recombinant δg-vsv for studies on virus entry, identification of entry inhibitors, and immune responses to vaccines. Journal of Virological Methods. 2010;169(2):365-74.

144. Weiss RA, Boettiger D, Murphy HM. Pseudotypes of avian sarcoma viruses with the envelope properties of vesicular stomatitis virus. Virology. 1977;76(2):808-25.

145. Huang AS, Palma EL, Hewlett N, ROIZMAN B. Pseudotype formation between enveloped rna and DNA viruses. 1974.

146. Zavada J, Rosenbergova M. Phenotypic mixing of vesicular stomatitis virus with fowl plague virus. Acta virologica. 1972;16(2):103.

147. Lawson ND, Stillman EA, Whitt MA, Rose JK. Recombinant vesicular stomatitis viruses from DNA. Proceedings of the National Academy of Sciences. 1995;92(10):4477-81.

148. Whelan S, Ball LA, Barr JN, Wertz G. Efficient recovery of infectious vesicular stomatitis virus entirely from cdna clones. Proceedings of the National Academy of Sciences. 1995;92(18):8388-92.

149. Wang W, Butler EN, Veguilla V, Vassell R, Thomas JT, Moos M, et al. Establishment of retroviral pseudotypes with influenza hemagglutinins from h1, h3, and h5 subtypes for sensitive and specific detection of neutralizing antibodies. Journal of Virological Methods. 2008;153(2):111-9.

150. Su C-Y, Wang S-Y, Shie J-J, Jeng K-S, Temperton NJ, Fang J-M, et al. In vitro evaluation of neuraminidase inhibitors using the neuraminidase-dependent release assay of hemagglutinin-pseudotyped viruses. Antiviral Research. 2008;79(3):199-205.

151. Temperton NJ, Hoschler K, Major D, Nicolson C, Manvell R, Hien VM, et al. A sensitive retroviral pseudotype assay for influenza h5n1−neutralizing antibodies. Influenza and other respiratory viruses. 2007;1(3):105-12.

152. Temperton N. Retroviral pseudotypes - els - temperton - wiley online library. eLS. 2009.

153. Sandrin V, Cosset F-L. Intracellular versus cell surface assembly of retroviral pseudotypes is determined by the cellular localization of the viral glycoprotein, its capacity to interact with gag, and the expression of the nef protein. Journal of Biological Chemistry. 2006;281(1):528-42.

154. Libersou S, Albertini AA, Ouldali M, Maury V, Maheu C, Raux H, et al. Distinct structural rearrangements of the vsv glycoprotein drive membrane fusion. J Cell Biol. 2010;191(1):199-210. Epub 2010/10/06.

155. Memish ZA, Mishra N, Olival KJ, Fagbo SF, Kapoor V, Epstein JH, et al. Middle east respiratory syndrome coronavirus in bats, saudi arabia. Emerging infectious diseases. 2013;19(11):1819.

156. Bermingham A, Chand M, Brown C, Aarons E, Tong C, Langrish C, et al. Severe respiratory illness caused by a novel coronavirus, in a patient transferred to the united kingdom from the middle east, september 2012. Euro Surveill. 2012;17.

157. Costello DA, Lee DW, Drewes J, Vasquez KA, Kisler K, Weisner U, et al. Influenza virus-membrane fusion triggered by proton uncaging for single particle studies of fusion kinetics. Analytical Chemistry. 2012;84:8480-9.

158. Libersou S, Albertini AAV, Ouldali M, Maury V, Maheu C, Raux H, et al. Distinct structural rearrangements of the vsv glycoprotein drive membrane fusion. The Journal of cell biology. 2010;191(1):199-210.

159. Hess ST, Kumar M, Verma A, Farrington J, Kenworthy A, Zimmerberg J. Quantitative electron microscopy and fluorescence spectroscopy of the membrane distribution of influenza hemagglutinin. The Journal of cell biology. 2005;169(6):965-76.

160. Suzuki Y, Nagao Y, Kato H, Matsumoto M, Nerome K, Nakajima K, et al. Human influenza a virus hemagglutinin distinguishes sialyloligosaccharides in membrane-associated gangliosides as its receptor which mediates the adsorption and fusion processes of virus infection. Specificity for oligosaccharides and sialic acids and the sequence to which sialic acid is attached. The Journal of biological chemistry. 1986;261(36):17057-61.

161. Chan DC, Kim PS. Hiv entry and its inhibition. Cell. 1998;93(5):681-4.

162. Wyatt R, Sodroski J. The hiv-1 envelope glycoproteins: Fusogens, antigens, and immunogens. Science. 1998;280(5371):1884-8.

163. Brian AA, McConnell HM. Allogeneic stimulation of cytotoxic t cells by supported planar membranes. Proc Natl Acad Sci. 1984;81:6159-63.

164. Mao H, Yang T, Cremer PS. Design and characterization of immobilized enzymes in microfluidic systems. Anal Chem. 2002;74:379-85.

165. Yang T, Jung S-Y, Mao H, Cremer PS. Fabrication of phospholipid bilayer-coated microchannels for on-chip immunoassays. Anal Chem. 2001;73:165-9.

166. Soumpasis DM. Theoretical analysis of fluorescence photobleaching recovery experiments. Biophys J. 1983;41:95-7.

167. Floyd DL, Harrison SC, van Oijen AM. Analysis of kinetic intermediates in single-particle dwell-time distributions. Biophys J. 2010;99:360-6.

168. Howland MC, Szmodis AW, Sanii B, Parikh AN. Characterization of physical properties of supported phospholipid membranes using imaging ellipsometry at optical wavelengths. Biophysical Journal. 2007;92(4):1306-17.

169. Nielsen MMB, Simonsen AC. Imaging ellipsometry of spin-coated membranes: Mapping of multilamellar films, hydrated membranes, and fluid domains. Langmuir. 2013;29(5):1525-32.

Appendix A

Materials. The following lipids were used in these experiments: 1, 2 dioleoyl-*sn*-glycero-3-phosphocholine (DOPC), 1-oleoyl-2-palmitoyl-sn-glycero-3-phosphocholine (POPC), cholesterol, and total ganglioside extract (bovine, brain). These were obtained from Avanti Polar Lipids (Alabaster, AL). The fluorescently labeled lipid, Oregon green 488 DHPE (Molecular Probes, Eugene, OR), was used to conduct fluorescence recovery after photobleaching experiments and to detect the pH drop in acidic flow experiments. Biotechnology grade chloroform and methanol for preparation of vesicles were purchased from Sigma-Aldrich. Polycarbonate filters (Whatman Nucleopore) with pore diameters of 100 nm and 50 nm were used in the preparation of vesicles. Glass coverslips (25 mm x 25 mm; No. 1.5) from VWR were used as supports for the bilayers. Sulfuric acid and hydrogen peroxide used to clean the glass coverslips were purchased from VWR. Polydimethylsiloxane (PDMS; Sylgard 184) used to fabricate microfluidic flow cell devices was purchased from Robert McKeown Company (Branchburg, NJ). Sodium chloride salt (NaCl) and (2-(N-Morpholino) ethanesulfonic acid sodium salt (MES) used to make buffers were purchased from VWR. *o*-nitrobenzaldehdye (*o*-NBA) was purchased from Sigma

Aldrich. Influenza X:31 (H3N2) was purchased from Charles River Labs (Wilmington, MA). Octadecyl Rhodamine B chloride (R18) and Sulforhodamine B (SRB) used to label the virus were purchased from Molecular Probes (Eugene, OR). G-25 spin columns used in virus labeling and purification were purchased from GE Healthcare. Triton-X (J.T. Baker) detergent used in virus labeling optimization was purchased from VWR.

Rhodamine 110 chloride and 1-octadecanol were purchased from Sigma Aldrich for the synthesis of the Rhodamine 110 octadecyl ester (R110C18). The concentrated sulfuric acid used to start the synthesis reaction was purchased from VWR and the triethylamine used to stop the reaction was purchased from Acros Organics. Silica Gel 60 (63-200 μm particle diameter) was purchased from EMD and Neutral Alumina (50-200 μm particle diameter) was purchased from Dynamic Adsorbents, Inc.) In order to purify the dye product using column chromatography. Isopropanol, chloroform, and methanol were all purchased from VWR to make the elution solvents.

For the Oregon Green C dot preparation, Oregon Green 488 maleimide was purchased from Molecular Probes (Eugene, OR). Silane for conjugation, 3-mercaptopropyltrimethoxy silane (MPTMS), was purchased from Gelest (Morrisville, PA). Tetraethyl orthosilicate (TEOS) and 2 M ammonia in ethanol were purchased from Sigma Aldrich. Particles were dialyzed using a 3500 molecular weight cut-off (MWCO) SnakeSkin Dialysis Tubing purchased from Thermo Scientific (Rockford, IL). The C dots were densified using a 20 mL reaction vial with a Teflon faced septa lid from Chemglass (Vineland, NJ).

Buffer Preparation. Sodium chloride salt (NaCl) and (2-(N-Morpholino) ethanesulfonic acid sodium salt (MES), citric acid, *o*-NBA, and *o*-nitrosobenzoic anion (*o*-NSA^-) were used to make buffer solutions according to the formulations in Table S1. *o*-NSA^- is the post-irradiated product of the photoisomerization reaction of *o*-NBA. The pHs of each solution are indicated within the text where appropriate.

Table A1. Buffer Formulations

	NaCl (mM)	**MES (mM)**	**Citric Acid (mM)**	***o*-NBA (mM)**	***o*-NSA^- (mM)**
Buffer A	150	1.5	5	0	0
Buffer B	150	1.25	0	10, 12, 14	0
Buffer C	0	1.25	0	0	0
Buffer D	150	1.25	0	0	12
Buffer E	150	1.25	0	0	0

Note that for buffer B, the concentration of *o*-NBA was 10, 12, or 14 mM, with all other components constant. Varying *o*-NBA concentration allowed us to control the post-irradiated pH, as described in the text. Various concentrations of *o*-NBA buffer could be made by dissolving the appropriate amount of *o*-NBA in 50 ml of Buffer B initially at pH 7.0. For example, to create a 12 mM solution (used here for some of the

proton uncaging experiments), 0.0906 g of *o*-NBA was required. The solution was heated to 98ºC and then cooled gradually to room temperature. Solutions were prepared in a darkened room to prevent any stray light from irradiating the solution, partially uncaging protons, and consequently dropping the pH of the buffer solution. The solution was stored at room temperature in the dark and used within three days of preparation. The pH was checked prior to use to ensure that no degradation had taken place.

Surface Preparation. Glass microscope coverslips were cleaned in piranha solution (70% sulfuric acid, 30% hydrogen peroxide). Slides were immersed in 150 ml of piranha solution for ten minutes. The slides were subsequently rinsed for 30 minutes with copious amounts of deionized water with a minimum resistance of 18.2 MΩ·cm obtained from a Siemens Purelab Ultra water purification system. Clean slides were stored under deionized water, then dried with a stream of ultra pure nitrogen gas prior to use.

Microfluidic Device Fabrication. Microfluidic devices for the fusion experiments were fabricated using soft lithography. The microchannel pattern was designed using the CAD software program L-Edit (Tanner EDA) and a master of the flow pattern was made on a silicon wafer at Cornell Nanoscale Science and Technology Facility (CNF). Each microfluidic device contained six channels. The dimensions of each channel are 1 mm wide by 70 μm deep with a total length of the channel of 1.5 cm. The spacing between the centers of each channel is 1 mm. The silicon wafer was coated with P-20 primer in a spin coater, followed by SPR220 (Megaposit) photo-resist. The wafer was baked for 90 seconds at 115ºC and then exposed to UV light for 7.5 seconds in an

ABM contact aligner to pattern the wafer with the flow cell design. Following this step, the wafer was baked again for 90 seconds at 115ºC and then developed for 60 seconds in a Hamatech-Steag Wafer Processor. The pattern was then etched into the wafer using a Unaxis 770 Deep Si Etcher. The depth of the channel was determined using a Tencor P10 Profilometer.

Microfluidic devices were formed using PDMS in a molding process. To facilitate the release of the cured PDMS after molding on the etched silicon master, the master slide was first coated with Sigmacote (Sigma). A 10:1 (elastomer/crosslinker) mixture of Sylgard 184 was mixed and then degassed before pouring on the silicon master slide etched with the flow cell pattern. The PDMS was then baked for 3 hours at 80ºC. After baking, PDMS microfluidic devices were peeled off of the wafer, and inlet and exit ports were punched in each channel of the device. Both the clean glass coverslip and PDMS mold were treated with oxygen plasma using a Harrick Plasma Cleaner (Model # PDC-32G, Ithaca, NY) at a pressure of 750 μm on the high setting for 25 seconds. Gently pressing the surfaces together resulted in a tight bond between the glass and PDMS and formed the four walls of the microfluidic channel.

Lipid Vesicle Preparation. The following lipids were used in these experiments: 1, 2 dioleoyl-*sn*-glycero-3-phosphocholine (DOPC), 1-oleoyl-2-palmitoyl-*sn*-glycero-3-phosphocholine (POPC), cholesterol, and total ganglioside extract (bovine, brain). Lipid vesicles were prepared using a molar ratio of 4:4:2:0.5 of DOPC, POPC, cholesterol and total ganglioside extract. For diffusion measurements and acidic flow experiments, 0.01 mol% Oregon Green DHPE was also added to the bilayer formulation. Cholesterol was dissolved in biotechnology grade chloroform and total

ganglioside extract was dissolved in a 2:1 mixture of biotechnology grade chloroform/methanol. Lipids were thoroughly mixed in a scintillation vial and then the solvent was removed under a stream of high purity nitrogen gas. To ensure all solvent was removed, the vial was placed in a desiccator under vacuum for an additional 2.5 to 3 hours. 6 ml of Buffer A at pH 7.0 was then added to the dried lipid film and resuspended gently in a sonication bath (Model # BD2500A-DTH, VWR) for twenty minutes on the lowest setting. The final lipid concentration was approximately 8.3 mg/ml. Liposomes were then extruded twice through a polycarbonate filter with pore size 100 nm, and five times through a filter with a pore size of 50 nm.

Lipid Vesicle Characterization: Size and Zeta Potential. The average liposome diameter was determined by dynamic light scattering using a Malvern Zetasizer Nano (Worcestershire, UK) and ranged between 90 and 100 nm in diameter. To ensure that the cage compounds did not interfere with the surface charge of the bilayer and possibly alter the electrostatic interactions between the virus and supported bilayer, we measured the zeta potential of the vesicles and virus under various conditions (Table S2). We found that there is little difference in the zeta potentials of either the virus or the vesicle in the presence of *o*-NBA or its post-irradiated analog, *o*-NSA^-, compared to the base case in plain buffer conducted at the same pH.

Table A2. Zeta Potential Measurements of Lipid Vesicles and Virus in Various Buffer Environments

Vesicle/Environment	pH	Zeta Potential (mV)

Vesicles in buffer E	7	-10.8 ± 0.3
Vesicle in Buffer E	5.2	-10.2 ± 0.5
Vesicles + *o*-NBA (12 mM) in buffer B	7.0	-12.4 ± 1.1
Vesicles + *o*-NSA^- (12 mM) in buffer D	5.2	-11.8 ± 0.4
Virus/Environment	**pH**	**Zeta Potential (mV)**
Virus in buffer A	7.0	-11.2 ± 1.0
Virus in buffer A	5.2	-7.2 ± 0.2
Virus + *o*-NBA in buffer B	7.0	-12.8 ± 0.7
Virus + *o*-NSA^- in buffer D	5.2	-7.8 ± 0.5

Lipid vesicles were subsequently used to form supported bilayers inside the microfluidic device via vesicle fusion(163-165). Lipid diffusion and bilayer quality was then assessed by fluorescence recovery after photobleaching.

Supported Bilayer Characterization: Diffusion Measurements.

Integrity of bilayers and diffusion of the lipids within it was examined by fluorescence recovery after photobleaching (FRAP). To measure the diffusion coefficient and mobile fraction of the lipid bilayer, liposomes of the same composition used in experiments were prepared with 0.01 mol% Oregon Green DHPE (Molecular Probes, Eugene, OR). A 10% dilution of liposomes in buffer A was incubated in a PDMS well attached to a piranha cleaned slide. Diffusion measurements were taken of the aforementioned liposomes under three different conditions:

1) In the presence of buffer A at pH 7 (control case).
2) In the presence of 12 mM *o*-NBA at pH 7.
3) In the presence of 12 mM *o*-NSA^-, with the pH of this solution adjusted to pH 7 using sodium hydroxide.

Liposomes were allowed to incubate for 10 minutes in each solution, before being rinsed with buffer A at pH 7.0 for one minute. The bilayer was scratched with a dissection tool to remove a thin line of bilayer to aid in focusing on the plane of the bilayer on the microscope. Following the scratching step, the bilayer was rinsed again for one minute with buffer A to wash out any lipids removed by scratching. A 20 μm diameter spot in the supported lipid bilayer was bleached with a 4.7 mW 488 nm krypton/argon laser for 200 ms. The recovery of the intensity of the photobleached spot was recorded for 15 minutes. The fluorescence intensity of the bleached spot was determined after background subtraction and normalization for each image. The recovery data was fit using a Bessel function following the method of Soumpasis(166). The diffusion coefficient was then calculated using the following equation: $D = \frac{w^2}{4t_{1/2}}$, where *w* is the full width at half-maximum of the Gaussian profile of the focused beam. The average diffusion coefficient for the samples under the aforementioned buffer conditions are shown in Table S3. Neither *o*-NBA nor its post-irradiated analog, *o*-NSA^-, affects the diffusion coefficient of the supported lipid bilayer. These diffusion coefficients are in line with numerous reports of lipid diffusion in supported bilayers and also indicate good formation and integrity of the supported bilayers used here.

Table A3. Lipid Diffusion Coefficients and Mobile Fractions in Supported Bilayers under Various Buffer Conditions			
Bathing Solution	**Control: Buffer A, pH 7.0**	**With *o*-NBA at pH 7.0**	**With *o*-NSA$^-$ at pH 7.0**
Diffusion Coefficient ($\mu m^2/s$)	1.76 ± 0.23	1.73 ± 0.46	1.95 ± 0.27
Mobile Fraction	0.97 ± 0.11	1.03 ± 0.05	0.94 ± 0.18

Virus Membrane Labeling and Purification. In these studies, two virus membrane labels were used. For experiments examining just the hemifusion step, R18, a red-emitting fluorophore, was used. In this case, 5 μL of virus and 0.1 μL of R18 were added to 250 μL of buffer A. The mixture was sonicated gently in a water bath for one hour. Free R18, which did not insert into the viral membrane, was removed from labeled virus using a G-25 spin column for two minutes in a centrifuge (Eppendorf, Centrifuge 5451C, Hauppauge, NY) at rate of 3x1000 min^{-1}. The supernatant containing the purified virus was diluted with 1.8 ml of buffer A and gently vortexed to mix the virus and buffer.

The optimal incubation time for R18 labeling of influenza X:31 to achieve the best fluorescence dequenching signals was achieved by varying both the sonication time and R18 concentration and then quantifying the extent of dequenching in a fluorimeter (PTI, Birmingham, NJ). Triton-X detergent was used to solubilize the membranes,

thus diluting the fluorophore and leading to full fluorescence dequenching. From these results, labeling-to-dequenching was optimized.

In experiments where both the membrane and internal viral contents were labeled, the membrane dye was switched to R110C18, a green-emitting fluorophore, so that a red-emitting fluorophore (SRB) could be used to label the internal contents. The same general labeling procedure described for R18 was used for labeling the viral membranes with R110C18. R110C18 was synthesized following the procedure in Floyd et al(81), and described here only briefly. In a reaction vial, 7.5 g of 1-octadecanol and 30 mg of Rhodamine 110 Chloride were mixed together at 80°C. Once the octadecanol melted, 100 μl of concentrated sulfuric acid was added to catalyze the dye conjugation reaction. The reaction was run for 48 hours at 80°C and halted by adding 600 μl of triethylamine. The reaction mixture was cooled to room temperature, dissolved in 200 mL of diethyl ether, and then filtered, leaving behind a solid product. A chromatography column was prepared so that there was a 1 cm-high silica slurry at the bottom with a 10 cm-high alumina slurry above, both soaked in 10% isopropanol in chloroform. The product was loaded on the column and eluted with 100 mL each of 10%, 20%, 30%, and 40% isopropanol in chloroform, in that order, to remove excess octadecanol. The R110C18 product was eluted using a 10% methanol/20% isopropanol/70% chloroform solution. Fluorescent volume fractions were dried under nitrogen and then vacuum desiccated, leaving behind R110C18 powder that was subsequently used to label viruses.

Dual-Color Virus Labeling and Purification. For dual-color virus fusion experiments, influenza X:31 was labeled with SRB and R110C18. First, 10 μL of 20 mM SRB dissolved in buffer A was added to 5 μL of influenza X:31. 250 μL of buffer A was added to the virus/SRB mixture and allowed to incubate for 16-20 hours. Excess SRB was removed from labeled virus using a G-25 spin column for two minutes in a centrifuge at rate of 3x1000 min^{-1}. Free R18, which did not insert into the viral membrane, was removed from labeled virus using a G-25 spin column for two minutes in a centrifuge at rate of 3x1000 min^{-1}. Next, 3 μL of 2 mM R110C18 was added to the supernatant collected from the G-25 spin column and placed in a gentle sonicating bath for 90 minutes. Post sonication, the mixture was filtered through another G-25 spin column, as described previously to remove excess dye. The supernatant was diluted in 1.4 ml of buffer A.

Uniformity of Uncaging Across the Field-of-View. Uniformity of illumination and uncaging across the field of view (~ 100 μm^2) by the laser is confirmed by the random mapping of the fusion events shown in Figure S1.

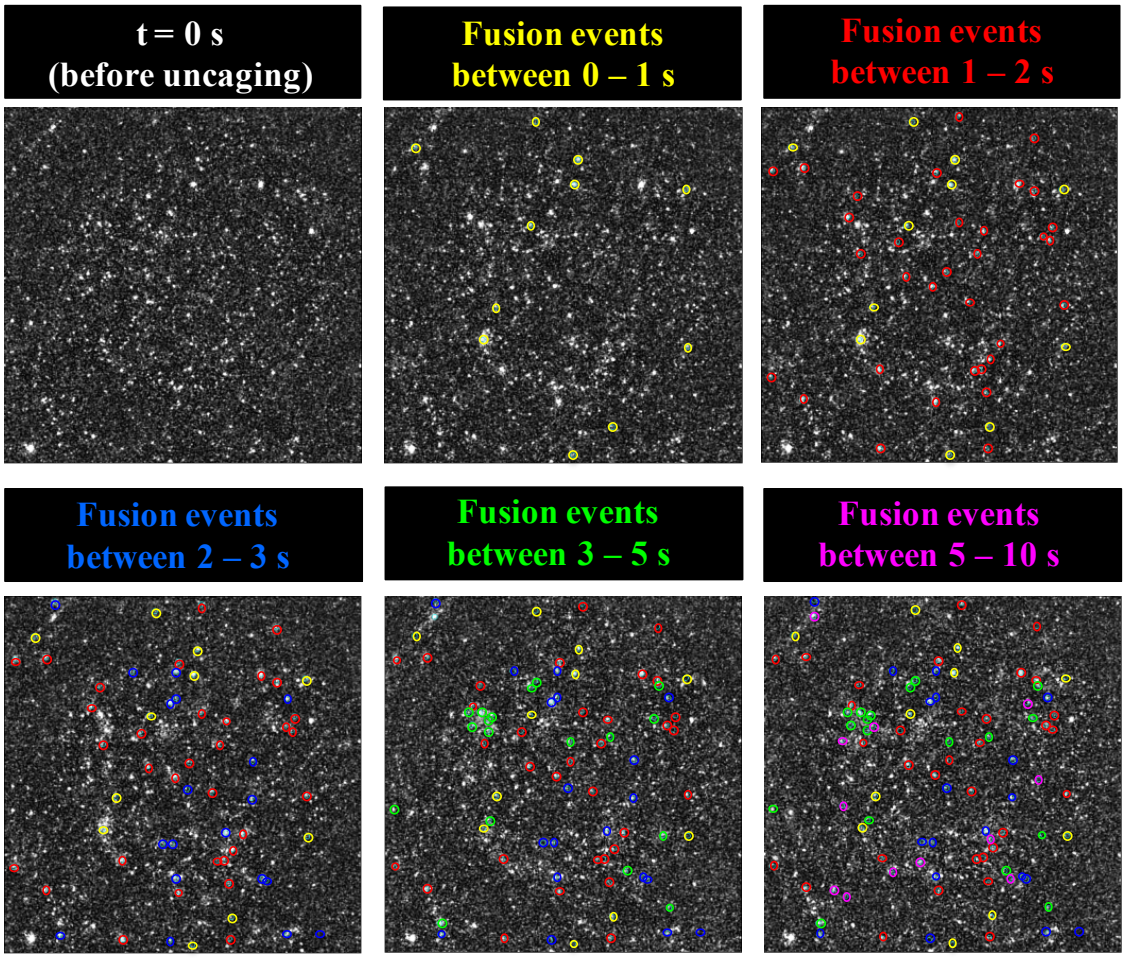

Figure A1. A map of the virus fusion events in time triggered by uncaging. Each image is the same t = 0 image marked with the time interval in which dequenching began for those viruses. Each dequenching event during that interval is marked with a colored circle to map out the events across the field of view. The events are randomly distributed, indicating that there is uniformity in the uncaging across the field of view.

Temperature change after UV pulse. To ensure that the UV laser pulse does not significantly change the temperature in the ROI at the time of fusion, the temperature pre- and post-UV pulse was checked using a thermocouple placed on a coverslip in the

path of the UV beam on the 100x microscope objective. The temperature pre-UV pulse was 23.4ºC and immediately post-UV pulse the temperature increased slightly to 24.5ºC but almost immediately returned to ambient temperature.

Marking the Onset of Hemifusion by Fluorescence Dequenching. In this assay, membrane hemifusion events are detected by the dequenching of a fluorescent membrane probe (R18 or R110C18) located in the viral membrane. In this example, influenza X:31 was incubated with R18, until enough R18 partitioned into the viral membrane so that neighboring fluorophores quench each other, as described in the virus labeling procedure above. During fusion, when the outer monolayers of the viral and supported membranes mix, the fluorophore gets diluted and a sharp increase (spike) in fluorescence (dequenching) is observed as shown in Figure S2. Following the 'spike' in fluorescence, the fluorescent probe diffuses away from the hemifusion site, thus indicating that these are true fusion events and the fluorescence increase, which marks the onset of hemifusion, and is not a result of a viral particle changing its position in the evanescent field.

Figure S2 shows a series of images of a single virus particle following the acidification at time = 0 by acidic buffer exchange method. The initial image (t = 0), onset of dequenching (t = 25 s), and after diffusion of R18 away from the fusion site (t = 49 s) are labeled on the plot with color-coded arrows. The time of hemifusion is defined by the timestamp of the image where the fluorescence begins to rapidly increase.

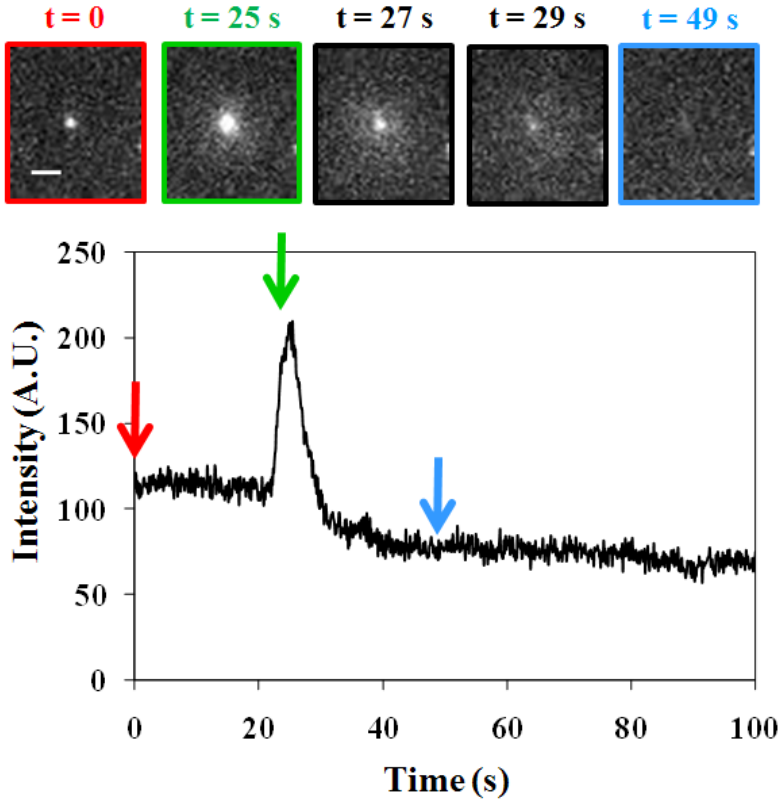

Figure A2. Virus particle dequenching trace. (Top) Images of a virus particle dequenching after hemifusion with the supported bilayer. The scale bar in image, t = 0, is 1 μm. (Bottom) A trace of the fluorescence level surrounding the fusion site in time. Images at t = 0, 25 s, and 49 s, are labeled on the plot with color-coded arrows.

Virus Diameter Measurements. The average virus diameter was determined by dynamic light scattering using a Malvern Zetasizer Nano (Worcestershire, UK). The average diameter of X:31 and Udorn was 140nm and 155nm respectively. Brisbane contained two populations with peaks at 145nm and 760nm.

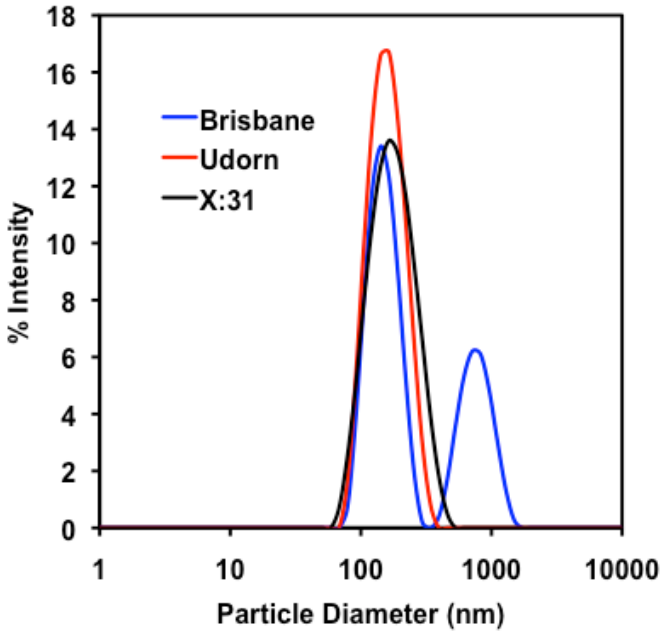

Figure A3. Dynamic light scattering measurements of influenza virion diameter

Image Processing. The images acquired during the fusion assays were analyzed using both ImageJ (NIH) and MATLAB (Mathworks). Fusing particles were manually selected in ImageJ and the fluorescence intensity in a 3x3 pixel region around each particle was collected as a function of time. In videos where background noise was high due to a large amount of fusion events, a rolling ball background subtraction algorithm was applied to all of the images to remove excess background noise as the

fluorophores diffused into the membrane after hemifusion. The rolling ball algorithm determines the local background for every pixel by averaging over a large circular region around the pixel. This background value is then subtracted from the original image. The fluorescence trajectories for the particles were then imported to MATLAB (Mathworks) for further analysis. A code written in MATLAB determined the onset time of the dequenching 'spike' for each particle by finding the time of the maximum intensity in each particle trajectory.

Kinetic Analysis. The lag time for each hemifusing virus was recorded and a cumulative distribution curve was generated by plotting the time of the onset of hemifusion as a function of the frequency of events. The resulting curve (like those in Figure 3 in the main text) is then fit with a cumulative gamma distribution (equation S8) to estimate the kinetic parameters:

$$p_H = \int_0^t \frac{k_H^N t^{N-1}}{\Gamma(N)} e^{-k_H t}$$

(S8)

Where k_H is the hemifusion rate constant, t is time, and N is an additional fit parameter, often correlated to the number of steps or the number of HA trimers that must act concertedly to initiate fusion(81). A gamma distribution is commonly used to fit kinetics of viral fusion because individual fusion events occur independently of each other. The gamma distribution describes a multistep reaction scheme, where each step is a stochastic Poisson process with a rate constant k. For N kinetic steps, the overall rate constant is defined as k_H, the hemifusion rate constant. The sharp rise and decay of hemifusion events is indicative of multiple intermediate kinetic steps that

take place between acidification and hemifusion. An exponential decay of observed events would suggest that hemifusion is a single step process; however, previous work suggests that kinetic steps involved in influenza hemifusion occur in parallel and that N may represent the number of HA trimers required to initiate hemifusion(81). The probability distribution was fit to our data using a non-linear least squares fitting algorithm.

The accuracy with which N and k_H can be determined depends on both the number of experimental observations and the number of steps in the process(167). To accurately estimate N from a gamma distribution a minimum number of a fusion events must occur for statistical significance. For example, to distinguish a 2-step process from a 3-step process i.e. $N = 2$ from $N = 3$, a minimum of 50 fusion events must be observed in a single experiment. The number of fusion events that occurred during each experiment reported here varied from 159 to 228 and 129-187 for fusion initiated using proton uncaging and acid flow respectively.

Control Experiments. This section summarizes control experiments conducted to ensure that *o*-NBA and *o*-NSA^- did not have adverse effects on the fusion kinetics of influenza. The data are summarized in Figure A4. In this figure, the black circles are the acid flow data obtained by buffer exchange experiments at various pH's (buffer A) as indicated on the plots. Buffer exchange rates for all control experiments were 100 μl/min. Both the k_H and N data for acidic flow exchange match remarkably well with the data in the literature(81).

To first ensure that the UV laser itself did not adversely affect the virus's ability to fuse, we ran a control where the virus was bound to the bilayer, then irradiated with

UV light for 200 ms, and then fusion initiated by acidic buffer exchange to pH 5.1 (green square). The data falls within the acid flow control data.

Next, we checked if the presence of *o*-NBA affected fusion by incubating the virus in this solution at pH 7.0 for 30 minutes, followed by acidic buffer exchange to pH 4.7 (blue square) and also find that the data falls within the acid flow controls.

Finally, we checked if the post-irradiated product of *o*-NBA, *o*-NSA^-, impacted virus fusion in two ways. For both of these experiments, a 12 mM solution of o-NBA was irradiated with UV light uniformly to maximally uncage all *o*-NBA and create *o*-NSA^- in its place. For the first experiment, a portion of this solution was brought back to pH 7.0 with sodium hydroxide and then incubated with the virus for 30 minutes. Following this incubation, acidic buffer exchange at pH 4.7 was used to initiate fusion (purple square). The data falls within the acidic flow controls. For the second experiment, the pH of the remaining solution was measured with a pH probe and found to be ~ 4. This acidic solution was then exchanged with the existing pH 7.0 solution in the device to initiate fusion (pink square). This data also falls within the trends of acidic flow controls.

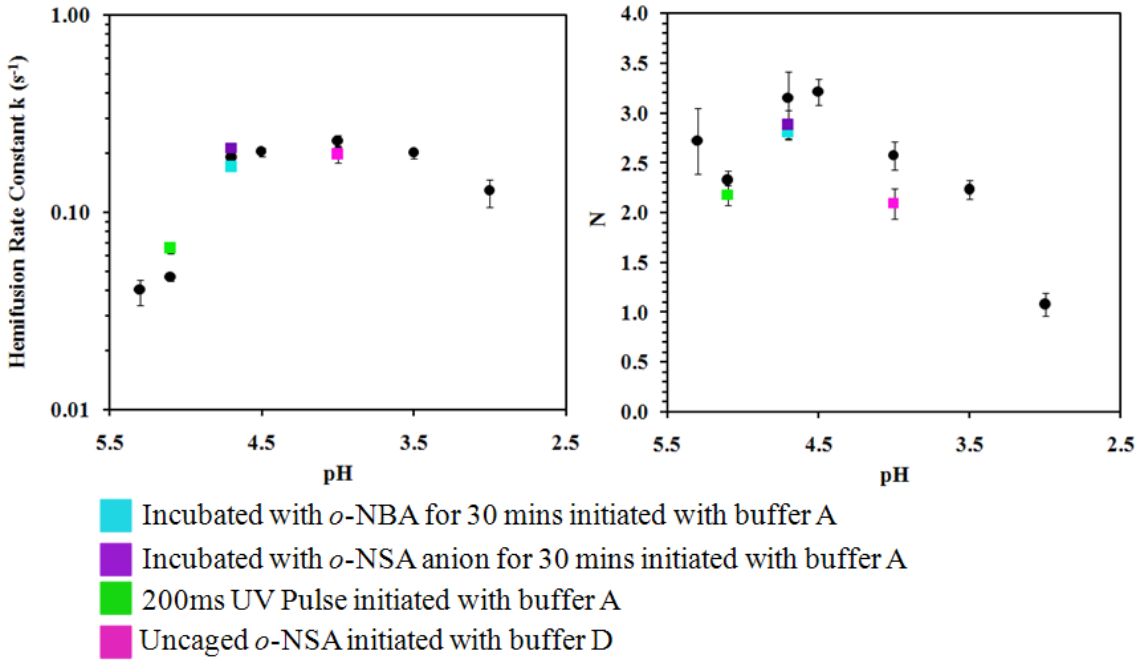

Figure A4. Summary of control experiments showing that the *o*-NBA and *o*-NSA$^-$ do not adversely affect the fusion kinetics of the virus.

Appendix B

1. Preparation of glass surfaces for supported bilayers

Glass microscope coverslips (25 mm x 25 mm; No. 1.5) from VWR were cleaned in piranha solution consisting of 70% sulfuric acid and 30% hydrogen peroxide. Slides were immersed in 150 ml of piranha solution for 10 minutes then rinsed for 30 minutes with copious amounts of deionized water with a minimum resistance of 18.2 MΩ·cm obtained from a Siemens Purelab Ultra water purification system. Clean slides were stored under deionized water and dried with a stream of ultra-pure nitrogen gas prior to use. For bilayer formation, glass surfaces were used either with PDMS wells or microfluidic devices.

2. Fabrication of PDMS wells

To form the PDMS wells, a thin sheet of PDMS (~ 5 mm) was made in a Petri dish using 10:1 elastomer/crosslinker mixture of Sylgard 184 (Robert McKeown Company; Branchburg, NJ). The PDMS was baked for 3 hours at 80ºC, cut into small squares approximately the same size as a coverslip, and a hole punched through each square to form the wells. PDMS squares were then attached to a clean glass coverslips, which formed the bottom of the wells. The approximate volume of a well was 100 µl.

3. Fabrication of microfluidic devices

Microfluidic devices for the fusion experiments were fabricated using soft lithography. The microchannel pattern was designed using the CAD software program L-Edit (Tanner EDA) and a master of the flow pattern was made on a silicon wafer at

Cornell Nanoscale Science and Technology Facility (CNF). Each microfluidic device contained six channels. The dimensions of each channel are 1 mm wide by 70 μm deep with a total length of the channel of 1.5 cm. The spacing between the centers of each channel is 1 mm. The silicon wafer was coated with P-20 primer in a spin coater, followed by SPR220 (Megaposit) photo-resist. The wafer was baked for 90 seconds at 115ºC and then exposed to UV light for 7.5 seconds in an ABM contact aligner to pattern the wafer with the flow cell design. Following this step, the wafer was baked again for 90 seconds at 115ºC and then developed for 60 seconds in a Hamatech-Steag Wafer Processor. The pattern was then etched into the wafer using a Unaxis 770 Deep Si Etcher. The depth of the channel was determined using a Tencor P10 Profilometer.

Microfluidic devices were formed using PDMS in a molding process. To facilitate the release of the cured PDMS after molding on the etched silicon master, the master slide was first coated with Sigmacote (Sigma). A 10:1 (elastomer/crosslinker) mixture of Sylgard 184 was mixed and then degassed before pouring on the silicon master slide etched with the flow cell pattern. The PDMS was then baked for 3 hours at 80ºC. After baking, PDMS microfluidic devices were peeled off of the wafer, and inlet and exit ports were punched in each channel of the device. Both the clean glass coverslip and PDMS mold were treated with oxygen plasma using a Harrick Plasma Cleaner (Model # PDC-32G; Ithaca, NY) at a pressure of 750 μm on the high setting for 25 seconds. Gently pressing the surfaces together resulted in a tight bond between the glass and PDMS and formed the four walls of the microfluidic channel.

4. Liposome formation procedure

To form these liposome preparations, appropriate amounts of each component

were mixed in biotechnology grade chloroform in a scintillation vial. For formulations containing sphingomyelin, this component was first dissolved in a 4:1 mixture of chloroform: methanol then added to the mixture. The bulk solvent was removed from the vial under a stream of high purity nitrogen gas and then placed in a desiccator under vacuum overnight to ensure complete evaporation of all solvent. Phosphate-buffered saline at pH 7.4 was added to the dried lipid film and gently resuspended in a sonication bath (Model # BD2500A-DTH; VWR) for 20 minutes on the lowest setting. The final lipid concentration was approximately 2 mg/ml. Liposomes were then extruded twice through a polycarbonate filter (Whatman Nucleopore) with pore size 100 nm, and five times through a filter with a pore size of 50 nm. The average liposome diameter for all formulations was determined by dynamic light scattering.

5. General membrane labeling procedure

To fluorescently label the cell bleb proteoliposome membranes for the visualization of bilayer formation, blebs were incubated with 0.18 mM R18 for 15 minutes in a sonicating bath (VWR) on the lowest setting.

To fluorescently label membranes for fusion experiments, 5 µl of SA-liposome or virus solution was diluted with 250 µl of buffer A and mixed with 0.1 µl of 1.8 mM R18 for 1 hour in a sonicating bath. For fusion experiments, it is desired to label membranes with a quenched amount of R18 to mark membrane hemifusion events by fluorescence dequenching. Free R18, which did not insert into the membranes, was removed from the solution by centrifuging (Eppendorf, Centrifuge 5451C, Hauppauge, NY) through a G-25 spin column for 2 minutes at rate of 3x1000 min^{-1}. The supernatant containing the purified SA-liposomes or virus was diluted with 1.8 ml

of buffer A and gently vortexed to mix.

6. General liposome or virus interior labeling procedure

For pore formation experiments, 5 μl of SA-liposome or virus solution was mixed with 10 μl of 20 mM Sulforhodamine B (SRB) solution and incubated overnight. Excess SRB, which did not partition into the SA-liposome or virus interior, was removed from the solution by centrifuging through a using a G-25 spin column for 2 minutes at rate of 3x1000 min^{-1}. The supernatant was diluted in 800 μL of buffer A prior to use.

Cell bleb and supported bilayer characterization

1. Size distribution in cell bleb supernatant

The hydrodynamic diameter and its distribution for the cell bleb supernatant were measured using dynamic light scattering. A plot of the size distribution is shown in Fig. B1.

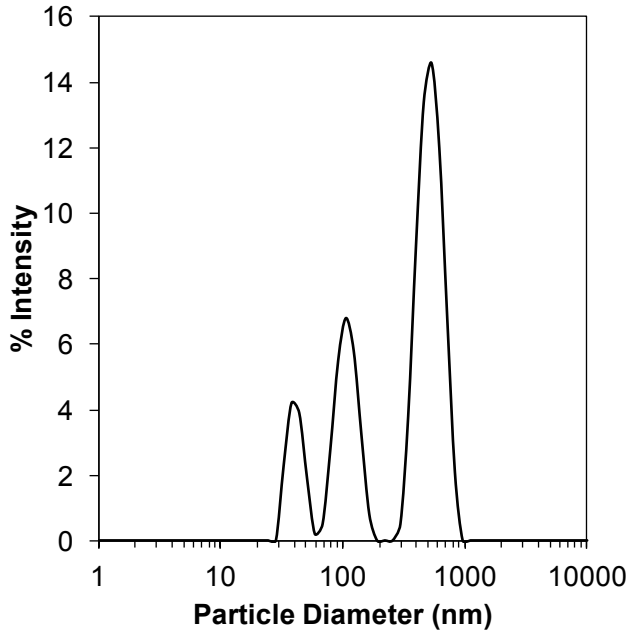

Fig. B1. Distribution of particle diameters in cell bleb samples determined by dynamic light scattering.

2. Atomic force microscopy (AFM)

AFM was used to image the supported bilayer samples and measure bilayer thicknesses. Samples for AFM were prepared as described and the surfaces were gently scratched so as to allow a step height measurement of the lipid bilayer. Samples were imaged with a PicoPlus 2500 AFM (Molecular Imaging) using DNP-S10 contact mode tips (Bruker). Images were taken under aqueous buffer in contact mode at 10 μm/s, 256 lines per image, and 10x10 μm scan size.

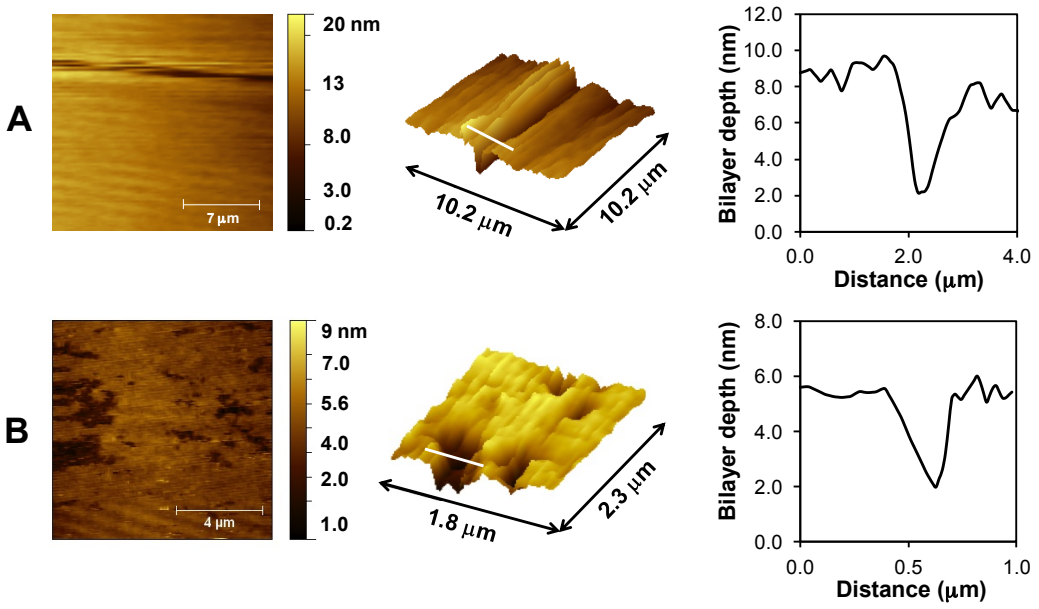

Fig. B2. AFM images confirm the presence of a lipid bilayer. A) 2D and 3D AFM images of BHK-liposome (bleb-free) SLB with accompanying depth profile across the scratch (white line) in the 3D image. B) AFM image of ruptured HA-bleb bilayer formed with BHK-liposomes with accompanying depth profile (white line) of a defect in the 3D image.

3. Ellipsometry

Ellipsometry was used to confirm thickness measurements made by AFM. An EP3 Imaging Ellipsometer (NanoFilm) with a liquid cell, filled with deionized water, was used for all ellipsometric experiments. Measurements of both bare silicon and bilayer films were taken to confirm oxide layer thickness. The area of the surface over which the measurements were made was 0.5 cm x 0.5 cm. Variable angle measurements of 57- 60 degrees were taken of areas of about 0.25 mm^2 at a wavelength of 531.7 nm. The data from the ellipsometric measurements was modeled using a Marquardt-

Levenberg simulation in Thin Film Companion software (Semiconsoft, Inc.). The thickness of the oxide layer on the bare silicon wafer used for these experiments was determined to be approximately 4.1 nm, and this value was incorporated into the calculation of total supported bilayer thickness. For the supported bilayers, we used frequency-dependent complex refractive index parameters, n = 1.38 and k = 0, based on previously published results (168, 169), to model the experimental data.

Table B1
Average thickness of supported bilayer films measured by ellipsometry

Sample	Thickness (nm)
(A) BHK-liposome SLB	3.2
(B) HA-bleb+BHK-liposome SLB	3.9
(C) Adsorbed HA-blebs	--

4. Antibody binding experiments

The following figure show the antibody binding to the VLSB and control cases, with appropriate background reference to asses specific binding, as described in the main text.

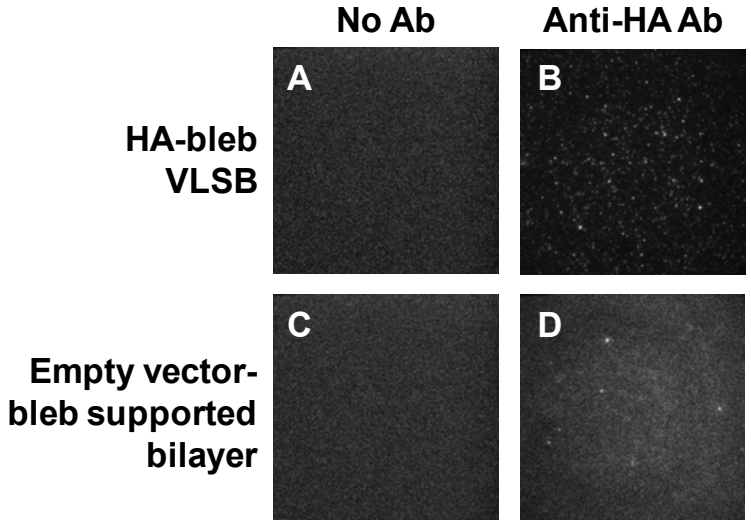

Fig. B3. Antibody binding to various supported bilayers derived from cell blebs. (A) HA-VLSB (no fluorescent label or antibody, just background signal); (B) HA-VLSB with fluorescently-labeled anti-HA bound; (C) Empty vector-bleb supported bilayer (control case with no fluorescent label or antibody present); (D) Empty vector-bleb supported bilayer with fluorescently-labeled anti-HA.

5. Diffusion measurements in supported bilayers using fluorescence recovery after photobleaching

Integrity of bilayers and diffusion of the lipids within it was examined by fluorescence recovery after photobleaching (FRAP). Bilayers were formed following the above procedures inside PDMS wells. R18 was used to label the bilayer and carry out the photobleaching experiments. Once formed, bilayers were gently scratched with a dissection tool to remove a thin section of the supported bilayer. This line aided in focusing on the plane of the bilayer on the microscope. Following this step, the bilayer was rinsed for 1 minute with buffer A to wash out any lipids removed by scratching. A ~20 μm diameter spot in the supported lipid bilayer was bleached with a 4.7 mW 488 nm krypton/argon laser for 200 ms. The recovery of the fluorescence intensity of the photobleached spot was recorded for 15 minutes at regular intervals. The fluorescence intensity of the bleached spot for each image was determined after background subtraction and normalization. The recovery data was fit using a Bessel function following the method of Soumpasis (166). The diffusion coefficient was then calculated using the following equation:

$$D = \frac{w^2}{4t_{1/2}} \tag{B1}$$

where *w* is the full width at half-maximum of the Gaussian profile of the focused laser beam.

6. Diffusion coefficients in supported bilayers determined by fluorescence dispersion during hemifusion

Table S2
Diffusion coefficients determined from the radial dispersion of R18 fluorophores during membrane hemifusion

R18 HA-bleb to SA-SLB	$0.14 \pm 0.08\ \mu m^2/s$
R18 SA vesicle to HA bilayer	$0.27 \pm 0.11 \mu m^2/s$
R18 Virus to SA-SLB	$0.22 \pm 0.03\ \mu m^2/s$

Appendix C

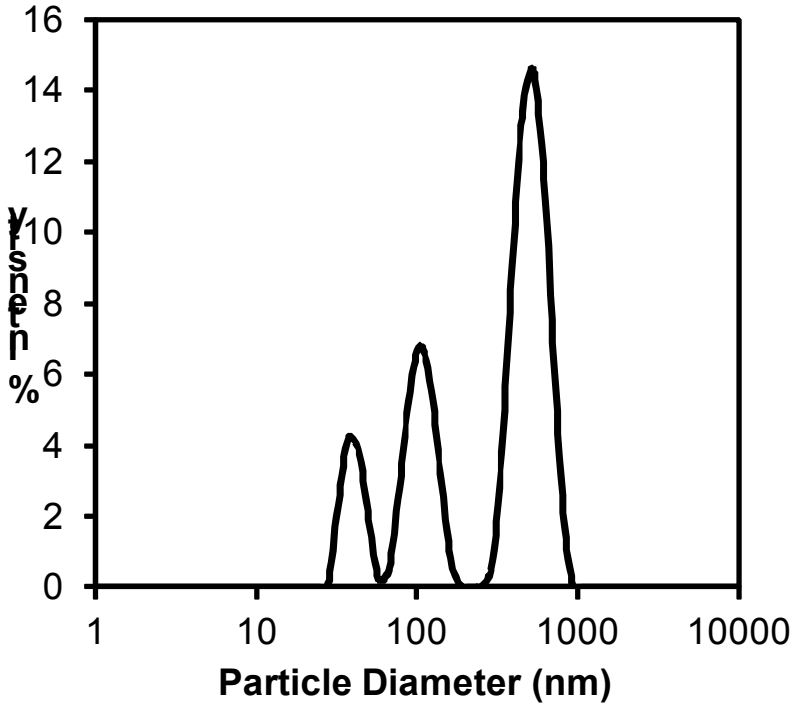

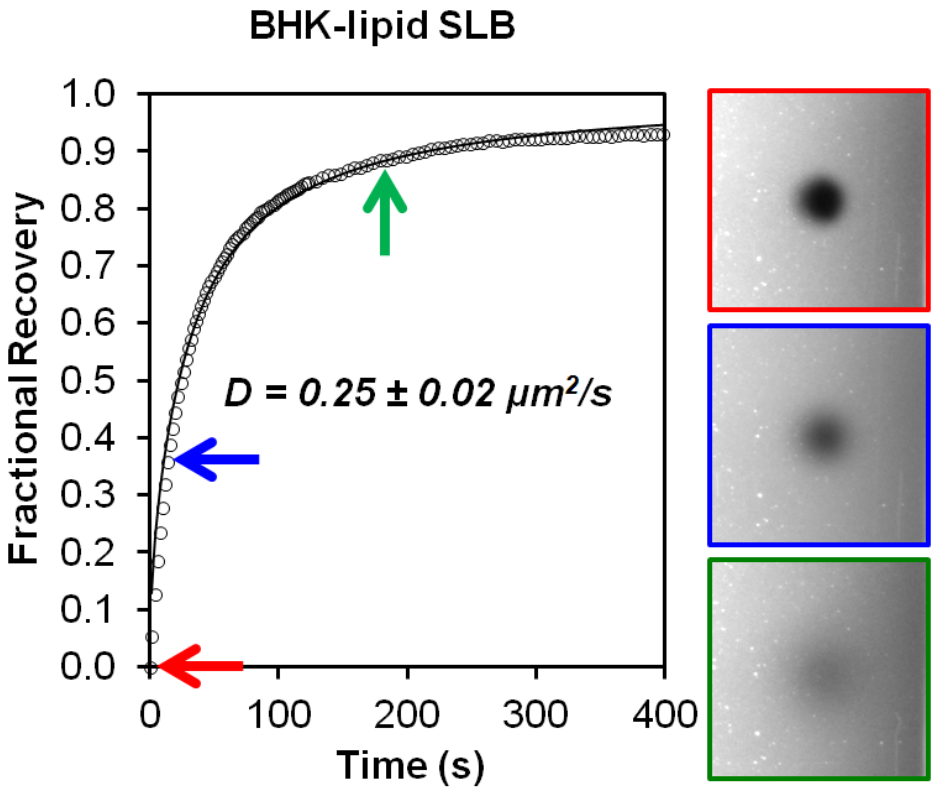

Figure C2 Lipid-only supported bilayer characterization and mobility. (a) R18 fluorescence recovery after photobleaching in a supported bilayer made from BHK-liposomes labeled with R18. The images correspond to the times for each color-coded arrow on the plot. The data are fit to curve (black line) to obtain the diffusion coefficient, as described in the *Methods* section. At t = 0, the bilayer was bleached with a 561 nm laser beam. The diameter of the bleached area is ~ 20 μm. The reported diffusion coefficient on the plots is averaged from several experiments.

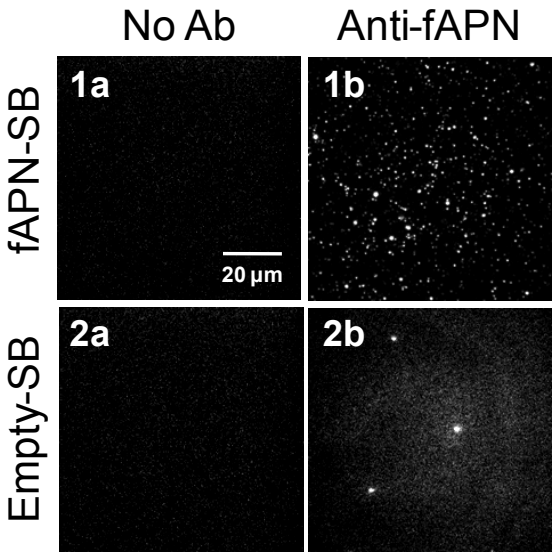

Figure C3 Antibody binding to various supported bilayers. Row 1: (1a) fAPN-SB (no fluorescent label); (1b) fAPN-SB with fluorescently-labeled anti-fAPN. Row 2: (2a) Empty vector-SB (control case with no fluorescent label); (2b) Empty vector-SB with fluorescently-labeled anti-fAPN.

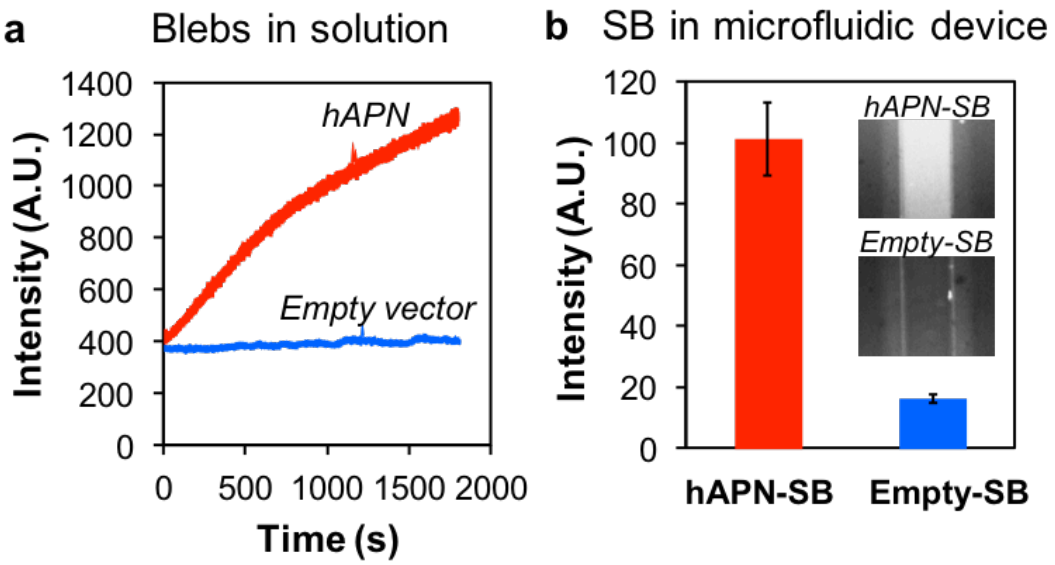

Figure C4 Enzymatic activity of APN in cell blebs and in supported bilayers. (a) Fluorescence intensity measured in a fluorimeter over time for hAPN blebs (red) and empty vector bleb control (blue). Intensity increases as substrate is cleaved by APN present in cell blebs. The control case is the empty vector bleb. (b) Fluorescence intensity measured inside microfluidic channel coated with hAPN-SB. The intensity is measured after 12 hours. The inset shows the microchannels for the hAPN and empty vector supported bilayers under the same experimental conditions.

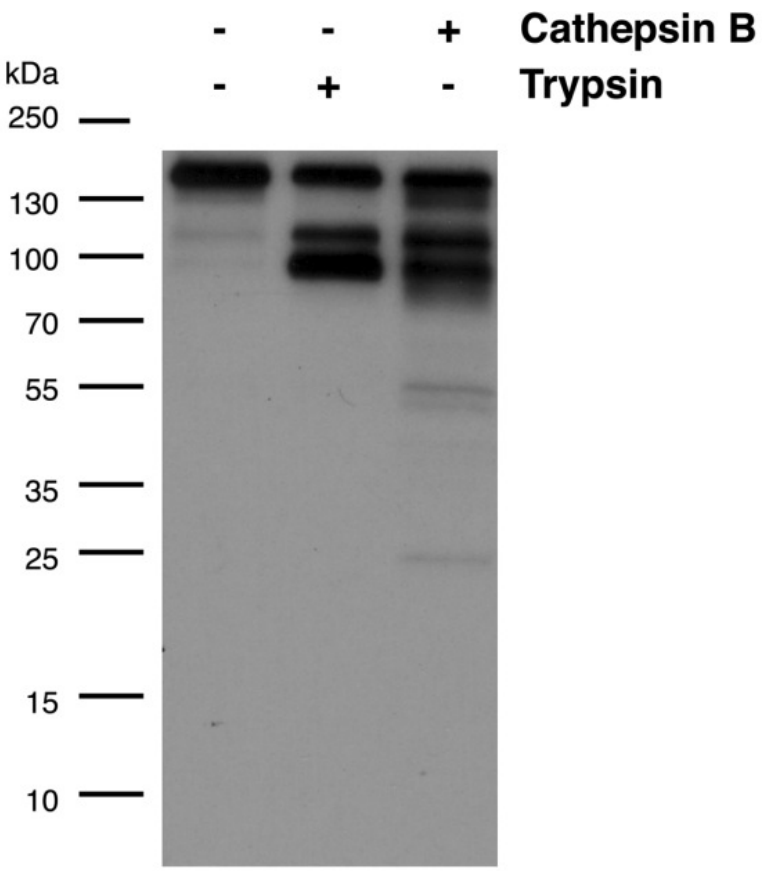

Figure C5 Cleavage of FCoV-1683 by cathepsin B and trypsin. Ultracentrifuged viral preparations of FCoV 1683 were either non-treated, trypsin-treated, or cathepsin B-treated. The samples were then subjected to deglycosylation by PNGase F treatment to avoid having differentially glysosylated species of FCoV-1683 S. Samples were then analyzed by Western blot with the anti-FCoV S mAb 22G6.4.